

Politecnico di Torino

ScuDo
Scuola di Dottorato ~ Doctoral School
WHAT YOU ARE, TAKES YOU FAR

Doctoral Dissertation
Doctoral Program in Metrology (37^{th}cycle)

Operation and optical frequency comparisons with an ytterbium optical lattice clock

By

Stefano Condio

******

Supervisor(s):
Dr. Marco Pizzocaro, INRiM

Doctoral Examination Committee:
Dr. Filippo Bregolin, Referee, Toptica Photonics AG
Dr. Jacopo Catani, Referee, CNR-INO

Politecnico di Torino
2025

Declaration

I hereby declare that, the contents and organization of this dissertation constitute my own original work and does not compromise in any way the rights of third parties, including those relating to the security of personal data.

Stefano Condio
2025

* This dissertation is presented in partial fulfillment of the requirements for **Ph.D. degree** in the Graduate School of Politecnico di Torino (ScuDo).

Acknowledgements

First, I would like to thank my supervisor Marco Pizzocaro for the constant support and precious advice during the three years of my Ph.D. A particular acknowledge goes to the other members of the ytterbium group at INRiM, Irene Goti and Tommaso Petrucciani, for all the time shared in the lab fixing problems, aligning lasers, tuning PID and (in the remaining time) operating the clock.
My gratitude goes to all the researcher and doctoral fellows of the INRiM frequency group, Hoping not to forget anyone, Matteo Barbiero, Juan Pablo Salvatierra, Michele Gozzelino, Matias Risaro, Francesca Famà, Simone Donadello, Chiara Spano, Stefano Giaccari, Cecilia Clivati, Marco Tarallo, Gianluca Bertaina, Salvatore Micalizio, Claudio Calosso, Giovanni Costanzo Elio Bertacco, Alberto Mura and, finally, the group leaders Filippo Levi and Davide Calonico. I did not interact with all in the same way, but I really enjoyed the interesting discussions, hanging out for a drink or a padel match and the crazy lunch conversations.
Finally I would like to acknowledge professor Florian Schreck for giving me the opportunity to join the Universiteit Van Amsterdam for a secondment and all the Strontium Quantum Gases group for the welcoming me and involving in several activities. Especially thanks to András Gácsbaranyi, Scott Wolzak, Sheng Zhou and Sumit Sarkar for the nice moments spent in the lab.

FundingsThe project 18SIB05 ROCIT and 22IEM01 TOCK have received funding from the European Partnership on Metrology, co-financed from the European Union's Horizon Europe Research and Innovation Programme and by the Participating States.



Abstract

Optical clocks represent the state of the art in frequency metrology. They have widely surpassed microwave frequency standards, achieving unprecedented levels of accuracy and stability. This advancement pushes the limits of fundamental research, enabling tests of variations in fundamental constants, detection of dark matter, and explorations in general relativity. For all these reasons, optical frequency standards are considered the strongest candidate to replace Cesium clocks for a new definition of the second in the International System of Units. The mandatory criteria for a new definition have been established in a roadmap that guides international efforts toward their fulfillment. These requirements include absolute frequency measurements of optical transitions, frequency ratios between optical clocks, and regular contributions to timescale generation. This thesis aims to explore the potential and reliability of optical clocks for a new definition of the second, addressing the main challenges along this path.

My Ph.D. research mainly focused on the operation and improvement of the IT-Yb1 optical lattice clock, developed at INRiM and based on neutral ^{171}Yb atoms. Its fractional systematic uncertainty has been characterized at the level of 1.9×10^{-17} with an instability of 2×10^{-15} at 1 s. I will present several improvements I implemented on this atomic clock, including enhancing its automation capabilities to facilitate unattended measurements and optimizing the atomic state preparation phase. Specifically, these improvements involved optimizing the spin polarization process and implementing a sideband cooling scheme on the clock transition to reduce the temperature of the atomic ensemble.
I will describe the main metrological results obtained during these years. These include two absolute frequency measurements of the ytterbium clock transition, conducted both locally and remotely for more than 900 hours. My work also involved participation in two international frequency comparison campaigns, connecting up to 11 optical clocks across Europe via fiber link and GNSS satellite, where I contributed

operating the clock continuously to collect data for more than one month. In addition, I will present IT-Yb1's participation in the calibration of Coordinated Universal Time (UTC) for 16 consecutive months. I will also discuss the generation of a local timescale, steered solely by data from the INRiM ytterbium clock for over a year.
I will also describe my activities during a secondment at the University of Amsterdam, where I contributed to the development of an active optical clock based on superradiance. This technology represents a promising future advancement in optical frequency metrology. My specific focus was on the design and characterization of a transfer cavity used to transfer spectral purity from a stable reference to the lattice laser employed in the clock.
This work directly contributes to the ongoing advancement of optical atomic clock technology and its impact on a new definition of the second.

Contents

1 Introduction **1**

1.1 Optical clocks 1

1.2 Redefinition of the SI second 5

1.3 Timescales 7

1.4 Frequency measurements 9

1.5 Thesis Outline 11

2 IT-Yb1 **13**

2.1 Ytterbium atom 13

2.2 Experimental setup 15

2.2.1 Physical package 18

2.2.2 Manipulation lasers 19

2.2.3 Clock laser 22

2.2.4 Clock cycle 24

2.3 Uncertainty budget 26

2.3.1 Density Shift 27

2.3.2 Static Stark Shift 28

2.3.3 Lattice light shift 30

2.3.4 Black Body Radiation Shift 34

2.3.5 Zeeman shift 35

2.3.6 Probe Light shift 36
2.3.7 Gravitational redshift 37
2.3.8 Background gas shift 37
2.3.9 Other effects 38
2.4 State preparation 39
2.4.1 Spin Polarization 39
2.4.2 Sideband Cooling 44

3 Metrological Results 52
3.1 Absolute Frequency Measurement IT-Yb1:IT-CsF2 53
3.1.1 Optically generated microwave 56
3.1.2 Total result 57
3.2 International campaign 58
3.2.1 Remote clock comparison: INRiM SYRTE 2021 59
3.2.2 ROCIT 2022 Campaign 64
3.2.3 2023 International measurement campaign via fiber link . . 68
3.3 UTC contribution 70
3.4 Optical timescale 76
3.4.1 Conclusions 81

4 Secondment at UvA - transfer cavity stabilization for an active clock 83
4.1 Active optical resonators 83
4.2 Outlook - "mHz machine" 85
4.2.1 Current status 88
4.3 Magic lattice generation 88
4.3.1 Injection locking of a 808nm laser diode 89
4.3.2 Optical Injection locking (OIL) 90

4.4 Frequency stabilization 94
4.4.1 Design consideration 95
4.4.2 Cavity setup 98
4.4.3 Optical and electronic setup 101
4.5 PDH stabilization 103
4.5.1 Lattice lock 103
4.5.2 Transfer Lock 104
4.6 Conclusion 106

5 Conclusions **107**
5.1 Conclusions 107
5.2 Next steps 109
5.3 List of Publications 110

References **111**

Chapter 1

Introduction

1.1 Optical clocks

The working principle of every clock is based on counting the oscillation of a periodic event with constant frequency. As the oscillator can be affected by different sources of noise, its frequency has to be corrected keeping it locked with respect to a frequency reference.

Even optical clocks follow this principle and their excellent performances lie in the choice of the high frequency oscillators and reliable references. An ultrastable laser is employed as *Local Oscillator* (LO), which is a counted periodic event with known frequency. Its emission stimulates a particular optical atomic transition that constitutes a high reliability frequency reference. By comparing the oscillator with respect to the reference, it is possible to correct its frequency to keep it locked to the target value. Both high precision and accuracy derive from the choice of atomic species and transitions: a good frequency reference must be characterized by a high quality factor $Q = \nu_0/\gamma$, thus elevated natural frequency ν_0 and narrow natural linewidth γ, and also poorly influenced by external perturbations.
Accuracy is limited by environmental factors that affect the atoms and shift the resonant frequency from the ideal unperturbed conditions. The evaluation of these systematic effects is the fundamental uncertainty limit and the best optical clocks achieved fractional accuracy at level of low 10^{-18} [1–3].
Two categories of optical clocks are now diffused in the world: single ion clock and lattice clocks with neutral atoms. The former based on probing a single ion confined

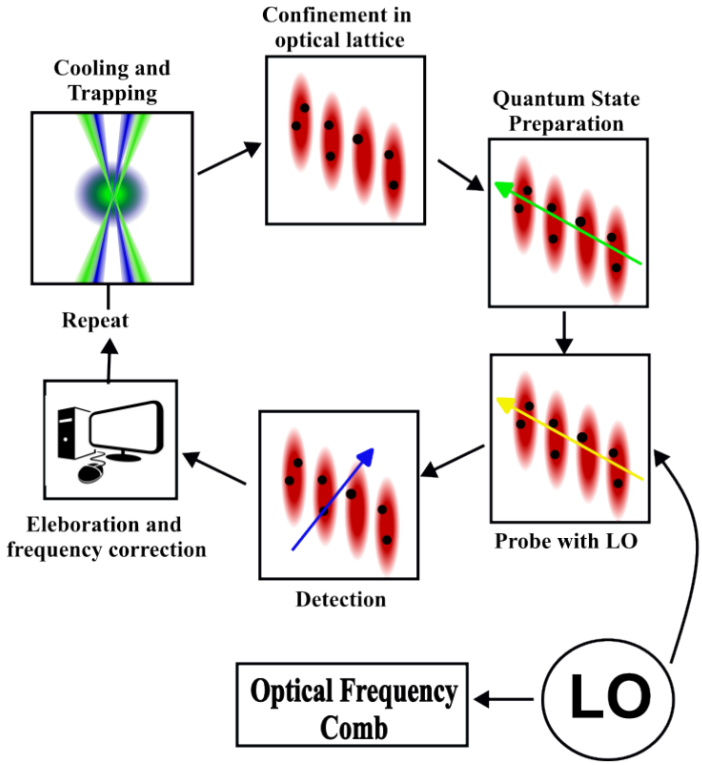


Fig. 1.1 Typical working scheme of an optical lattice clock based on neutral atoms. Thermal atoms are cooled and confined in an optical lattice, where they are prepared in the desired quantum state. There the clock laser (LO) probes the frequency reference with a spectroscopy of the clock transition. Detecting the fraction of interacting atoms, a servo loops correct the LO frequency, counted by a frequency comb.

in a Paul trap. This type will not be discussed during this thesis. Optical lattice clocks are instead based on trapping an ensemble of few thousands of neutral atoms in an optical lattice, and these will be the core of this thesis.

Figure 1.1 schematically represents the typical clock cycle in neutral-atom-based clocks: atoms from a thermal beam are cooled and trapped in Magneto Optical Trap (MOT) and then confined in an optical lattice, obtained with a back-reflected laser beam far from resonance [4]. Atoms are thus prepared in the desired quantum state and then the Local Oscillator performs a spectroscopy on the clock transition, probing the frequency reference. After that, the detection phase follows to discriminate the fraction of atoms that interacted with during the interrogation and then a frequency correction is applied to the LO, keeping it resonant with the frequency reference.

The precision, expression of the statistical uncertainty, depends on the clock stability. It describes the variation of the measured frequency over time, so it can also be defined as instability. This statistical quantity is typically described using the Allan Variance $\sigma_y^2(\tau)$, the two-samples variance of the average fractional frequency difference evaluated over a duration τ [5–7]. It provides information about the reduction of statistical uncertainty in time and it makes possible to distinguish different sources of noise affecting the local oscillator frequency. As in optical clock the frequency fluctuations are dominated by white noise, instability decreases with the square root of measurement time [8]:

$$\sigma_y(\tau) = \frac{1}{\kappa_s \cdot SNR \cdot Q}\sqrt{\frac{T}{\tau}} \tag{1.1}$$

where κ_s is a parameter depending on the spectroscopy method, $SNR = S_0/\delta S$ is the signal-to-noise ratio of the measurement and T is the total duration of the measurement. Crucial parameters are thus the quality factor (up to 10^{15} for optical transition against about 10^{11} for microwave standards) and *SNR*, scaling with the number of atoms. Two effects constitute a limit for the stability, the Quantum Projection Noise (QPN) [9] and the Dick effect [10]. The first comes from the intrinsic randomness of quantum mechanics, inducing statistical fluctuation in the measurement process when atoms are interrogated with the same probability to be found in the ground and in the excited state. It is a fundamental limit that cannot be canceled but only reduced by increasing the SNR. In recent years spin-squeezing-based protocols have been investigated to overcome this limit [11, 12]. The Dick effect instead constitutes the actual stability limitation in real systems. It is generated by the LO noise during the dead times, when the frequency reference is not probed (e.g. during the preparation of the atomic sample or the preparation of the desired quantum state). Between two consecutive interrogations, when the LO is not measured with the atoms, the noise induces a frequency drift and thus an aliasing effect affecting the clock stability. Two intuitive solutions help bringing down this effect: reducing the LO noise (like locking the clock laser to an ultrastable cavity) and minimizing the deadtimes between interrogations accelerating the preparation of the sample. Novel approaches are under investigation to remove or strongly suppress the Dick effect, such as quantum non-demolition measurements [13–15] and zero-deadtime continuous measurement [16–18].

The Optical Frequency Comb (OFC) is the instrument employed to count the LO frequency. It is based on a mode-locked femtosecond pulsed laser, whose broadband spectrum can be decomposed in the frequency domain in a series of peaks equally spaced like the teeth of a comb, hence the name. As the mode locking condition imposes that all peaks are separated by the same frequency f_{rep}, also called repetition rate, the frequency of the nTH tooth can be calculated with:

$$f_n = f_{CEO} + n \cdot f_{rep} \tag{1.2}$$

where $f_{CEO} = f_{rep}\frac{\Delta\phi}{2\pi}$ is the so-called carrier-envelope offset and $\Delta\phi$ is phase offset between two consecutive laser pulses. This peculiar spectrum can be employed as a ruler in the frequency domain, allowing one to track an optical frequency by measuring the beatnote between the LO and the nearest comb tooth.
In addition, OFC can be employed as transfer oscillator to compare two oscillators measured with the same comb: this technique is commonly employed to compare two different optical clocks or to down-convert an optical frequency to the microwave regime, making it possible to perform measurement against the primary Cs standards.

Applications

Due to their extremely high accuracy and stability, there is a rising interest in optical atomic clocks for experiments of fundamental physics and searching for new physics. Several experiments have been conducted to measure variations of fundamental constants in time, such as the constant of fine structure α [19, 20]: transition frequency between energy levels depends on α, which is responsible for the coupling of charges with electromagnetic fields, thus a time drift in the measured frequency ratio between two different species could evidence a time variation of this constant. Pioneer experiments intend to employ a global network of optical clocks to detect topological dark matter interaction as a shift in the measured clock frequency [21, 22]. In addition, general relativity tests have been widely studied with optical clocks [23, 24]. Regarding applied physics, optical clocks could provide advancements and improvements in the field of the timekeeping and the navigation systems, further breaking the uncertainty limits of the caesium clocks. By measuring the gravitational field with high accuracy, optical clocks can be employed for global geodesy which also find applications in other scientific fields.

1.2 Redefinition of the SI second

Since the XIII CGPM in 1967, the second in the International System of Units has been defined starting from the unperturbed frequency of a hyperfine transition of the ^{133}Cs atom. The current definition, fixed in 2019, is the following [25]:

The second, symbol s, is the SI unit of time. It is defined by taking the fixed numerical value of the caesium frequency $\Delta\nu_{Cs}$*, the unperturbed ground-state hyperfine transition frequency of the Caesium 133 atom, to be* 9 192 631 770 *when expressed in the unit* Hz*, which is equal to* s^{-1}

Caesium fountains are the primary frequency standards and the best realization of this definition, with a relative frequency uncertainty at the level of 10^{-16}. Other atomic transitions have been recommended by CCTF as secondary frequency standards, so without inherent accuracy and requiring to be referred to a primary standard. These include a rubidium microwave transition and 11 optical transitions in both ions and neutral atoms [26, 27] and their values are periodically updated. The SI second can be obtained indirectly from secondary representations and some of them are intrinsically accurate at the level of 10^{-18}, widely exceeding the primary ones. This is the main reason for the change in the definition of the second that surpasses the Cs atoms. Other motivations come from the stakeholders that require lower uncertainties for highly demanding experiments, such as in the field of relativistic geodesy.

Three options are now under exam as new definition [28]: the first is based on replacing the current Cs frequency standard with an optical transition by fixing its frequency to the numerical value $\nu_i = N$ Hz, where N is the defining value. The main advantage resides in its simplicity and in the gain of lower uncertainty in the second realization, characteristic of optical clocks. Option 2 consists in a weighted geometric mean of the frequencies of several transitions [29]. In this case, SI second would be defined by fixing the average frequency of the ensemble $\Pi_i \nu_i = N$Hz, defined by the numerical value N, and the weights w_i, whose sum is 1. An alternative version recently proposed, consisting in periodically updating the weights depending on the new measurements of the OFS that contribute to the definition [30]. Option 2 is more complicated for general users, but presents the advantage of including various standards instead of choosing only a single one, that could become obsolete or showing some unpredicted problem. Option 3 is instead closer to the definition of

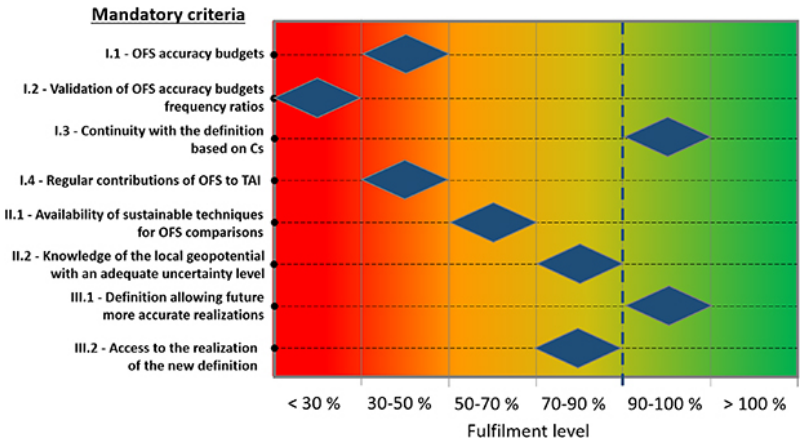


Fig. 1.2 Compliance status of the mandatory criteria for the redefinition of the second in 2022. Source *Dimarcq et al.* [28]

the other base units that compose the SI, fixing the numerical value of a fundamental constant of nature. Among the selected possibilities, there are the electron mass m_e, the Compton frequency ν_e or the Rydberg constant R_∞. The value of these constants can not be fixed by choice but has to be measured, but currently the associated uncertainty is several orders larger than the present realization and definitely not competitive with optical clocks.
Option 1 and 2 are thus the strongest candidates, improving by two orders of magnitude the current definition. Regardless the new definition choice, all the other SI base units except the mole will be influenced by this variation due to their dependence on the unit of time [25].

Before a proposal for a new definition based on optical clocks will be submitted to the General Conference on Weights and Measures (CGPM), CCTF sets out a list of mandatory requirements that must be met [28]. The diagram in figure 1.2 summarizes the necessary requirements that have been stated with their level of fulfillment. Concerning the optical clocks these criteria include: continuity with the current definition (absolute frequency measurements with uncertainty $\Delta\nu/\nu < 3 \times 10^{-16}$), at least 3 OFS characterized with uncertainty below 2×10^{-18}, validation of the accuracy budget through clock comparisons in agreement at $< 5 \times 10^{-18}$, high reliability of optical frequency standards for continuous operations and regular contribution to the calibration of both international (TAI and UTC) and local timescales. Other criteria concern the links to compare and distribute OFS and the accessibility of the new

definition to Countries and laboratories without an optical clock. Currently only two mandatory criteria achieved complete compliance (continuity with the past and feasibility of new improvements), while other requirements have been just partially fulfilled. A new definition is not expected before CGPM 2030.

1.3 Timescales

Generation and calibration of the international timescales is one of the main applications involving atomic clocks. Classical timescales based on the observation of celestial phenomena are not sufficient for the necessities of modern times, such as Global Navigation Systems and financial transactions.
Several requirements must be met to generate a reliable and scientifically accurate timescale. Among the most important, it must be universal (valid and accepted by all the Countries and organizations), perpetual (extendable to the past and the future in continuity with previous scales), accessible to the users all over the world, reliable despite technical faults and finally, uniform and accurate with respect to the unit of measurement[31].
Atomic timescales became possible after 1967, when the XIII General Conference on Weights and Measurements (CGPM) changed the definition of the second based on the Cs atom. It provided the advantage of having more primary samples, being accessible diffused worldwide and, in particular, being more stable in frequency.

The Universal Coordinated Time is the only internationally recommended time scale and the basis of civil time in most countries. It is generated and diffused by the BIPM (Bureau International des Poids et Measures).

Its generation requires some steps, schematized in figure 1.3.
First the Echelle Atomique Libre (EAL) is generated by the weighted average of more than 400 atomic clocks in about 80 laboratories in the world. They are mainly free-running commercial clocks and provide a stable timescale but without a reference. Task of BIPM is to correct this timescale to be accurate and consistent with the definition of the SI second. This process is defined as *frequency steering* and is carried out with the contribution of several primary and secondary frequency standards from all over the world which provide their data. BIPM monthly steers EAL to generate the International Atomic Time (TAI), a coordinated time scale referenced to the SI second on the rotating geoid. It is a virtual timescale (i.e. post-processing

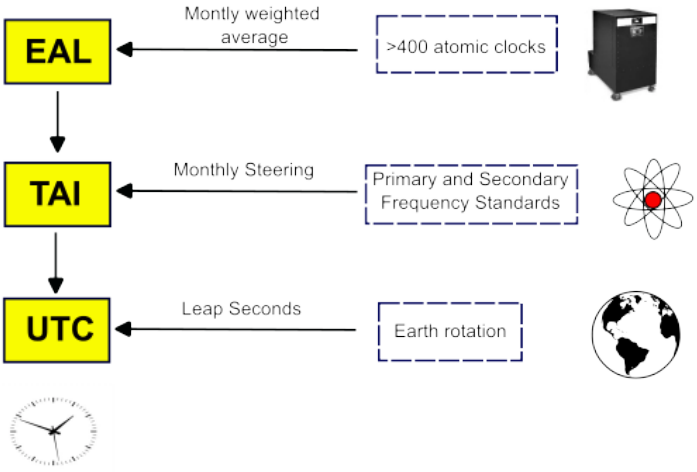


Fig. 1.3 Diagram of the generation of the Universal Coordinated Time. Echelle Atomique Libre, generated by several atomic clocks, is periodically frequency corrected respect to the definition of the second to generate the International Atomic Time. UTC is obtained adding leap seconds to keep TAI in agreement with the terrestrial time.

generated) and the results are published in *Circular T* [32], a monthly bulletin reporting the clocks contributing to TAI generation and the difference between TAI and local scales in 5-day intervals. The main participation in the TAI steering is still in charge of the primary frequency standards, the Cs fountains, but in recent years also secondary frequency standards and in particular optical clocks are increasing their participation.

The most widely used international standard in timekeeping is UTC, the Universal Coordinated Time. It is based on TAI but it is not continuous and differs for an integer quantity of leap seconds that make UTC more suitable for the daily civil use. This offset has been added to TAI to keep UTC locked to the terrestrial time UT1 (calculated with respect to the angular position of the Earth along its revolution motion, which is slowing in time) making UTC suitable to civil applications. Following the report of the International Earth Rotation and Reference Systems Service (IERS)[33], if the difference $|UTC - UT1|$ is greater than an integer number of seconds, UTC must be aligned by adding the same number of leap seconds. This addition can be done every 6 months and since 1972 UTC accumulated 37 s of offset from TAI. From 2035 new leap seconds will not be taken into account due to technological criticality, fixing a maximum displacement between UTC and terrestrial time before future alignment [34].

The National Metrological Institutes (NMIs) in each Country generate the local realization of UTC, UTC(k), regularly realigned on the global time scale reporting the difference on the Circular T.

1.4 Frequency measurements

Measuring an optical frequency with an optical clock means counting the frequency of the Local Oscillator, locked to the atomic unperturbed transition which serves as frequency reference. In practice, it means comparing the beatnote between LO and the comb with a reference signal coming from a hydrogen maser. In case the H-maser is measured with respect to a primary sample, the OFS is compared with the definition of the second and this is defined as an absolute frequency measurement. Both the comb and the H-maser cover the role of transfer oscillator to connect the optical and the microwave frequency, referred to the definition of the SI second.
A local absolute frequency measurement can be directly performed if a Caesium fountain is present and it is operating contemporaneously and in the same place with an optical clock, measuring both the oscillator with the same comb. In case a primary sample is not available, the definition of the second can be accessed with a link to TAI: the International Atomic Time is in fact strictly connected to the SI second thanks to the steering contribution of about 10 Cs fountains worldwide. The distribution via Global Navigation Satellite Systems (GNSS) and Two Way Satellite Time and Frequency Transfer (TWSTFT) techniques makes TAI globally available. This allows for the calibration of the H-maser frequency and remote measurements with high-frequency accuracy.
In any case, absolute frequency measurements of OFS are limited at the level of the Caesium clocks, even if secondary frequency standards in principle present an accuracy of two orders of magnitude better. This problem will be fixed after an optically based new definition of the second or by directly comparing optical clocks. The result, expressed in terms of ratio between two different optical frequencies, is more effective in detecting the true level of accuracy of an optical clock. During the measurement of two optical frequencies with the same comb, in principle stability and uncertainty are only limited by the performances of the two clocks [35].
Local comparisons can be performed only if the two clocks are in the same place, allowing measurement with the same frequency comb. In case this is not possible,

remote measurements can be obtained by connecting clocks located in different places using high accuracy links. Currently, the most performing techniques is based on optical fiber links: it is based on transmitting an ultrastable 1542 nm laser into an optical fiber and counting its frequency with an OFC at the two terminals. The two clocks can be put in contact by counting their frequency with respect to the same laser, which constitutes a transfer oscillator. This technique introduces a contribution to the measurement uncertainty at the level of 10^{-19}, one order of magnitude lower than the best optical clocks, and few hours of measurements are sufficient to achieve this level of uncertainty. Comparisons between clocks placed thousands of kilometers away are possible without affecting the uncertainty budget, but they are limited to intracontinental connections. Intercontinental connections are feasible thanks to GNSS techniques [36–38], widely explored for microwave clocks but suitable also for opticals, and, more recently, Very Long Baseline Interferometry (VLBI) radiotelescopes [39–41]. Both methods are characterized by lower infrastructure requirements, but they strongly underperform compared to the fiber link in terms of stability and uncertainty, (limited at 10^{-16}) and require several days of continuous operation.

Both absolute frequency measurements with relative uncertainty $<3 \times 10^{-16}$ and frequency ratios of optical transitions in agreement within 5×10^{-18} are necessary in the roadmap for the redefinition of the second [28], but while the first are now common, the latter are still far away, except in a few cases. As absolute frequency measurements are the only way to determine an OFS with respect to the current definition, CCTF periodically updates the recommended value of the secondary representations of the second from a weighted average of all the reported values from laboratories around the world. By way of illustration, figure 1.4 reports the history of the absolute frequency measurements of the clock transition of the neutral ^{171}Yb (one of the most investigated atoms in optical clocks) compared with the evolution of the recommended value over time. Dots and diamonds distinguish the absolute measurements performed with Cs fountains from the one obtained with a link to TAI. The reference value, so the one recommended by CCTF [27, 26], is indicated by the red lines while the associated uncertainty is represented by the shaded region. This graph evidences the evolution of this value after successive CCTF thanks to the contribution of new measurements with higher accuracy as well as the uncertainty now limited only by the primary standards. The institutes that contributed to these

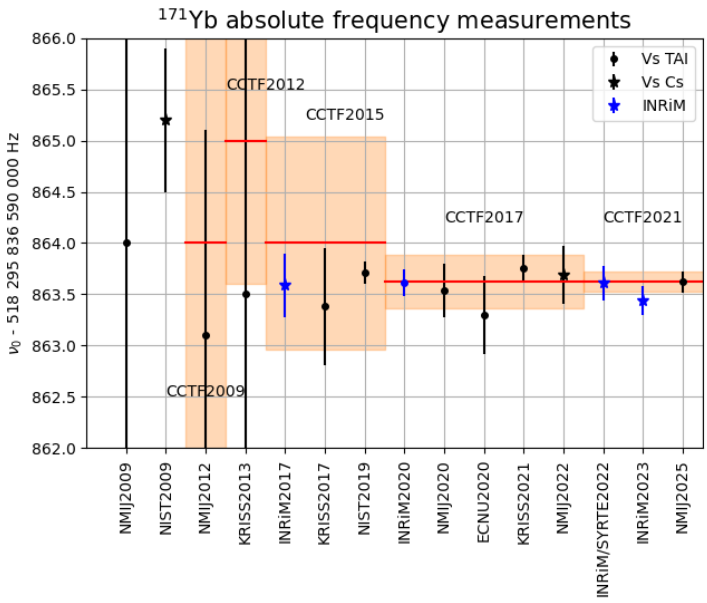


Fig. 1.4 Absolute frequency measurements of the ^{171}Yb clock transition performed in the last years compared to the values recommended by the CCTF. Circles (Stars) represent the measurements performed comparing with TAI (Caesium fountains) while blue markers highlight the one involving INRiM. Red lined and shaded regions respectively represent the CCTF recommended value after progressive updates (marked with the year) and the associated uncertainty.

measurements are NIST [42, 43] in USA, NMIJ in Japan [44–47], KRISS in South Korea [48–50], and ECNU in China [51]. In the last years INRiM contributed with 4 absolute frequency measurement (blue dots on the graph): first in 2016 measuring the optical clock IT-Yb1 against the italian primary frequency standard IT-Cs2 [52], and then in 2019 against TAI [53]. During my Ph.D. other two measurements took place, one local comparing the clock against IT-CsF2 for more than 900 hours [54] and another remote comparing IT-Yb1 with the Syrte Cs fountain, placed in Paris, connected with a more than 1000 km optical fiber link[55].

1.5 Thesis Outline

This manuscript describes some of the activities to which I contributed during my Ph.D. and is organized in the following order: Chapter 2 contains a description

of IT-Yb1, the ytterbium optical lattice clock developed at INRiM and on which I operated during these three years. In particular, I will focus on the description of experimental system, the clock operations, the improvements I implemented on the clock cycle and an overview of the systematic effects limiting the clock accuracy. Chapter 3 is dedicated to the main metrological results obtained while operating IT-Yb1. Among them, one can find two absolute frequency measurements, the participation to two campaigns of optical frequency comparisons, the contribution to the UTC calibration and the generation of an optically based local timescale. Chapter 4 contains the activities that I dedicated during my period as a visiting student at the University of Amsterdam. First it presents an outline of the working principle of the superradiance to generate active optical clocks and a short description of the experimental system under development. Then I will describe the main activities I performed, including the design and the characterization of the lattice laser system and a transfer cavity to frequency stabilize that laser.

Chapter 2

IT-Yb1

The main topic of my thesis is the work with the ytterbium optical lattice clock IT-Yb1, developed at INRiM and showed in figure 2.1. In this passive clock, laser-cooled atoms are trapped in an optical lattice to perform a Rabi spectroscopy of the ${}^1S_0 \rightarrow {}^3P_0$ clock transition with an ultrastable laser.
During this chapter I will describe the experimental setup of IT-Yb1, the operation principles and its uncertainty characterization. In the first section I am going to introduce the relevant characteristic of the ytterbium atoms that motivates its application in high-accuracy optical clocks. Then in section 2.2 I will describe the experimental apparatus forming the INRiM IT-Yb1 clock and its working. After that, in 2.3, I will present the main systematic effects affecting the clock uncertainty budget and their characterization at the level of 1.9×10^{-17}. Last section 2.4 contains some of the improvements I implemented during my Ph.D operating on the state preparation phase, in particular concerning the spin polarization and sideband cooling of atoms.

2.1 Ytterbium atom

The ytterbium atom is a lanthanide metal with an earth-alkaline-like atomic structure. In particular, the ^{171}Yb (I=1/2) fermionic isotope has interesting metrological properties that make it a suitable candidate as optical reference in atomic clocks, both neutral and ion. The ultranarrow ${}^1\mathrm{S}_0 \rightarrow {}^3\mathrm{P}_0$ (ΔS$\neq$0, J=0$\leftrightarrow$0, Δm_f=0) transition, excited with a 578 nm yellow laser, can be used as an atomic frequency reference due to a low sensitivity to external perturbations (reducing the effects of systematic

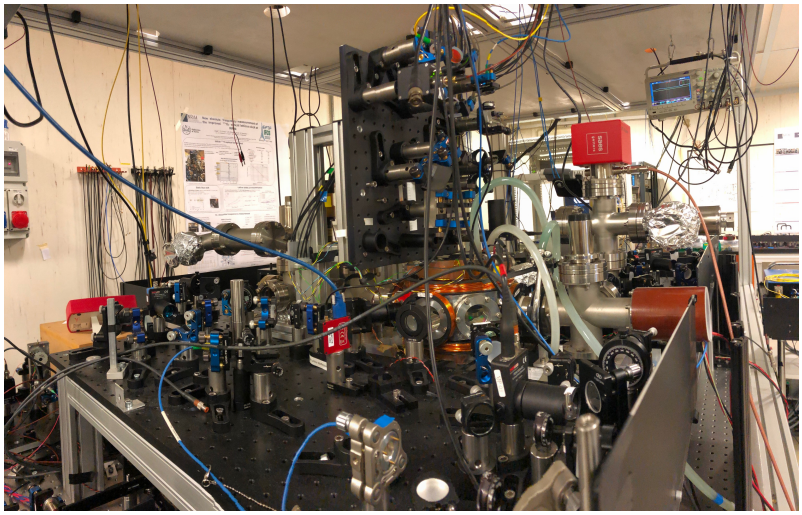


Fig. 2.1 IT-Yb1 physical package

frequency shifts) and a high transition quality factor Q. The quantum mechanic selection rules make this transition doubly forbidden for spin and angular momentum, inducing an extremely narrow natural linewidth $\gamma = 7$ mHz [56]. This, associated with a transition frequency $\nu_0 \simeq 518.295$ THz in the optical domain, leads to a quality factor Q of the order of 10^{17}. Due to the $F = 1/2$ hyperfine quantum number of the two clock states, under the action of a constant magnetic field two clock π transitions are possible with $m_F = \pm 1/2$. Furthermore, the zero electronic total angular momentum J reduces the sensitivity of the clock states to external perturbations and the hyperfine quantum number F=1/2 cancels the tensor light shift[57, 58]. Another advantage provided by the earth-alkaline-like structure is the presence of at least one *magic wavelength* [59] at which the polarizability of the two clock states is equal. It is a necessary requirement because the spectroscopy of the clock transition is performed by trapping atoms in an optical lattice, an electromagnetic standing wave perturbing the frequency resonance for AC Stark shift (also called lattice light shift). This contribution can be minimized by tuning the laser used to generate this optical trapping potential at the magic wavelength: among all the possible wavelength [60, 61], the 759 nm magic lattice is the most employed because of high-power laser availability and a low sensitivity of the polarizability from the laser frequency detuning [52]. Also other ytterbium transitions have recently been proposed as an alternative high-accuracy frequency reference [62, 63]. Among them, the inner-shell orbital transition ${}^1S_0 \rightarrow 4f^{13}5d6s^2(J = 2)$ at 431 nm, involving electrons from the internal $4f$ level, has been experimentally observed [64]. It is still far to be com-

monly employed in atomic clocks, but it presents highly promising properties in terms of sensitivity to external perturbations.
The 2 valence s-shell electrons generate a simple atomic structure, shown in picture 2.2, including singlet and triplet manifolds connected by strongly allowed or spin-forbidden transitions. Thanks also to the laser wavelength availability, this structure makes ytterbium feasible to trap and manipulate in experiments of atomic physics. The strong electric dipole $^1S_0 \rightarrow ^1P_1$ transition is characterized by a 28.6 MHz natural linewidth and a high photon scattering rate, allowing fast and efficient slowing and cooling of the atoms [8]. Furthermore, unlike strontium, another atom commonly employed in atomic physics and for high performance atomic clocks, it is a closed transition with negligible decay toward metastable the ^3P levels. For this reason, additional repumping lasers are not required in the trapping phase. This transition can be excited with 399 nm laser beams to trap Yb atoms in a so-called *blue* MOT limited in temperature at the mK level [65]. A further cooling stage is necessary to bring the temperature to the level of few microKelvin and it is obtained by the excitation of the narrower $^1S_0 \rightarrow ^3P_1$ intercombination *green* transition at 556 nm. This spin-forbidden atomic transition has a natural linewidth γ=182 kHz, corresponding to a Doppler temperature $T_D = \frac{h\gamma}{2k_b} \simeq 4.4\,\mu K$. This level of temperature is necessary to allow efficient transfer from the MOT to the optical lattice and to minimize effect dependent on the atomic motion, such as Doppler shift, density shift and lattice light shift (see 2.3).

The last atomic state of the ytterbium involved in the clock cycle is the $^3D_1$, used to repump atoms in the ground state after clock interrogation. Atoms in the metastable $^3P_0$ clock excited state are excited toward the short-living $^3D_1$ with a near-infrared 1389 nm laser and from there they decay toward the $^3P_1$ and then to the ground state [66].

2.2 Experimental setup

In this section, I will briefly describe the experimental setup of the optical lattice clock IT-Yb1. In-depth descriptions can be found in the literature [52, 54] or in other previous theses [66–70]. As represented in Figure 2.3, the experimental scheme of IT-Yb1 can be decomposed into blocks with different functions: the physical package, constituted by the vacuum chamber where the atoms are vaporized, cooled and then

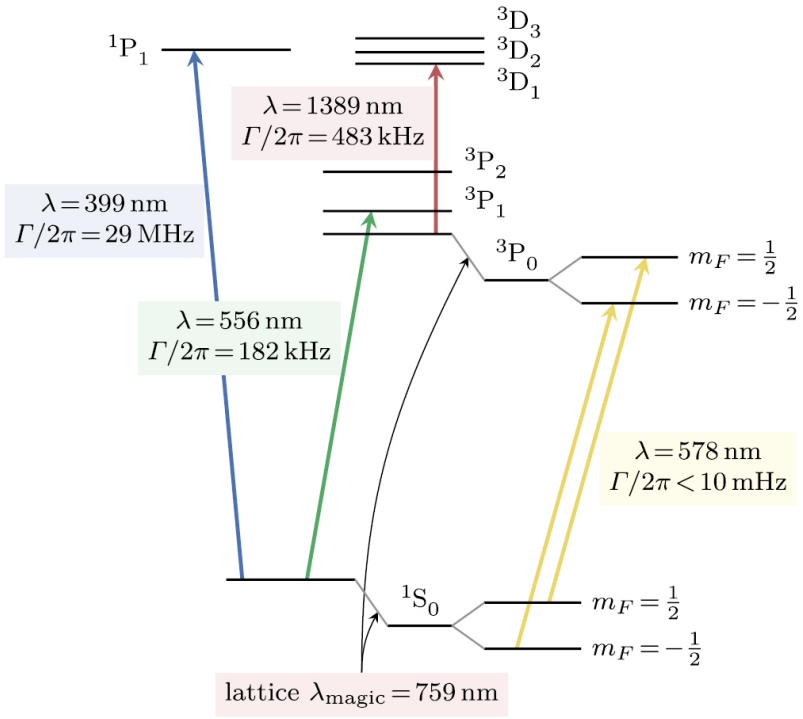


Fig. 2.2 Relevant energy levels with relative transitions involved in the ^{171}Yb atomic clock [52]. The colored panels report the wavelength and the linewidth of the electronic transitions. The Light shift and the Zeeman structure are showed only for the clock states.

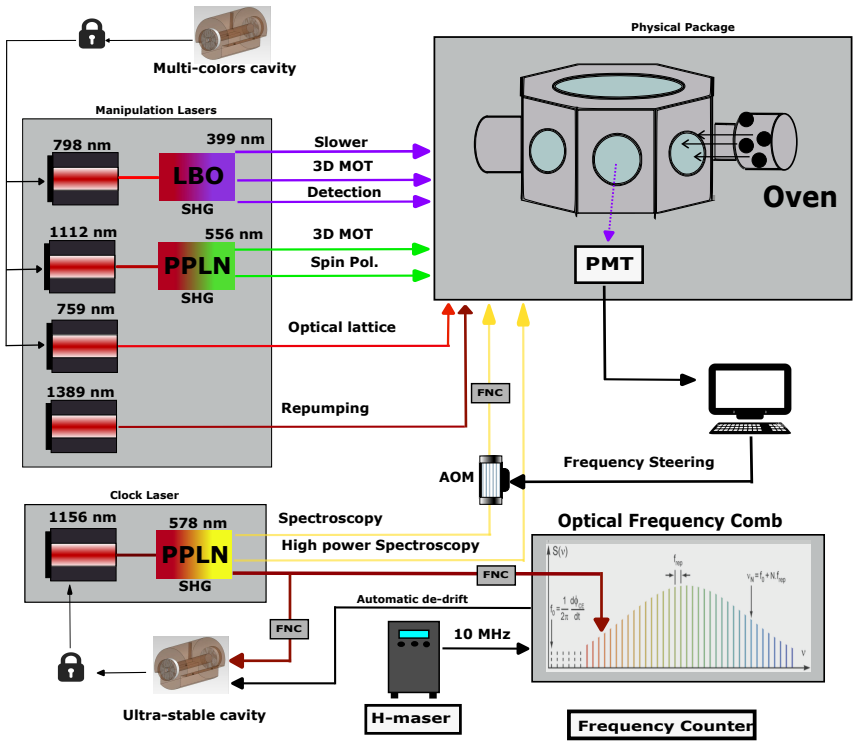


Fig. 2.3 Simplified scheme of the experimental apparatus of the optical lattice clock IT-Yb1. The nonlinear crystal used for second harmonic generation (SHG) are indicated with the code LBO and PPLN. PMT stands for photomultiplier. The code AOM is for the acousto-optic modulator while FNC represents the fiber noise cancellation.

trapped to perform the interrogation, the manipulation lasers, necessary to cool, trap and control the atoms, the clock laser, which is the oscillator whose frequency is stabilized on the atomic reference and then the frequency comb, constituting the counter used to compare the optical frequency with respect to the definition of the second.

2.2.1 Physical package

A vapor of thermal atoms is generated by an home made atomic oven [71] that heats at about 395°C a powder of solid metallic ytterbium: the high temperature atomic gas diffuses into the science chamber collimated through a series of microtubes. A differential vacuum tube separates the oven from the main system, guaranteeing a pressure, respectively, of 5×10^{-9} mbar and 1×10^{-9} mbar measured by two different ion pumps. The science chamber is constituted by an aluminum octagonal structure. The choice of the material comes from the necessity to keep the temperature uniform thanks to the high thermal conductivity and eight platinum thermistors are distributed to measure the temperature, necessary to evaluate the black body radiation emitted by the surrounding environment. The optical access is provided by 6 lateral viewports with 40 mm diameter and two 70 mm diameter vertical windows. All viewports are manufactured with fused silica, sealed to the science chamber with indium wires and present an antireflection coating for 759 nm, 399 nm, 556 nm and 578 nm. Four copper pads are glued onto both the top and bottom windows: they can be electrically fed to behave as electrodes to apply a constant electric field to the atoms. A couple of coils in anti-Helmoltz configuration with axis aligned along vertical direction provides the magnetic field gradient necessary to generate the Magneto Optical trap. They are wound around a 3D-printed structure and they are water-cooled in order to reduce the heat transfer to the chamber. Three additional couples of coils in Helmholtz configuration provide the static magnetic field necessary to compensate for the external fields and to separate the hyperfine structure during clock interrogation.
Blue and green light are overlapped and separated in three back-reflected branches that propagates in the three spatial directions to generate the 3D-MOT trapping the atoms. The MOT is generated inside the thermal atomic flux about 20 cm away from the oven. To increase the number of atoms loaded in the MOT by up to a factor 6, the velocity of the thermal atoms is reduced by a counter-propagating slowing beam

at 399 nm beam, red-detuned respect to the ${}^1S_0 \rightarrow {}^3P_0$ transition.
The optical lattice, trapping atoms in the vertical direction against gravity, is generated back-reflecting an incoming 759 nm laser beam with a 50 mm radius mirror. The waist dimension can be set to 45 µm or 60 µm thanks to two different collimators that couple light to the optical system. It allows to trap atoms in a dipole trap with depth up to 1000 E_r.

2.2.2 Manipulation lasers

399nm Blue laser

The blue light employed to stimulate the ${}^1S_0 \rightarrow {}^1P_1$ electric dipole transition in ytterbium atoms is generated by second harmonic generation (SHG) [72] starting from a 798 nm tapered amplified laser diode TA+DL pro from TOPTICA photonics. Light emitted through an optical fiber is coupled into a bow tie enhancement cavity containing a non-linear LBO crystal [73]. The SHG phase matching conditions are obtained by tilting the angle between the laser beam and the optical axis of the crystal. The cavity is stabilized under resonant conditions operating on a moving mirror mounted on a piezoelectric actuator: by using a Hänsch-Couillaud error signal [74], it makes it possible to keep the cavity length multiple of the fundamental laser wavelength. During the first year of my Ph.D. we implemented an home-made automatic self-lock of the enhancement cavity based on an Arduino™ board. A portion of the blue power after the cavity is measured by a photodiode: in case of loss of the locking (generally because of external perturbations or the limited dynamic of the automatic control) the measured power is lower than a set threshold giving the microcontroller the order to open the servo loop and to scan the cavity length by operating on the piezo voltage. The cavity resonances are detected measuring the emitted power and if it is higher than the locking threshold the Arduino board closes the loop stabilizing the cavity length to maximize the power. The scanning process typically requires 1-2 s and it significantly increases the clock uptime, especially during the unattended measurements.
The laser system has been built on a different table respect to the physical package and the blue light is delivered to the atoms through optical fibers. This optical radiation is frequency stabilized with offset Pound-Drever-Hall technique by coupling about 10 µW of 798 nm light to a multi-color cavity [75]. Starting from about 1.1 W

at 798 nm coupled in cavity, it can emit more than 400 mW of blue power. The maximum power periodically degrades over time due to dust particles burned on the mirrors or crystal surfaces due to the high laser power, but it can be easily fixed cleaning the optical elements with methanol.
The 399 nm laser is separated in three beams coupled in optical fibers and detuned with AOMs: the **Detection** beam is obtained sending few mW resonant with the ${}^1S_0 \rightarrow {}^3P_0$ transition of the ytterbium. About the 60% of the blue power constitutes the **Slowing** beam, about 5 MHz detuned by the resonance, while the rest of the power is sent to the clock to generate the 3 MOT beams, about 20 MHz detuned. Mechanical shutters are mounted on all three branches to cut the optical access.

556nm Green laser

The second manipulation laser, used to trap atoms at colder temperature and to set the atom in the desired hyperfine quantum state m_F, is a green 556 nm laser obtained by frequency doubling a 1112 nm infrared laser. The fundamental laser source is a DL+TA pro from TOPTICA, frequency stabilized with optical cavity with a broadband current control and a slow piezo control. The emission in the infrared domain is doubled by a waveguide PPLN (Periodically Poled Lithium Niobate) non-linear crystal from NTT photonics, whose phase matching conditions are controlled by temperature. Starting from about 200 mW coupled onto the crystal, about 45 mW of green light are emitted. The green radiation is divided in three branches and finely controlled in frequency with AOM. About 10 µW are sent to the multicolor cavity for the **frequency stabilization**, few mW are coupled in fiber to be used for the **spin polarization** process 2.4.1 (moving the whole the ensemble to the same hyperfine state m_F to increase the signal-to-noise ratio of the detection and to reduce collisional effects) while the main fraction of the power is used for the **green MOT**. Mechanical shutters are mounted on the last two branches.

759nm Lattice laser

The 759 nm red laser used to trap atoms at the ytterbium magic wavelength is generated by a commercial Titanium:Sapphire laser Matisse CS from Syrah. This solid-state continuous-wave ring laser is optically pumped by 20 W of a 532 nm

green laser and can emit up to 6.5 W of red radiation. This laser is frequency stabilized on the same multi-color cavity used for the green and blue laser by offset PDH locking, allowing a fine tuning of the laser frequency at the sub-MHz level. Moreover, its frequency is counted on an optical frequency comb, enabling a fine tuning of the laser at the magic frequency and, as a consequence, constituting a reference point to manually remove the cavity drift. Before being delivered to the atoms, the laser emission is filtered by a reflective Volume Bragg Grating from Optigrate [76, 77]. It filters out the eventual Amplified Spontaneous Emission (ASE) emitted by the laser with a broad spectrum far-detuned from the magic wavelength, which could introduce an additional light-shift contribution. By optimizing the filter alignment on the laser emission frequency, light out of the 30 GHz bandwidth is attenuated by about 60 dB [60]. The ASE-induced light shift has been estimated as negligible for this laser system. Observing with an optical spectrum analyzer (OSA) the filter transmission (composed of the out-of-filter radiation and only 1% of the laser emission), ASE spectrum was not detectable and so at least 70 dB below the peak, limit of the OSA [60].

This laser has been implemented during the last year of my Ph.D. to substitute a previously employed Msquared Ti:Sa laser and it constituted a relevant improvement in terms of clock reliability: while the previous lattice laser was the main limitation for the long-term measurements, this one can operate unattended for several days at high power staying locked to the reference cavity, hopefully stringly increasing the uptime for the future measurement campaign.
Power stabilization of the lattice laser on the atoms is provided by an AOM aligned to maximize the transmission of the zeroth diffraction order. It makes it possible to actively control the laser power sent to the science chamber (measured by a photodiode) simply by changing the RF power injected to the AOM.

As an high quality TEM_{00} mode is preferable to generate the optical lattice, the 759 nm light comes from an optical fiber. However, aiming to couple up to 5 W of red laser power, Brillouin scattering forces a limitation of the fiber length to below 3 m [78]. For this reason, this is the only laser placed on the same optical table as the physical package, thus the limitation for mechanical shutters along its path.

1389 nm Repumper laser

The last manipulation laser is an infrared laser diode in butterfly configuration used to pump the atoms from the metastable $^3P_0$ clock excited state toward the ground state. It is a manifactured by pigtail distributed feedback diode laser from NKT photonics emitting about 20 mW of 1389 nm power directly coupled in fiber. Its frequency is not stabilized but only tuned by temperature and current. Under stationary condition it is subjected to a drift of about 600 kHz/h.

2.2.3 Clock laser

The local oscillator used to probe the frequency of the ytterbium $^1S_0 \rightarrow ^3P_0$ clock transition is a 578 nm yellow laser. It is generated by SHG starting from a TOPTICA DL+TA pro 1156 nm laser, frequency doubled through a PPLN crystal from NTT photonics controlled in temperature. From 350 mW of infrared power about 50 mW of 578 nm radiation are emitted. The yellow laser, employed for the clock transition spectroscopy, is separated in two branches: the so-called **high-power** spectroscopy, that delivers about 5 mW of power to the clock and it is employed for sideband spectroscopy and sideband cooling (2.4.2), and the **low power spectroscopy** branch, responsible for the Rabi interrogation of the clock transition. Both branches are transferred to the atoms by optical fiber and the latter presents power stabilization and active fiber noise cancellation [79]. When the clock is operating, the low power spectroscopy branch is actively frequency-steered to keep it resonant with the atomic resonance. Just after of the non-linear crystal a dichroic mirror separates the yellow light from the residual infrared radiation, which is distributed with three optical fibers: two toward the two combs present at INRiM while the last one goes to the ultra stable cavity (after passing through a double-pass AOM employed for fine frequency tuning and removal of the cavity drift). Fiber noise cancellation has been implemented on all three fiber links.
The frequency of the 1156 nm fundamental laser is measured on the frequency combs, referenced by a 10 MHz signal from a hydrogen maser.



Fig. 2.4 Internal of the acoustic enclosure containing cavity inside the vacuum can and the locking optics. The breadboard is mounted on an platform to actively cancel the vibrations.

Ultrastable cavity

The IT-Yb1 local oscillator is frequency stabilized on a commercial optical cavity, shown in picture 2.4, from Stable Laser Systems. This plano-concave cavity presents fused-silica mirrors with high-reflective coating for 1156 nm, separated by a 10 cm long Ultra-Low-Expansion glass (ULE) spacer mounted on a Zerodur block. Two thermal shields stabilize the temperature at the zero crossing temperature of 28.5°C. The whole system is contained in a vacuum chamber, keeping the pressure lower than 2×10^{-7} mbar, and mounted on a breadboard placed on an active vibration-isolating platform (DVIA-T 45). Moreover an additional isolation from external vibration is provided by an acoustic enclosure from Herzan (AEK-2002).
The clock laser is stabilized by Pound-Drever-Hall technique using a TOPTICA FALC analog controller module [80]. The cavity flicker phase-noise limit has been estimated at 1×10^{-15} from a three-corner-hat measurement.
We implemented an active removal of the natural cavity drift locking the clock laser frequency to an hydrogen maser. Measuring the beatnote between the comb and the 1156 nm laser, a digital lock stabilizes it at about 95.3 MHz, transferring the long-term stability of the H maser referencing the comb. This lock has to be slow enough (about 300 s of integration time) to remove the drift without affecting the better short-term stability of the cavity.

2.2.4 Clock cycle

The typical IT-Yb1 clock cycle operation is represented in figure 2.5. First atoms are cooled and trapped in two stage Magneto Optical Trap (MOT) [81–83] obtaining a confined atomic cloud with a temperature of a few μK. The collimated atomic flux coming from the oven is slowed down with a counter-propagating slowing beam at 399 nm, reducing the velocity of the thermal beam. About 2×10^5 atoms at 10 mK are collected in the blue MOT, obtained with three counter-propagating orthogonal laser beams at 399 nm. When the number of trapped atoms is sufficient, the blue beams are turned off, generating the green MOT with three 556 nm laser beams overlapped with the blue ones. Atoms are thus cooled to temperature of few μK, allowing the load of cold atoms into the optical lattice. To increase the number of transferred atoms, the green MOT is not suddenly turned off but the power, the red-detuning and the gradient of magnetic field are reduced in two stages. The

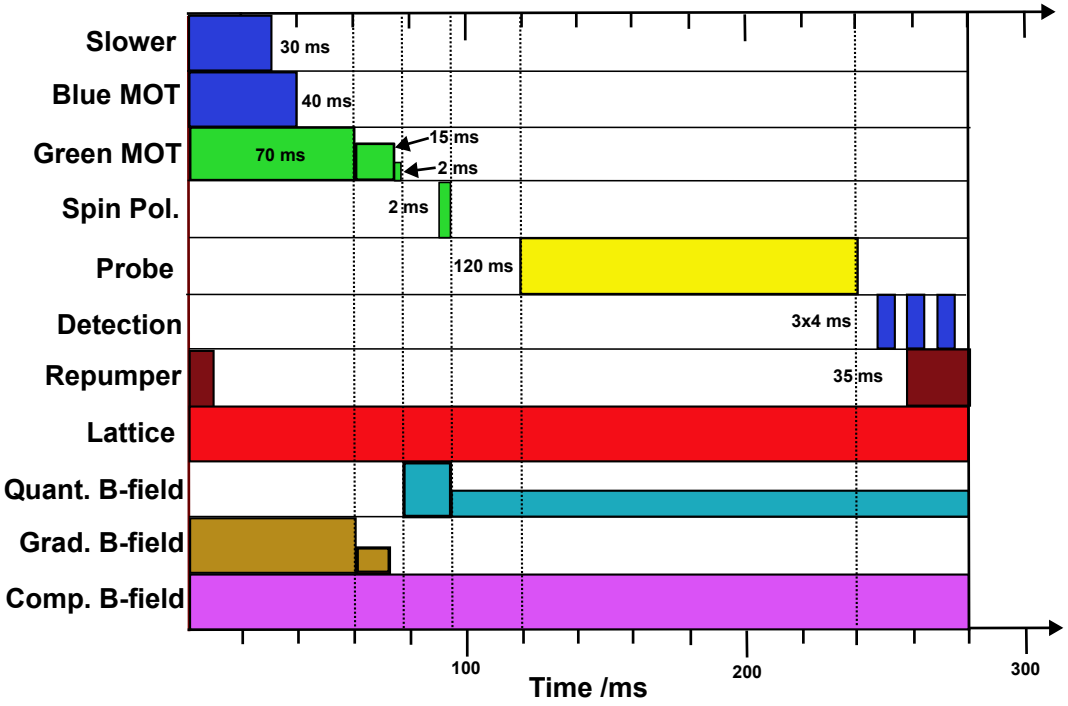


Fig. 2.5 Typical clock sequence in IT-Yb1. The colored bars represents the duration of laser pulses and different magnetic fields used to trap or interrogate atoms while the height indicate the relative intensity. The time necessary for a single clock cycle is about 300 ms, whose 120 ms of probing through Rabi Spectroscopy.

number of trapped atoms can be controlled changing the duration of the slower or the blue MOT.
The vertical optical lattice is always kept on and overlapped with the center of the MOT to maximize the number of trapped atoms. While the atoms populate the optical lattice sites acquiring thermal equilibrium, the quantization magnetic field is turned ON: then a state preparation phase follows (described in detail in section 2.4) to prepare the internal atomic state optimizing the clock interrogation. Clock transition is probed with a Rabi spectroscopy applying a π-pulse 120 ms long. In alternative, about 2 mW of 578 nm light can be employed to probe a sideband spectroscopy of the clock transition.

After that, the detection phase follows, with a series of three 399 nm pulses measuring the fluorescence with a photomultiplier perpendicular to the detection beam: the first pulse measures the atoms not excited while the second the background level. Before the third pulse, the repumping laser is turned on to bring the atoms excited on the $^3P_0$ level toward the ground state, thus measuring the fluorescence of the atoms excited by the 578 nm probe.

The detection process is destructive, requiring a restart of the loading phase for a new interrogation. During clock spectroscopy the constant quantization magnetic field is kept on to separate the hyperfine structure $m_F \pm 1/2$: the two hyperfine π transitions are probed in two consecutive cycles and from the average frequency it is possible to remove the first-order Zeeman shift. From the measure of the excited fraction, a feedback loop tries to keep the local oscillator frequency locked at half of the maximum excitation probability (side-of-the-fringe stabilization). This frequency steering is done through an AOM.

2.3 Uncertainty budget

In optical clocks, several physical effects contribute to shifting the frequency of the clock transition from the unperturbed conditions. These effects must be minimized and evaluated and they contribute to the determination of the clock accuracy budget. In this section I will discuss the systematic shifts affecting IT-Yb1, reported in Table 2.1 with the relative frequency shift and the corresponding uncertainty, and how they have been estimated. The total systematic shift has been evaluated with a relative

uncertainty of 1.9×10^{-17}, limited by the Blackbody radiation shift and the lattice light shift. Additional information can be found in previous theses [66, 67].

Effect	$\Delta\nu/\nu$ $/10^{-17}$	u_{rel} $/10^{-17}$
Density shift	-0.5	0.2
Static Stark shift	-1.7	0.2
Fiber links	0.05	0.10
Lattice shift	1.5	1.2
Probe light shift	0.04	0.03
Zeeman shift	-3.12	0.02
Blackbody radiation shift (room)	-234.9	1.2
Blackbody radiation shift (oven)	-1.3	0.6
Background gas shift	-0.5	0.2
Other shifts	-	0.3
Gravitational redshift	2599.5	0.3
Total	2359.1	1.9

Table 2.1 IT-Yb1 uncertainty budget. The physical effects concurring introducing a systematic frequency shift are here summarized with the estimated correction and the associated uncertainty. Other shifts include effects such as servo errors, fiber links, AOM switching, and line pulling will be described in the dedicated subsection.

2.3.1 Density Shift

In optical clocks a large amount of atoms are trapped in the optical lattice to interrogate the clock transition. If it improves the stability of the measurement, a high atomic density increases the probability of collisions between different atoms, shifting the atomic transition from the unperturbed conditions.

The main source of these effects derives from the cold collisions among atoms trapped in the same lattice site. From the theory, for the fermionic ^{171}Yb isotope the Pauli exclusion principle suppresses the strong *s-wave collisions* if the atoms are in the same internal quantum state [84], leaving only a residual contribution from *p-wave* scattering that can be mitigated by operating at low temperatures. In real systems both these effects contribute to the collisional shift because of a non-zero atomic temperature, inhomogeneous atomic preparation or evolution of the atomic state during the interrogation [61, 85].

Assuming that the density shift is proportional to the number of atoms trapped in the

optical lattice [86], its characterization is carried out by alternating clock cycles with high and low atomic density and probing the clock frequency. To keep the trapping conditions constant, the difference in the atom number is obtained only by changing the time the 399 nm slowing beam is kept on, while maintaining the cycle duration equal. This systematic effect must be characterized in real time due to its dependence on several experimental conditions influencing the trapping condition that make it difficult to reproduce, such as the trap depth [86], the fraction of population in a specific hyperfine state [87], the mean excitation fraction [88], the Rabi-spectroscopy pulse-area [89] and the density of the last stage of the green MOT [66].
The density shift in IT-Yb1 has been evaluated by running interleaved measurements in similar trapping conditions locking the clock line at 50% of the maximum excitation probability (condition that minimizes the magnitude of this systematic effect [66]) and reproducing the measurement at different trap depths. At the typical lattice depth $D = 100E_R$ the average density shift is $\delta\nu_{density}/\nu_0 = -5(2)\times10^{-18}$[67]. Figure 2.6 shows the interleaved instability for more than 500 000 s of density shift measurement in term of overlapping Allan deviation (OADEV).

Some solutions are currently being investigated in IT-Yb1 to further reduce the magnitude of the density shift and its uncertainty for the next measurement campaigns: after the change of the 759 nm laser we increased the lattice waist from 45 to 60 µm reducing the density of the trapped atoms. Then, decreasing both the longitudinal and the radial temperatures will have the dual effect of reducing the probability of collisions and making it possible to have a significant amount of atoms at lower lattice depth [90, 91].

2.3.2 Static Stark Shift

The DC Stark shift [92] arises in presence of an undesired static electric field with intensity δE, inducing a perturbation on the clock transition frequency of a quantity: $\delta\nu_{DC\,Stark} = -\frac{1}{2}\Delta\alpha(\delta E)^2$, [93, 94] where $\Delta\alpha$ is the difference in static electric dipole polarizability of the two clock states. This systematic effect can be evaluated by interleaved measurements alternating a controlled external electric field $E_\pm$ in opposite directions and measuring the induced frequency shift $\Delta\nu_\pm$: The frequency

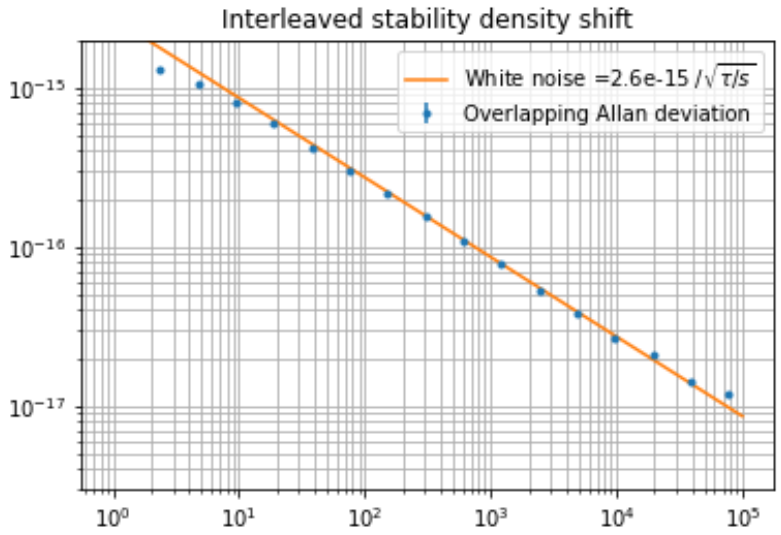


Fig. 2.6 Overlapping Allan deviation of the interleaved density shift measurements measured between March and April 2023 for about 550 000 s. From the fit we detected a white noise of 2.7×10^{-15} at 1 second.

shift induced by the stray electric field can be estimated as [93]:

$$\delta\nu_{DC\,Stark} = \frac{(\Delta\nu_+ - \Delta\nu_-)^2}{16\Delta\nu} \tag{2.1}$$

where $\Delta\nu$ is the average shift. In case the atoms are well shielded [92] by parasitic electric fields (δE=0), the perturbations induced by the external field are equal; otherwise the vector sum $\vec{E_\pm} + \delta\vec{E}$ makes the measured shifts $\Delta\nu_+ \neq \Delta\nu_-$ when the field is alternated in direction, evidencing the presence of this static contribution.

The evaluation of the DC Stark shift on IT-Yb1 is performed thanks to a combination of eight electrodes applied symmetrically on the horizontal windows of the science chamber [54]: It is possible to set the voltage of each electrode from -175 V up to 175 V to generate a resulting electric field that can be oriented in three orthogonal directions with positive or negative sign. Alternating interleaved measurements with opposite directions of the externally applied electric field enables investigating the presence of stray electric fields in all three space directions.
In particular, we detected a static electric field well aligned to the slower-oven direction, whose magnitude does not reveal decay in time. We interpreted its origin from static charges emitted by the oven and accumulated on the windows, but was

not possible to remove them and they are not subjected to some sort of time decay. The solution to compensate for this systematic shift is to measure its magnitude with the scheme previously described and then apply a constant DC field with the same intensity but opposite direction. This compensation enables a control on this effect at the level of 10^{-17}, but effective cancellation requires monitoring the intensity of the parasitic electric field at least twice a week due to its unpredictable variation over time. The field detected in the other spatial directions is smaller and does not require external compensation.

From the average of the frequency perturbation measured along the three spatial directions and applying the compensation only to the oven-slower axis, the total DC Stark shift has been evaluated at $\frac{\delta \nu_{DC\,Stark}}{\nu_0} = -1.66(19) \times 10^{-17}$. There are some possible solutions that could be implemented to cancel out this phenomenon, such as the implementation of a Faraday cage to shield atoms from static electric fields[92], the coating of the windows with conductive layers (e.g. indium tin oxide ITO) to remove eventual static charges or designing the science chamber with smaller windows and farther away from the atoms.

2.3.3 Lattice light shift

The lattice light shift is a form of AC Stark shift [95], a perturbation induced by the atom-light interaction that shifts and broadens the energy levels, induced by the lattice laser used to trap cold atoms.

In optical lattice clocks, the optical lattice is typically tuned at the so-called magic frequency [59], at which the electric dipole polarizability α_{E1} is equal for both two clock states, leaving the transition unperturbed. Despite it being the dominant effect, the electric dipole coupling is not sufficient to describe the light shift with high accuracy, but also other "non-magical" terms like electric quadrupole ($E2$) and magnetic dipole ($M1$) coupling or hyperpolarizability (β), related to the fourth-order electric dipole coupling with the lattice field [96]. These effects induce a light-shift not linearly dependent on the lattice depth and prevent complete cancellation [97].

Instead of using the typically model employed [87, 98–100], in IT-Yb1 we evaluate the lattice shift perturbation applying the expression recently proposed by NIST [101, 96]:

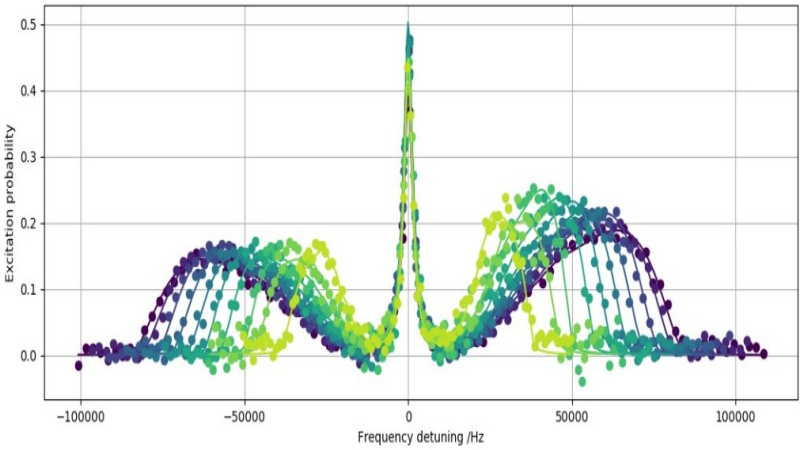
$$h\delta\nu_{LS} = -U_0\frac{\Delta\alpha_{E1}}{\alpha_{E1}}X - U_0\frac{\Delta\alpha_{E2M1}}{\alpha_{E1}}Y - U_0^2\frac{\Delta\beta}{\alpha_{E1}^2}Z \tag{2.2}$$

where $\Delta\alpha$ and $\Delta\beta$ are the differences in polarizability between the two clock states evaluated for different polarizability contributions and the factors X,Y,Z are dimensionless factors representing the spatial portion of the trapping potential explored by the atoms. These factors are limited in the interval [0,1] and depend on the lattice depth and the mean longitudinal and radial vibrational states of the system $\langle n_z\rangle$ and $\langle n_\rho\rangle$, related to the temperature. Intuitively, colder atoms populate the lowest trap levels $n_z = 0$, laying at the bottom of the trap where they are subjected to the maximum confinement potential (X,Z=1;Y=0), while atoms populating the more energetic states explore a wider portion of the lattice site, thus they undergo a lower average potential. The main advantage of this technique arises if the temperature of the atomic ensemble depends linearly from the lattice depth $T \propto U_0$: in this case the parameters X,Y,Z are no longer function of the lattice depth U_0 becoming constants. Follows that the expression 2.2 becomes:

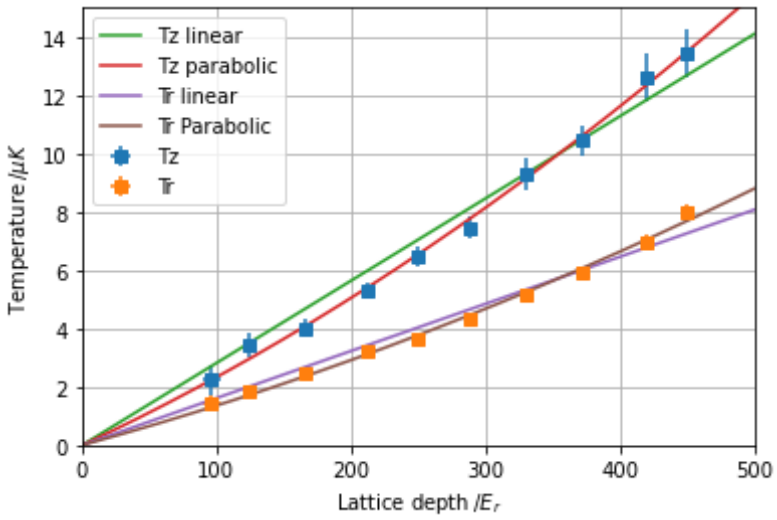
$$\frac{\delta\nu_{LS}}{\nu_{clock}} = -\alpha^* U_0 - \beta^* U_0^2 \tag{2.3}$$

where α^* and β^* are the polarizability and hyperpolarizability parameters, non-dependent on the lattice depth, making the lattice light shift described by a parabola with U_0.

Before applying this formula, it is necessary to verify the linear dependence of the atomic temperature on the lattice depth: it is verified by performing sideband thermometry [102] at different trap depths as shown in Figure 2.7a. This characterization is controlled daily making it possible to correct eventual deviations from linearity changing the trapping conditions, for example, by operating on the green MOT frequency. In a first approximation, the atomic temperatures in IT-Yb1 closely follow a linear trend especially at low depths, but, as evidenced in figure 2.7b, the addition of a quadratic parameter to the fitting function provides a better description. This implies the addition of a correction to equation 2.2 to describe the deviation from the model. This also introduces an additional uncertainty [67], which has been estimated as the typical error from the model after a Monte Carlo simulation.
The differential lattice light shift can be experimentally evaluated by interleaving



(a)



(b)

Fig. 2.7 (a) Sidebands spectroscopy of the clock transition acquired at different lattice depth (see bottom panel) with sideband fit evidenced by solid lines. (b) Plot of the corresponding longitudinal (blu) and radial (orange) temperature varying the lattice depth. Continuous curves compare the linear and parabolic fit of the temperature evolution.

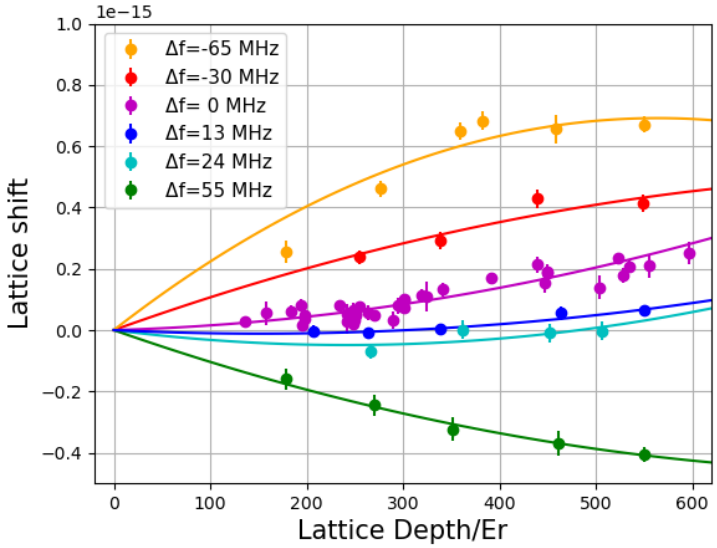


Fig. 2.8 Measured lattice light shift varying the lattice depth and corrected for the density shift. Every colored curve have been acquired at different detuning from the set "magic" working condition 394 798.267 GHz, represented by the purple data in the graph. Courtesy from Irene Goti [67].

measurements at high and low lattice depth, where the low level is generally the typical working depth, set to 100 E_R. The shift measured with this technique has to be corrected for the density shift, which is strongly dependent on the lattice depth, as described in Section 2.3.1. The experimental values are shown in graph 2.8 for different detuning from the magic frequency.

We assumed as the operating magic frequency the value 394 798.267 GHz represented by the purple curve in Figure 2.8), following the one proposed by *Brown et al.* [101]. By fitting the data corresponding at the set working point with the previously described parabolic model it is possible to extract the parameters α^* and β^* necessary to calculate the lattice perturbation and its uncertainty at 100 E_r as $\delta\nu_{LS}/\nu = 1.5(2) \times 10^{-17}$. We decided to consider an additional uncertainty contribution, coming from the deviation from the linear model and conservatively estimated at 1×10^{-17}. The uncertainty affecting the lattice shift has been strongly mitigated compared to the previous evaluations in IT-Yb1 [52, 53] due to the reduction of the operational lattice depth due to the introduction of a vertical confinement of the atoms [67]. In 2025 we are going to evaluate again this shift thanks to the new lattice laser (installed in 2024), which makes it possible to explore higher trap depths

up to 1000 E_r and so reducing the uncertainty from the parabolic fit. Furthermore, we observed that the integration of sideband cooling technique [91] in the trapping process not only makes possible to trap a significant amount of atoms at lower trap depth (down to 50 E_R or lower), but also reduces the deviation from the linear model of the temperature, increasing the accordance with the theoretical model and consequently bringing down the additional uncertainty.

2.3.4 Black Body Radiation Shift

As IT-Yb1 is operated at room temperature, the blackbody radiation emitted by the surrounding environment at finite temperature induces a Stark shift on the atoms. As the thermal radiation spectrum at room temperature ranges in a low frequency interval far from the the typical values of the atomic electric dipole transitions, the atomic electric polarizability can be considered in first approximation static α_0 with a small correction η_{BBR}, that keeps in account the dynamic behavior and depends both on the temperature and the atomic properties [92, 103]. The BBR-induced frequency shift respect to the clock transition calculated at temperature T_0 is thus [94, 104]:

$$\Delta\nu_{BBR} = -\frac{\Delta\alpha_0}{h}\langle E^2_{BBR}\rangle_{T_0}(1+\eta_{BBR}(T)) \tag{2.4}$$

where $\Delta\alpha_0$ is the difference in static polarizability between the clock states (experimentally measured for ^{171}Yb [94]) and $\langle E^2_{BBR}\rangle_{T_0}$ is the average thermal electric field emitted by the environment at temperature T_0, calculated from the measured temperature of the surrounding environment.

As shown in table 2.1, in IT-Yb1 the evaluation of the BBR shift takes in account two separate contributions: the first comes from the physical package around the atoms, dominated by the aluminum science chamber and the viewports, the second from the oven used to vaporize the atomic vapor. The higher uncertainty is associated to the evaluation of the BBR from the vacuum chamber: its temperature is monitored by ten platinum thermistors placed symmetrically on the external surface. The resistance of each sensor is measured every 80 s via 4-wires reading and registered. As there is no possibility to control uniformly the temperature of the vacuum system except for the water cooling applied to the MOT coils we can only assume that the

cell temperature follows a rectangular probability distribution between the minimum and the maximum value measured by the thermistors. We assign as most probable temperature the average between the two extreme values $T = (T_{max} + T_{min})/2$ and the associated uncertainty $uT = (T_{max} - T_{min})/\sqrt{12}$ [105]. The typical relative BBR shift induced by the room is $\delta\nu_{BBR}^{room}$=-234.9(12) $\times 10^{-17}$ and there is no possibility to reduce its uncertainty because the main part comes from the spread of the measured temperatures rather than the accuracy of the sensors[53]. The only way to strongly overcome this effect is to make structural changes to the physical package, such as introducing a BBR shield, to keep the temperature around the atoms more uniform. The second source of thermal radiation is the oven at about 395°C, whose radiative contribution is not negligible because the atoms are trapped in front of the atomic flux coming from the oven. The radiation emitted by the oven has to be scaled for the portion of solid angle accessible to the atoms and the average intensity of electric field can be calculated knowing the oven temperature, measured by a thermocouple inside the oven. The relative shift has been estimated as $\delta\nu_{BBR}^{oven}$=-1.3(6) $\times 10^{-17}$, whose uncertainty derives mainly from the evaluation of the solid angle and from the determination of the oven temperature[67]. Even this effect is not suppose to be cancelled in our experimental system without structural modifications: among the feasible solutions we could integrate in future we are investigating to place an atomic shutter, shielding the solid angle from the oven during the interrogation or interrogating the clock transition far from the oven line-of-sight trapping the atoms first in a 2D MOT [106, 107].

2.3.5 Zeeman shift

Due to the well-known Zeeman effect, in presence of an external magnetic field atomic energy levels are shifted depending on their hyperfine states. The shift is quantified by $\Delta E_Z = g_F \mu_B B m_F$, where μ_B is the Bohr magneton, B is the intensity of the magnetic field and g_F is the Landé g-factor. In case the two clock states experience different bending, the transition frequency is affected by a Zeeman shift. In Fermionic atoms like ^{171}Yb (I=1/2), this systematic shift can be neglected with a simple technique: spectroscopy of the clock transition is probed with a π transition$|g, m_f = \pm 1/2\rangle \rightarrow |e, m_f = \pm 1/2\rangle$ conserving the same hyperfine state and as the two hyperfine states m_F=+1/2 and m_F=-1/2 are subjected to a Zeeman shift with same magnitude but opposite direction, this effect can be cancelled at the first

order interrogating in succession the two opposite states and then considering the average frequency [108].

However, quadratic Zeeman shift $\delta\nu_Z^{quad} = a_Q B^2$ affects both Zeeman levels in the same way, so it cannot be eliminated with the previous technique. Knowing the value of the quadratic coefficient, estimated by NIST as a_Q=-6.095(7) Hz/mT^2 [43], and the intensity of magnetic field it is possible to estimate the magnitude of this shift. The only way to measure the intensity of magnetic field inside the science chamber is measuring the linear Zeeman shift induced on clock transition. Knowing $\delta\nu_Z = \pm a_L B$, with $a_L(m_f = \pm 1/2)$=1995.16(2) Hz/mT [43], we typically apply about 50 µT of constant magnetic field parallel to the probe light polarization observing a split of about 100 Hz from the unperturbed conditions. It is assumed to be the only magnetic field perturbing the atoms, as the external background is canceled with three pairs of compensation coils.

In addition, an additional component of magnetic field is originated by the lattice vector light shift: a residual elliptical polarization of the lattice laser beam, induces an apparent magnetic field which sums itself to the external one [66, 109] and whose intensity depends on the lattice power. In IT-Yb1 this effect has been observed and is conservatively estimated by assigning 0.4 Hz of uncertainty to the Zeeman splitting measurements. As a consequence, it means a relative uncertainty contribution in the clock transition of 1×10^{-19} which makes it comparable to the uncertainty of the applied magnetic field.
Under these considerations, the total Zeeman shift has been evaluated as $-3.12(2) \times 10^{-17}$ under typical conditions.

2.3.6 Probe Light shift

Although in two-level atomic model a resonant photon should not induce any light-shift effect [95], the probe laser itself can weakly couple with other atomic transitions involving the clock states, generating a so-called probe light-shift [43]. The magnitude of this effect is related to the power of the probe pulse. As the clock transition is interrogated with Rabi spectroscopy with a π-pulse of duration τ, the clock laser intensity required scales with the Rabi time as $1/\tau^2$. Increasing the interrogation time is, therefore, beneficial not only to reduce the Dick effect that limits the clock

instability, but also to reduce the probe laser intensity. We evaluated the probe light shift magnitude in IT-Yb1 as $\delta\nu_{LS}^{probe}/\nu = 4(3)\times10^{-19}$ by rescaling for 120 ms of Rabi time the calculations done in *McGrew et al.* [43], who reported a relative frequency shift $2(1)\times10^{-20}$ for T_{Rabi}=560 ms. The associated uncertainty has been conservatively overestimated.

2.3.7 Gravitational redshift

As is well known from general relativity, the gravitational potential affects the flow of time and consequently the frequency of a clock [110]. This phenomenon is also called gravitational redshift and the relative frequency shift induced by the Earth potential is on the order of 1×10^{-16}/m, easily detected and measured by optical clocks [23, 24]. At the same time, what was previously considered only a perturbation from the unperturbed conditions, especially critical during clock comparisons, can now be measured by optical clocks with an accuracy that promises to surpass the traditional techniques, opening the road to clock geodesy [43]. As established by CGPM 2018, the unperturbed frequency of an atomic transition must be evaluated with respect to the conventional gravitational potential W_0=62 636 856.0 m^2/s^2 [111]. This involves the requirement to keep in consideration this effect not only in the clock comparisons, where each clock is placed in a different reference frame, but also during measurements involving a single clock.

In IT-Yb1 this shift has been evaluated measuring the difference in gravitational potential compared to the geoid as $W_{IT-Yb1}-W_0$=2336.28(25) m^2/s^2 [53] from which a fractional correction for the gravitational redshift of $\delta\nu^{redshift}/\nu$=2599.5(3)$\times$ 10^{-17}.

2.3.8 Background gas shift

Beyond the cold collisions occurring between atoms trapped in the optical lattice which give origin to the density shift 2.3.1, collisions with thermal atoms diffusing into the science chamber can introduce a systematic effect. These particles, mainly hot Yb atoms emitted by the oven and H_2 molecules permeating the vacuum system or degassed by steel, compose the background gas which limits the vacuum level of the science chamber. Background collisions have the additional effects of scattering

atoms out of the lattice, so measuring the lattice lifetime can provide an insight into the collisional rate: the background gas shift, indeed, inversely scales with the trap lifetime [112, 43] with a proportionality factor dependent on the different kinds of collisions occurring. This factor has been calculated as -1.6(3) $\times 10^{-17}$ s [53] from the C_6 coefficients [113] theoretically calculated from Yb-Yb [114] and Yb-H_2 [69] interactions. Taking into account a typical measured lifetime of $\tau_{lattice}$=2.7(5) s^{-1}, the background gas collision shift has been estimated as $\delta\nu_{coll}^{Bck}/\nu$=$-0.5(2)\times 10^{-17}$.

In general, the only way to reduce this effect is increasing the vacuum level of the physical package. While hydrogen molecules permeating the steel can be limited by using a getter on the vacuum system, the degassing from the steel is minimized with a long and high-temperature baking. Concerning collisions with hot Yb atoms from the oven instead, a possible solution can be to move the science chamber far from the line of sight of the oven flux, as described in subsection 2.3.4.

2.3.9 Other effects

Other physical effects that contribute the shift of the clock transition frequency are summarized here. As probe light is generated on an optical bench different from the physical package, 578 nm light is delivered to atoms is transmitted via a polarization-maintenance optical fiber. Any variation of the fiber optical path induced by vibrations, temperature fluctuations or mechanical stresses is responsible for introducing an additional phase noise in the probe laser, generating a frequency shift induced by **fiber links**. In IT-Yb1 fiber phase noise accumulated along the path is actively compensated [79]. In this way, we estimate a residual shift compatible with zero assigning an uncertainty at the level of 1×10^{-18}. The **Servo Error** is induced by the servo loop locking the local oscillator to half the atomic resonance [67]: a slow lock makes it possible to compensate the drift of the ultrastable cavity and at the same time keeping the LO frequency deviation from the locking point consistent with zero with relative uncertainty of 3×10^{-18}. Another uncertainty source derives from the **AOM switching** [115]. To avoid thermal effects on the clock AOM and to keep the fiber noise cancellation loop locked as well, the 578 nm probe light is constantly maintained switched-ON and just detuned out-resonance when the clock transition is not interrogated. This AOM frequency shift introduces a small phase shift on the clock laser, generating a frequency shift also in the measured frequency at the level of 10^{-18}. In addition, this phase shift is detected by the fiber

noise cancellation system and compensated as real phase noise. This effect is limited in IT-Yb1 periodically alternating the sign of the frequency switching from the resonance, averaging to zero the detected phase shift. For this reason, the systematic frequency shift has been estimated as null with an associated uncertainty of 1×10^{-18}. The **Line Pulling** effect derives from the presence of other atomic transitions whose excitation probability is non-zero at the clock frequency, shifting the unperturbed transition frequency. In particular, for ^{171}Yb ($I = 1/2$), the closest and most relevant effects derive from $\sigma_{\pm}$ transitions occurring between hyperfine levels. The induced line pulling can be readily eliminated by filtering the probe laser polarization with a Glan-Thompson polarizer and preparing the atomic ensemble in the same spin state, allowing only the clock π transitions. The systematic frequency shift that results from line pulling has been evaluated as zero with a fractional uncertainty of 2×10^{-19}. Another systematic effect derives from the atom tunneling between lattice sites [67]: the vertical lattice confines atoms along gravity [116] introducing a gravitational energy difference between two contiguous lattice sites that suppress tunneling sufficiently to be considered negligible. For this reason, it has not been taken into account in IT-Yb1 uncertainty budget.

2.4 State preparation

As previously described, the state preparation is a fundamental step in interrogating the clock transition with high signal-to-noise ratio and in strongly mitigating the systematic effects. During my Ph.D. I worked optimizing the spin polarization process in IT-Yb1 to move the atomic ensemble in the desired hyperfine quantum state limiting the losses of trapped atoms and I implemented a longitudinal sideband cooling protocol to reduce the atomic temperature in the lattice axial direction, introducing a new level of control on the trapped atoms.

2.4.1 Spin Polarization

In order to maximize the signal-to-noise ratio of clock spectroscopy and to strongly suppress s-wave collisions (see 2.3.1), spin polarizing the atomic ensemble to a single hyperfine quantum number of the ground state $|^1S_0, m_F = \pm 1/2\rangle$ plays a crucial role. As already described, ^{171}Yb is a fermionic atom with nuclear spin $I = 1/2$. This

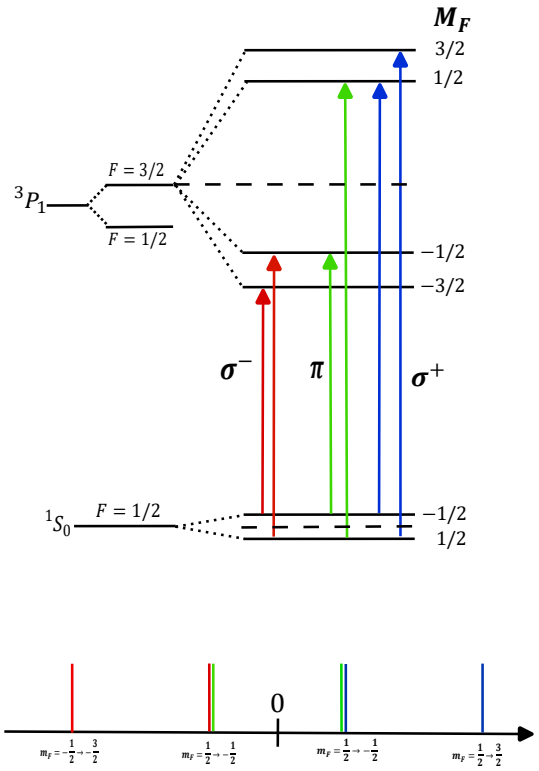


Fig. 2.9 Relevant hyperfine levels involved in the spin polarization process. The Zeeman splitting of the energy levels is not in scale

means that under a constant magnetic field the spectroscopy signal splits into several lines that reveal the hyperfine structure depending on the m_F number. Atoms in the ground state have the same probability of populating either the quantum state $|^1S_0, m_F = 1/2\rangle$ or $|^1S_0, m_F = -1/2\rangle$, so the spectroscopic signal of the two clock transitions when separated by a magnetic field will exhibit a maximum excitation of 0.5. As shown in Figure 2.9, it is possible to increase the signal-to-noise ratio by polarizing atoms in the same hyperfine state with the excitation of a σ transition $|m_F = \pm 1/2\rangle \rightarrow |m_F = \mp 1/2\rangle$, which changes the hyperfine state. These can be stimulated by setting light polarization perpendicular to the quantization magnetic field and detuning the frequency by an appropriate amount.
In IT-Yb1 we apply a spin polarization process by exciting the 556 nm intercombination transition between the $^1S_0$ and P_1 levels. The 187 kHzlinewidth is narrow enough to resolve the Zeeman transitions even with a limited magnetic field, and the decay rate is sufficiently high to repeat the excitation-decay cycle in a short time while limiting the loss rate. After excitation, the atoms preferentially decay to the ground state with Δm_F=0. A non-negligible branching ratio at $\Delta m_F = \pm 1$ does not constitute an issue for moving the ensemble into the desired spin configuration if the laser pulse is long enough.

As already introduced in section 2.3.5, under a constant magnetic field the hyperfine energy levels are shifted of a quantity:

$$\Delta E_Z = h\Delta\nu_Z = g_F \mu_B B m_F \tag{2.5}$$

where B is the magnetic field intensity, $\mu_B \approx h{\cdot}14\,\mathrm{MHz/mT}$ is the Bohr magneton and g_F is the Landè g-factor. The latter depends on the quantum number of the atomic state as:

$$g_F = g_J \frac{F(F+1) - I(I+1) + J(J+1)}{2F(F+1)} - g_I \frac{\mu_N}{\mu_B} \frac{F(F+1) + I(I+1) - J(J+1)}{2F(F+1)} \tag{2.6}$$

where $\mu_N = h{\cdot}7.62\,\mathrm{kHz/mT}$ is the nuclear magneton and g_I=0.4919 [117] for Yb atom. For the ground state $^1S_0$ the first term of equation 2.6 is null, so $g_F(^1S_0) = g_I \frac{\mu_N}{\mu_B}$ while for the excited state the second term is negligible, as μ_N is about 2000 times smaller than μ_B. Knowing $g_J = 1 + \frac{J(J+1)+S(S+1)-L(L+1)}{2J(J+1)}$, for the $^3P_1$ state g_J=3/2. Therefore, g_F can be evaluated for the excited state considering its hyperfine

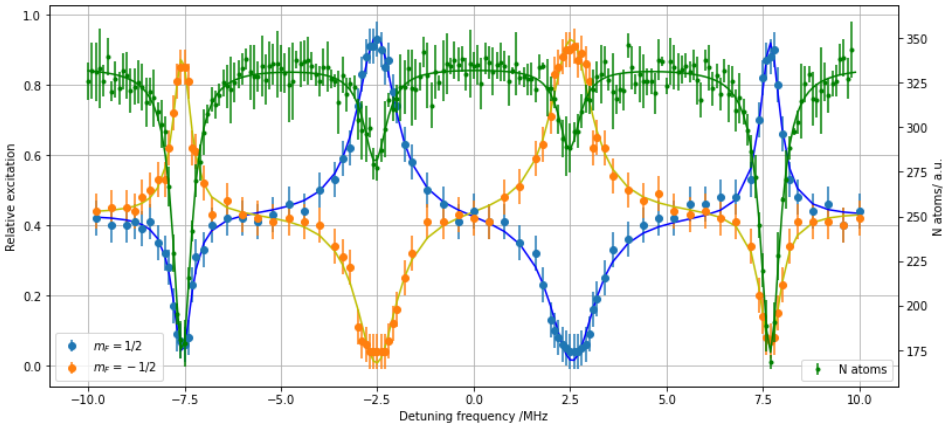


Fig. 2.10 Blue (Yellow) line represents the measured excited fraction in the hyperfine state $m_F = 1/2$ ($m_F = -1/2$) changing the detuning of the spin-polarization beam. Green line is the Zeeman spectrum of the $^1S_0 \rightarrow ^3P_1$ intercombination transition observing the number of atoms trapped in lattice. All three lines have been obtained with a fit containing 4 Lorentzian distributions.

multiplicity as $g_F(^3P_1, F = 3/2) = 1$ and $g_F(^3P_1, F = 1/2) = 2$. Follows that the Zeeman shift of the ground state is almost negligible compared with the $^3P_1$ state, making the π transitions close in frequency with the σ ones. Table 2.2 reports the Landé g-factors calculated for the relevant hyperfine states involved in the spin polarization process with the corresponding linear Zeeman shift, evaluated through 2.5.

State	L	S	J	I	F	m_F	g_F	$\Delta\nu_Z/B$ (kHz/μT)
$^1S_0$	0	0	0	1/2	1/2	$\pm$1/2	$-g_I\frac{\mu_N}{\mu_B}$=-2.68e-4	$\mp$187.6e-5
$^3P_1$	1	1	1	1/2	3/2	$\pm$3/2	1	$\pm$2.1e1
$^3P_1$	1	1	1	1/2	3/2	$\pm$1/2	1	$\pm$7
$^3P_1$	1	1	1	1/2	1/2	$\pm$1/2	2	$\pm$1.4e1

Table 2.2 Quantum number of the relevant sub-levels of the states $^1S_0$ and $^3P_1$ and their values of the g_F factor. The consequent Zeeman shift is reported for each sub-levels in units of magnetic field evaluated in Tesla.

Experimental results

In the IT-Yb1 experimental system, the 556 nm green laser beam is generated on a different table, tuned with a double-pass AOM and cut with a mechanical shutter

before being sent to the physical package with a polarization maintenance fiber. Then, its polarization is cleaned using a PBS cube and is oriented perpendicular to the magnetic field used to split the Zeeman structure in order to excite only the σ transitions. The magnetic field is generated by a pair of coils in Helmoltz configuration, with radius r=4 cm, placed 17 cm apart and with 100 wire windings. The maximum coil current is about 2 A and they can generate a magnetic field up to $\sim$500 µT.

As shown in figure 2.5, the typical spin polarization process is composed of two steps: the first 15 ms are dedicated to stabilizing the constant magnetic field up to 350 µT (necessary to separate the Zeeman sublevels), waiting for the decay of any Eddy currents, and opening the shutter. Then the spin polarization laser pulse ($\simeq$0.5 µW) is shined on the atoms for 2 ms. The efficiency of the spin polarization is monitored by applying a green pulse and then coherently probing both π transitions of the clock line ($|^1S_0, m_F = \pm 1/2\rangle \rightarrow |^3P_0, m_F = \pm 1/2\rangle$), thereby measuring the excited fraction after the polarization process. When the atoms are efficiently pumped into the desired hyperfine state, the maximum of the Rabi line approaches 1 while the other is suppressed. Figure 2.10 illustrates the spin polarization efficiency as a function of the detuning of the spin polarization beam. Considering the $^3P_1$ Zeeman levels arrangement (see fig.2.9), moving toward higher detuning the peaks observed in Figure 2.10 are consequence of the σ transitions ($m_F = -1/2 \rightarrow m_F = -3/2$), ($m_F = 1/2 \rightarrow m_F = -1/2$), ($m_F = -1/2 \rightarrow m_F = 1/2$) and ($m_F = 1/2 \rightarrow m_F = 3/2$) respectively. For the state preparation procedure, only the central σ transitions (involving only $m_F = \pm 1/2$ states) are used because the other two transitions induce an atom loss from the trap and would not produce an efficient optical pumping process. Observing the number of trapped atoms, it is possible to notice an atoms drop even in correspondence of the spin polarization peaks. Part of this phenomenon is probably attributed to a residual excitation probability of the π transitions, approximately at the same frequency as the central sigma transitions. The origin can be derived by a component of the light polarization parallel to the magnetic field, allowing the $\Delta m_F = 0$ transitions, due to misalignment of the beam. Laser beams are, in fact, intentionally tilted slightly from perpendicular incidence on the windows to avoid etalon effects, consequently introducing a minor non-perpendicular component of the beam polarization relative to the magnetic field. A second source of atom losses is the proximity of the σ transition involving the sublevels $m_F = \pm 3/2$ of the $^3P_1$ state. These transitions, indeed, represent a strong loss channel for the atoms

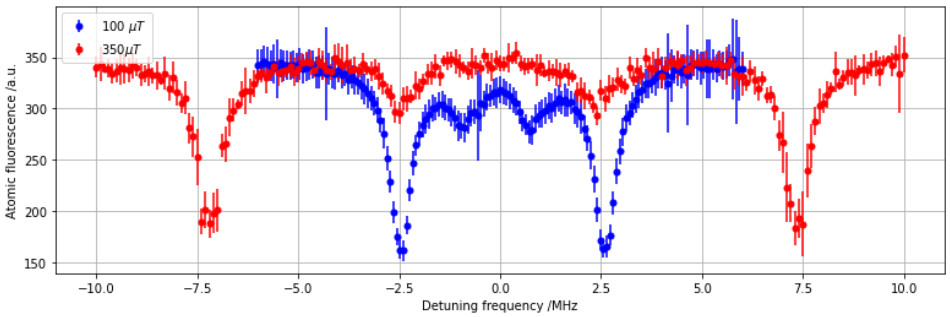


Fig. 2.11 Spectroscopy of the intercombination transition observing the number of atoms trapped as a function of the spin polarization beam frequency. With the new coils, a magnetic field of 100 μT and 350 μT has been respectively applied in the blue and the red spectrum, evidencing that increasing the Zeeman split of the σ transition involving $3/2$ levels reduce the atom losses during process.

and necessitating the generation of a sufficiently strong quantization magnetic field to adequately separate these sigma transitions from the two utilized for the spin polarization process. For this reason, during my Ph.D. we designed and constructed a new pair of custom-made coils capable of generating a more intense magnetic field. Figure 2.11 shows Zeeman spectroscopy of the intercombination σ transitions at varying magnetic field intensities. In order to reduce the atom losses the bias magnetic field has been set at the typical value of 350 μT. Other sources of atom losses during this process have been investigated without detecting relevant results, such as the dependence on the lattice depth. On the other hand, what strongly affects the atom numbers is the duration and the power of the green pulse, requiring to set them at the minimum value providing the desired spin polarization efficiency limiting the losses. Experimental parameters have been set to obtain a fraction of atoms prepared in the desired spin state larger than 95%.

2.4.2 Sideband Cooling

Atoms trapped in an optical lattice populate the lattice vibrational levels with a probability depending on the temperature. Each level defines a longitudinal vibrational state and is separated in energy by $h\nu_Z$, a quantum of motional energy.
The temperature of the atomic ensemble can be precisely determined through sideband spectroscopy of the clock transition (see figure 2.13a). Stimulating the clock transition with high laser power (a few milliwatt), beyond the central carrier(that

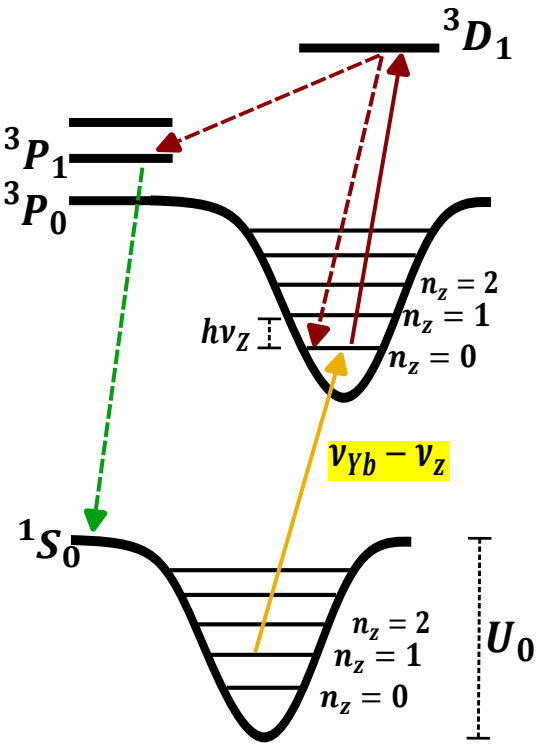


Fig. 2.12 Longitudinal sideband cooling scheme implemented on IT-Yb1. Atoms trapped in a potential hole with depth U_0 are excited along the clock transition with a red-detuning of ν_Z, reducing the vibrational state. After that, they are pumped on the short-life state $^3D_1$ from where they decay to the ground state. The process is repeated until all the atoms are in the fundamental vibrational state n_Z=0.

represents transitions conserving the same vibrational state $\Delta n_Z = 0$) two sidebands arise at higher and lower frequencies: they are defined as blue and red sidebands and they represent the transition respectively increasing or decreasing the vibrational state of one integer number ($\Delta n_z = \pm 1$). The temperature of the atomic ensemble can be decoupled into two components, a longitudinal T_z (parallel to the 1-D lattice axis) and a radial T_ρ (perpendicular to the confinement direction) [4], and as both strongly influence the sideband shape they can be extracted as fitting parameter [102].

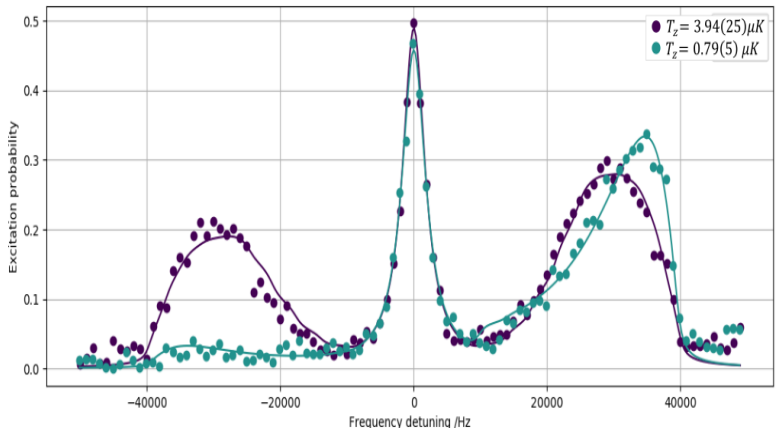
With the resoved sideband cooling technique [118] it is possible to move atoms populating the lowest trap levels reducing the temperature of the ensemble from the thermal equilibrium defined by the MOT: applying an opportunely red-detuned laser pulse, atoms can be excited along the red sideband ($\Delta n_z = n_Z^e - n_z^g = -1$) lowering the vibrational state during the transition and consequently reducing the energy of $h\nu_z$. Well-resolved sideband regime (transition linewidth $\Gamma_{clk} \ll \nu_Z$, in other words, sidebands well distinguished from the carrier) is required to efficiently excite the red sideband. In general, spontaneous decay preserves the same vibrational level and the optical pumping can be repeated until all atoms are at the fundamental vibration level n_z=0. The vibrational ground state is indeed transparent to the red-sideband transitions as a result of the absence of lower levels that can be addressed.
During my Ph.D. we implemented in IT-Yb1 a quenched sideband cooling scheme along the clock transition, as shown in figure 2.12. The red sideband of the clock transition is excited with $\sim$1.5 mW of yellow light appropriately detuned and with polarization aligned with the quantization magnetic field. To continue the process, the metastable $^3P_0$ metastable state is quenched by pumping the atoms into the short-lived $^3D_1$ state, from which the atoms decay spontaneously to the ground state passing through the $^3P_1$ level. The quenching is obtained by illuminating a few µW of 1389 nm lights on the atoms. Being a continuous sideband cooling scheme, during this totally incoherent process both the excitation and the quenching laser are applied simultaneously, providing a constant coupling between the metastable and the auxiliary states. As an alternative, we also tried a pulsed sideband cooling scheme: it is based on alternating in succession a cooling and a repumping pulse transferring atoms in the lower vibrational level with a coherent process with well controlled laser power and pulse time. However, this pulsed scheme yielded inferior results compared to the continuous method, likely due to the absence of phase correlation between the two lasers and the lack of active control over the power and

frequency of the 1389 nm laser. Theoretical descriptions and simulations of both schemes can be found in the literature [119, 120].

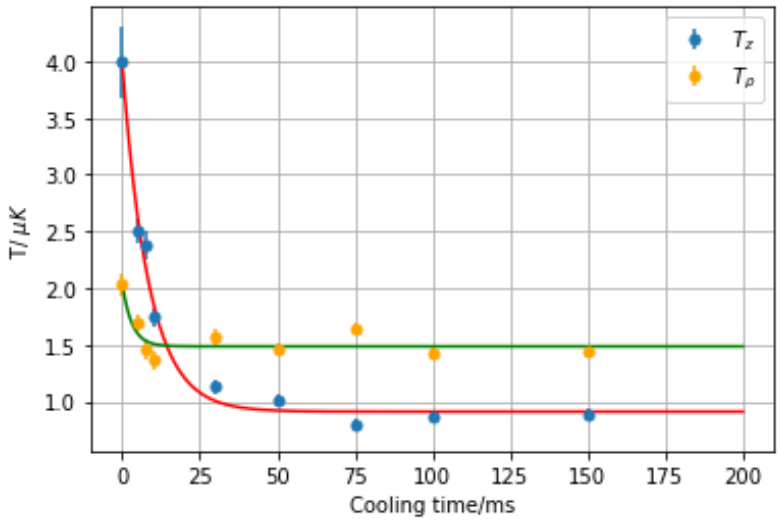
The effectiveness of this cooling technique can be assessed through sideband thermometry performed on the atomic ensemble, comparing results obtained with and without sideband cooling under identical trapping conditions, as shown in figure 2.13a.
The shape of the sidebands is determined by the $\Delta n_z = \pm 1$ transitions of all possible vibrational states, weighted by their population, which follows a generalized Boltzmann distribution[96]. Consequently, a reduction in the longitudinal temperature implies emptying the higher vibrational levels and driving more atoms to the fundamental $n_z = 0$ state. This suppression of population in higher-energy states and the absence of accessible lower states leads to the suppression of the red sideband and sharpening of the blue sideband. On the other hand, the radial temperature influences the sideband shape by distorting and broadening it.

Graph 2.13b demonstrates the exponential decay of temperature as a function of cooling time. These data were acquired under consistent trapping conditions, varying the duration of the cooling pulse while maintaining a fixed frequency detuning of approximately -30 kHz, corresponding to about 75% of ν_Z. A cooling pulse duration of approximately 50 ms is sufficient to bring the ensemble to a stationary condition with an average vibrational number $\langle n_z \rangle \approx 0.1$. At this point of work, we observed a temperature reduction from $\sim$4 µK to less than 1 µK. The minimum duration of the cooling pulse should be comparable with the atom radial oscillation time [66]. This cooling technique exhibits high efficiency along the tightly confined longitudinal direction, collinear with the cooling beam. Furthermore, even the radial temperature, T_ρ, is indirectly reduced, probably through collisional thermalization [4, 121].

Even though this is an incoherent pumping process, an efficient cooling requires high control of the laser beam parameters, in particular in terms of intensity and detuning of both the cooling and the quenching laser. Figure 2.14 reports the temperature measured at different lattice depths where the frequency of the cooling pulse $\nu_{cool} = \nu_{Yb} - \Delta\nu$ was varied with a red-detuning $\Delta\nu$ ranging from 0 (carrier) and ν_z.
The optimal frequency detuning for cooling exhibits a dependence on the lattice depth: for shallow confinement (blue and orange points) it is close to the trap



(a)



(b)

Fig. 2.13 (a) Sideband spectroscopy comparison with and without sideband cooling at D=100 E_R. Temperature, estimated from the sidebands fit, is reduced from ∼4 µK to less than 1 µK. Red sidebands (left) almost disappears while the blue one (right) is higher and sharper because of the higher number of atoms in the lowest trap levels. (b) Atomic temperature as a function of the cooling time measured at D=100 E_R with detuning $\Delta\nu$ =-30 kHz. T_ρ seems not being significantly influenced by the cooling. Solid lines are exponential fit of the temperature decay in time.

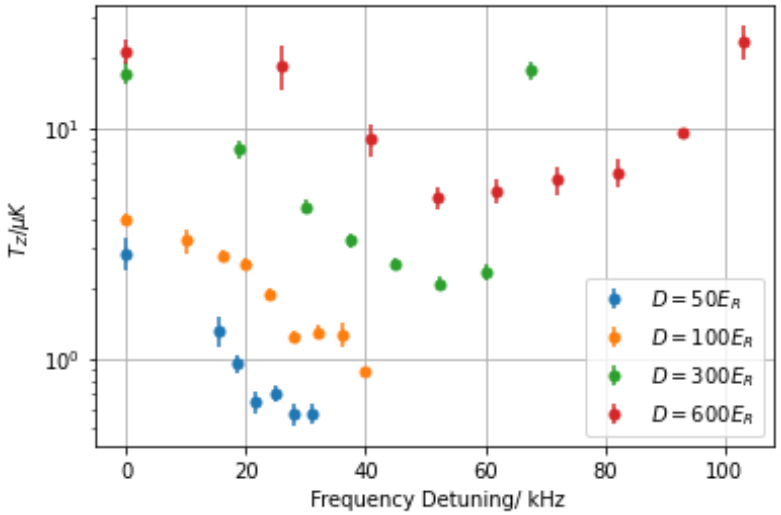


Fig. 2.14 T_z as a function of the negative detuning of the cooling laser (between 0 and ν_z) at different lattice depth. Quenching laser kept at fixed power and frequency. For shallow confinement the optimal red-detuning to cool atoms is $\Delta\nu \simeq \nu_z$, while for higher potential a lower detuning provides better results.

frequency ν_z while in case of a deeper lattice (red and green points) it has to be set to about 70% of ν_z, close to the edge of the red sideband. Atoms occupying higher vibrational states can only be excited with a smaller detuning and the radial motion further contributes to shifting and broadening the red sideband frequency. The repumping laser power requires careful frequency and power control in order to avoid the heating of the ensemble, which would heat and reduce the number of trapped atoms.

Implementing this technique in the typical clock cycle provide an higher control on the atoms and can lead to a reduction of systematic effects related to the atomic motion, such as the Doppler shift, cold collisions and lattice light shift [87, 90]. Currently, it has not yet been permanently implemented in the typical measurement scheme. We observed a reduction of the decoherence effects as a consequence of the reduction of the trapping inhomogeneity in cooled atoms: figure 2.15 shows the Rabi oscillation of the clock transition as a function of the time at fixed Rabi frequency. The blue dots have been acquired after sideband coolinghas been applied to reduce $T_z = 1\,\mu$K while the orange points have been obtained for thermally distributed atoms at $4\,\mu$K. Due to the higher uniformity of trapping conditions, the decoherence effects induced by atoms in different axial vibrational levels decrease [102]. This is evident when comparing the amplitudes of the Rabi oscillation fits across the two situations,

revealing significantly lower damping for atoms at 1 µK. As predicted by theory, the oscillation periods indicate that colder atoms exhibit a higher Rabi frequency, estimated from the fit as $4.17(5)$ Hz at 1 μK against $3.85(4)$ Hz at 4 µK. Considering an atom trapped in an optical potential with a vibrational state $|n_z, n_\rho\rangle$, its Rabi frequency Ω_{n_z,n_ρ} depends on the populated vibrational as follows [96]:

$$\Omega_{n_z,n_\rho} = \Omega_0 e^{-\eta_z^2} L_{n_z}(\eta_z^2) e^{-\eta_\rho^2} L_{n_\rho}(\eta_\rho^2) \tag{2.7}$$

where $\eta_{z,x}$ are the axial and radial Lamb-Dicke parameters and L_{n_z,n_ρ} are the Laguerre polynomials. As the atomic ensemble is composed by particles populating several vibrational states depending on the temperature, it is possible to define an average Rabi frequency:

$$\overline{\Omega} = \sum_{n_z,n_\rho} q(n_z, T_z) q(n_\rho, T_\rho) \Omega_{n_z,n_\rho} \tag{2.8}$$

with $q(n_i)$ normalized weights of the statistical thermal distribution. Assuming energy levels from an harmonic oscillator approximation (valid at low temperature) and a Boltzmann statistical distribution, these weights are described by:

$$q(n_i) = (1 - z_i) z_i^{n_i}, \quad z_i \equiv e^{-\frac{h\nu_i}{k_B T_i}} \tag{2.9}$$

The amount of inhomogeneity induced by atomic temperature can be estimated from the ratio between the root mean square spread of the Rabi frequency $\Delta\Omega$ and $\overline{\Omega}$ $\overline{\Omega}$. $\Delta\Omega$ id defined from:

$$\Delta\Omega^2 = \sum_{n_z,n_\rho} q(n_z, T_z) q(n_\rho, T_\rho) \Omega_{n_z,n_\rho}^2 - \overline{\Omega}^2 \tag{2.10}$$

Using 2.10, it is possible to evaluate the fractional inhomogeneity of Rabi frequency with and without the additional cooling scheme as $\Delta\Omega/\overline{\Omega}|_{T_z=1\mu K} = 0.023$ versus $\Delta\Omega/\overline{\Omega}|_{T_z=4\mu K} = 0.256$. This technique has the advantage of reducing the inhomogeneity of interrogation by an order of magnitude, bringing down the decoherence effects associated to the temperature. However, other relevant decoherence effects have not been investigated in this study, such as lattice beam misalignment,

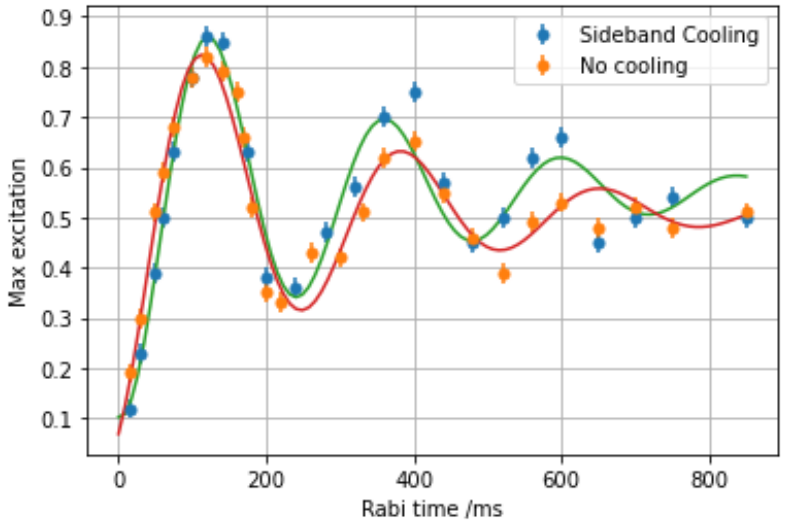


Fig. 2.15 Rabi flop the ytterbium clock transitions changing the interrogation time at fixed probe power. Blue (orange) dots have been acquired with (without) sideband cooling, at axial temperature T_z=1 µK(4 µK) and radial temperature T_ρ=1 µK (1.5 µK). The lower oscillation damping in the case of cool atoms suggests a reduction of the decoherence effects due to the trapping inhomogeneity. Fit of the Rabi flopping evidenced by the solid lines. Rabi frequency extracted by the fit as 4.17(5) Hz(3.85(4) Hz) for cooled (thermal) atoms.

radial motion of the atoms (poorly reduced by the sideband cooling technique) or the presence of undesired standing wave component in the probe beam [102].

Chapter 3

Metrological Results

During this chapter I will present the main metrological results obtained during my Ph.D. operating the ytterbium clock IT-Yb1. Most of these include frequency measurements and clock comparisons, which are essential for the validation of optical clocks and instrumental for the redefinition of the SI second [28]. In the first section, I will discuss the local absolute frequency measurement of the ytterbium clock transition performed at INRiM in 2022 and published in *Metrologia* [54]. Then, Section 3.2 is dedicated to the remote measurements performed during these three years of Ph.D. Specifically, Section 3.2.1 outlines the optical-microwave comparison against the French Caesium and Rubidium fountain through the European fiber link, a work published in *Physical Review Applied* in 2022 [55], while sections 3.2.2 and 3.2.3 respectively describe the international comparison campaigns involving optical clocks connected via fiber link performed in 2022 and 2023.Finally, the concluding sections will illustrate two instances of how optical clock research can extend beyond the laboratory to provide practical services. In 3.3 I will describe the IT-Yb1 contribution to the generation of the International Atomic Timescale (TAI) while the in conclusive section I report the description of the generation of a timescale steered using the INRiM ytterbium data, published on Optica [122].

3.1 Absolute Frequency Measurement IT-Yb1:IT-CsF2

Between June 2021 and September 2022, we operated the optical lattice clock IT-Yb1 to perform a local absolute frequency measurement of the ytterbium clock transition. This work has been published on *Metrologia* [54] in 2023.

To measure an absolute frequency, an optical atomic clock must be directly compared with the definition of the SI second. This is commonly achieved through TAI, which incorporates the average of several Cs fountains located worldwide, however at INRiM we had the possibility to do it locally due to the presence of a primary frequency standard. Consequently, we directly measured the frequency of the INRiM IT-Yb1 clock against the cryogenic Cs fountain IT-CsF2 [123]. This primary realization of the second is operative from 2013 and it regularly contributes to the TAI calibration with over 60 circular T contributions. Moreover, it also participates to the generation UTC(IT) [124], the Italian timescale. The total fractional uncertainty has been characterized at the level of 2.3×10^{-16} and its uncertainty budget is dominated by the characterization of the density shift and by the microwave imperfections. The local oscillator used for this measurement is a BVA quartz phase locked to an H-maser and upconverted to generate a 9.2 GHz microwave radiation. Then, it is tuned on the hyperfine atomic resonance mixing it with the signal from a direct digital synthesizer (DDS) whose frequency is corrected at every interrogation cycle. The typical short term stability lies between 2.3×10^{-13} and $2.8 \times 10^{-13} \sqrt{\tau/s}$ depending on the atomic density. The limiting factors are indeed the background noise from hot Cs atoms (reducing the signal to noise ratio) and the Dick effect from the local oscillator noise in the dead-time[123]. The local measurement has been carried out with an optical frequency comb placed at INRiM, whose uncertainty contribution is at the level of low 10^{-17}.

Measurement chain

The standard scheme for the absolute frequency measurement of IT-Yb1 with respect to the INRiM Cs fountain is represented in figure 3.1 by the blue branch. The Yb clock LO is the infrared 1156 nm laser locked to an ultra-stable cavity as described in section 2.2.3. A portion of the power is sent to an optical frequency comb (labeled as *comb2* in figure 3.1) by a fiber link with active cancellation of the link phase noise [79]. It is a crucial requirement to transfer the spectral purity to the comb enabling

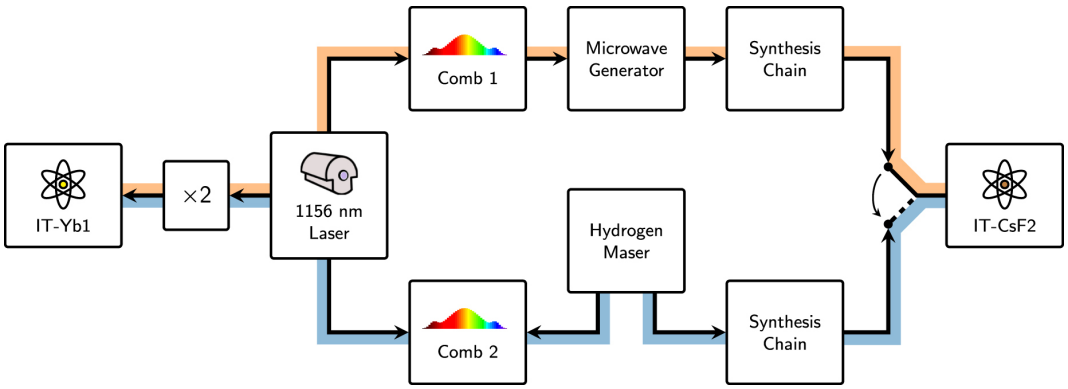


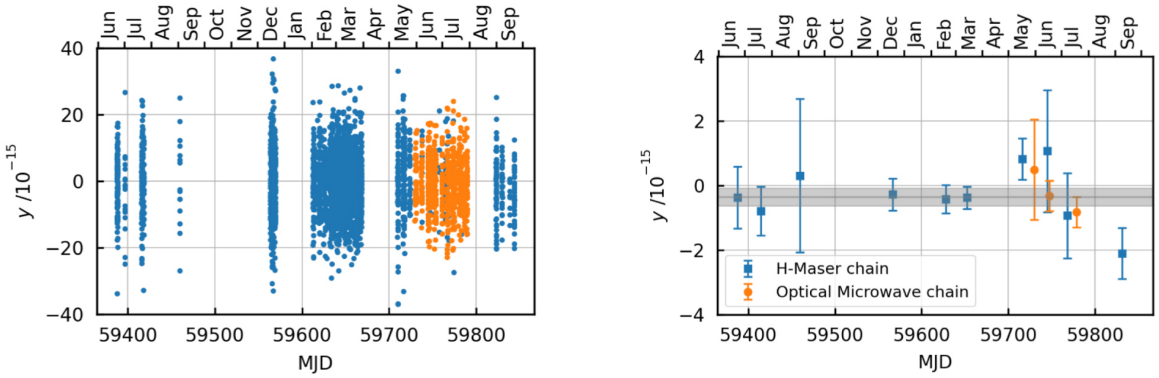
Fig. 3.1 Experimental setup adopted to compare the IT-Yb1 frequency against IT-FCs2 (extracted from [54]). Blue: path of the typical measurement scheme. From one side the H-maser provide a signal to the Cs fountain to generate the microwave through a synthesis chain, from the other it constitutes the reference for the comb used to measure the 1156 nm laser locked on the Yb atoms. The common reference allows a direct comparison between the two clocks. Orange: optical microwave chain. An additional frequency comb is locked on the ultrastable 1156 nm laser from which the Yb clock laser is generated. This one is used to generate a microwave employed as high stability local oscillator for the Cs fountain. The two microwave chains can be switched each other.

high precision measurements involving optical clocks. The comb used to count the frequency is referenced to the same H-maser used to generate the Cs fountain LO. By beating the two lasers with the comb and using the H-maser as transfer oscillator, the two local oscillators are directly compared to obtain the IT-Yb1/IT-CsF2 frequency ratio. The uncertainty contribution provided by the comb in the optical to microwave comparison has been estimated at the low 10^{-17} comparing two frequency combs counting the same frequency. This source of uncertainty is anyway one order of magnitude lower than the fountain accuracy, and so not dominant for this measurement.

Results

Data collection was carried out from June 2021 to September 2022, achieving a common uptime between the two clocks exceeding 32 days. Although both the ytterbium clock and the comb collect and register data every second, the Cs fountain requires a longer cycle. For this reason, data from IT-Yb1, comb and IT-CsF2 have been collected in bins averaging on 864 s to synchronously compare them. Data have been organized as fractional frequencies $y = r/r_0 - 1$, assuming r as the measured

frequency and r_0 the reference value. For this analysis we used as reference the recommended value by CCTF in 2021[26], r_0= 518 295 836 590 863.63 Hz with relative uncertainty of 1.6×10^{-16}. The use of a frequency ratio rather than a 16 or 17-digit number is a common convention in frequency metrology, convenient to reduce the computational effort [125]. Blue dots in Figure 3.2(a) report the data of the measured fractional frequencies averaged on 864 s bins of simultaneous clock operation. On the other hand, figure 3.2(b) records the same data averaged each month showing in gray the weighted average of the measurements.



(a) (b)

Fig. 3.2 (a) Experimental data of fractional frequency ratio IT-Yb1/IT-CsF2 in function of the time expressed in Modified Julian Date (MJD). Every point represents the average on 864 s of simultaneous operation. (b) The same data have been arranged showing the monthly average. The grey shaded line represents the weighted mean evaluated on the whole campaign. Blue data are referred to the traditional microwave chain while orange to the optically generated microwave.

The result of the measurement has been reported in the average fractional frequency ratio between IT-Yb1 and IT-CsF2 is:

$$f(\text{IT-Yb1/IT-CsF2, H-maser chain}) = -3.8(2.9) \times 10^{-16}$$

Corresponding to a absolute frequency of:

$$f(\text{IT-Yb1, H-maser chain}) = 518\ 295\ 836\ 590\ 863.43(15)\ \text{Hz}$$

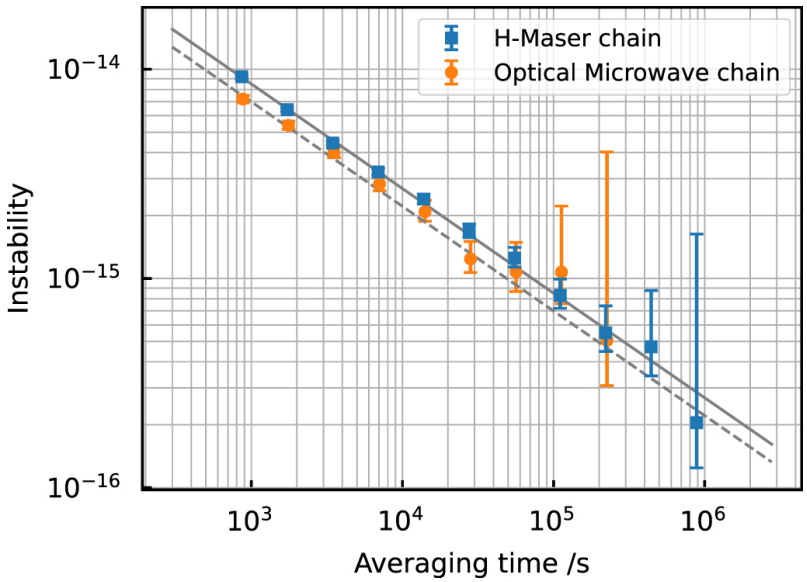


Fig. 3.3 Instability of the measurement campaign in term of overlapping Allan deviation distinguish the two ways to generate the Cs fountain local oscillator. H-maser chain: $2.7 \times 10^{-13} 1/\sqrt{\tau/s}$. Optical-to-microwave chain: $2.1 \times 10^{-13} 1/\sqrt{\tau/s}$

Graph. 3.3 shows the instability of the clock comparison in terms of overlapping Allan deviation. The short term stability is $2.7 \times 10^{-13} 1/\sqrt{\tau/s}$ at 1 s dominated by the Cs fountain, while the optical clock contribution is two order of magnitude lower (about $2 \times 10^{-15} 1/\sqrt{\tau/s}$ at 1 s) and it does not particularly affect the global instability. Knowing this value and the measurement time, one can estimate the statistical uncertainty affecting this measurement at the level of 1.6×10^{-16}, so below the systematic one.

3.1.1 Optically generated microwave

To enhance the stability of the Cs fountain local oscillator, during May, June and July 2022 we implemented an alternative chain to generate an ultrastable microwave starting from the Yb 1156 nm laser [126, 127]. The scheme, illustrated with the orange path in Figure 3.1, will be called *Optically generated microwave* in this work to distinguish it from the typically employed *H-maser chain*.
An additional frequency comb (*comb1* in the diagram) is referenced on the ultrastable laser through a phase-lock (bandwidth $\approx$ 300 kHz) instead of the H-maser. The spectral purity of the clock laser locked on the ultrastable cavity is thus transferred to the comb. The comb radiation is then collected by a fast photodiode, filtering

and amplifying the 40th harmonic of the 250 MHz repetition rate to obtain a 10 GHz oscillator. An additional synthesis chain reduces the microwave frequency to about 9.2 GHz and keeps it resonant to the Cs clock transition, thereby providing an ultrastable local oscillator.
The Flicker noise from the microwave generator and the synthesis chain represents the primary noise source that limits the stability of the optically generated microwave and has been estimated at 5×10^{-16}. The two microwave supply chains can be easily swapped, alternating measurements with the two methods.

The measurement with this *optical microwave* has been carried out for the equivalent of 6.9 days of both clock common operation with a stability of $2.1 \times 10^{-13}\sqrt{\tau/s}$ at 1 s, as reported in Figure 3.3. This result is worse than expected from a Dick effect contribution from the optically generated oscillator at level of of $3 \times 10^{-15}\sqrt{\tau/s}$: the main reason has been attributed to the Cs background gas that introduces a noise in the fountain interrogation, reducing the advantage of a better LO phase noise.

The result of measurement is reported in Figure 3.2 with orange dots and the measured ratio is:

$$y(\text{IT-Yb1/IT-CsF2,}\textit{Optical microwave}) = -3.2(3.7) \times 10^{-16}$$

Whose statistic contribution to the uncertainty has been estimated at 2.8×10^{-16}. From this ratio one can calculate the corresponding absolute frequency as follows:

$$f(\text{IT-Yb1,IT-CsF2,}\textit{Optical microwave}) = 518\ 295\ 836\ 590\ 863.46(19)\ \text{Hz}$$

Despite the better stability of the local oscillator, due to the shorter measurement time this result is affected by higher statistical uncertainty compared to the traditional one.

3.1.2 Total result

From the weighted average of the two results of frequency ratio reported in the previous sections, we estimated the ratio between IT-Yb1 and IT-CsF2 and the

corresponding absolute frequency of the ytterbium clock transition as:

$$y(\text{IT-Yb1/IT-CsF2}) = -3.6(2.7) \times 10^{-16}$$

$$f(\text{IT-Yb1}) = 518\ 295\ 836\ 590\ 863.44(14)\ \text{Hz}$$

The fractional uncertainty of 2.7×10^{-16} obtained during this work is the lowest reached for a absolute frequency measurement of the ytterbium clock transition against a local Cs fountain. Averaging for more than one year reduced the statistic uncertainty below the systematic limit of the fountain of 2.3×10^{-16}, while the uncertainty of the Yb clock and the optical to microwave conversion at the comb are negligible.

3.2 International campaign

Comparing optical clocks is the only way validating the high level of accuracy of these instruments and detect eventual outliers. At the same time, their worldwide spread is driving increasing interest in experiment of fundamental physics, like general relativity [23, 24], dark matter detection [21, 22] or variation of fundamental constants [128]. To connect optical clocks without affecting the accuracy and the stability, several techniques have been developed surpassing the GNSS performances, adapt for microwave clocks but requiring long times and limited in fractional uncertainty at low 10^{-15}. Optical fiber link are currently the best solution to compare optical clock in terms of performances, with an uncertainty contribution at the level of 10^{-19} averaging for just one day, so exceeding by one order of magnitude the best optical clocks. The only limitation comes from the need to periodically amplify and restore the signal, which limits their application primarily to intracontinental distances, albeit still extending to thousands of kilometers. A valid alternative to substitute the GPS satellite for inter-continental clock comparison has been found in the VLBI technique [41]. Even this one present the advantage of being implemented with already working infrastructures. Next sections contain a description and some results of the international comparison campaigns carried out in the last three years involving IT-Yb1 using the European optical fiber link to connect the clock with the other European National Metrology Institutes (NMIs).

3.2.1 Remote clock comparison: INRiM SYRTE 2021

During December 2021 we operated the optical lattice clock IT-Yb1 placed at INRiM, in Turin, to compare it against the microwave fountain FO2 by LNE-SYRTE, in Paris. This measurement at more than one thousand kilometers of distance was enabled by the 1023 km long optical fiber link between Turin and Paris, connecting INRiM to the main European NMIs. Additional information and an exhaustive description of the fiber link have been published on *Physical Review Applied* in 2022 [55]. Moreover, this experiment involved the INRiM Cs fountain IT-CsF2, which operated for 4 consecutive months from November 2021 to February 2022 with accuracy characterized at 2.4×10^{-16} and stability $3.2 \times 10^{-13}\ 1/\sqrt{\tau/s}$.

LNE-SYRTE FO2

SYRTE FO2 is a dual-species atomic fountain developed by the French metrology institute [129]. It can operate with both Caesium and Rubidium atoms in succession, constituting two independent frequency standards [130]: a primary one based on ^{133}Cs atoms (F02-Cs) and a secondary realization of the second interrogating the hyperfine transition of ^{87}Rb (Fo2-Rb). The systematic uncertainty limits the accuracy of the fountain at the typical level of 2-3 $\times 10^{-16}$[55] and the dominant factor is the density shift evaluation. The microwave oscillator used to interrogate the clock transition of both atomic species is generated by a cryogenic sapphire oscillator phase-locked to an hydrogen maser. This local oscillator guarantees a typical clock instability of $2.9 \times 10^{-14}\ 1/\sqrt{\tau/s}$ for FO2-Rb and $3.2 \times 10^{-14}\ 1/\sqrt{\tau/s}$ for F02-Cs (an order of magnitude better than IT-CsF2 stability). Furthermore, the experimental system has been designed to suppress the noise induced by the residual background gas by trapping atoms in a 2D MOT before moving them in the science chamber [129]. Due to this level of stability, it requires only 3-4 days of measurements to reduce the statistical uncertainty below the systematic one.

Optical fiber link

The infrastructure connecting the atomic clocks is a 1023 km cascaded fiber link with active stabilization of the optical length through the Doppler noise cancellation technique [131]. As shown in Figure 3.4, it connects Torino with Paris, traveling

on the already present telecom fibers passing through five intermediate stations. Additionally, this fiber link connects the Italian Quantum Backbone (IQB) [132], a national infrastructure to distribute frequency references to scientific institutes such as radio telescopes [41],[133], national space agency [132] or for quantum communication experiments [134] and high precision spectroscopy [135], with the French REFIMEVE[136][137]. From the French side, the link crosses the national borders extending toward UK and Germany and connecting the NPL and the PTB respectively. It makes possible an infrastructure putting in contact the main European NMIs.
A 1542.14 nm diode laser is frequency locked to an ultrastable cavity at SYRTE and its frequency is measured in real time with a frequency comb steered by an H-maser, thereby referring to the primary standard. The laser beam is sent through the international fiber link toward Torino, where its frequency is again measured against a frequency comb referenced to the local H-maser. makes this telecom laser a transfer oscillator: by measuring both clocks against the same reference, the clock at each side can be compared one against the other even if they are thousands of kilometers away. Intermediate stations are placed along the path to periodically regenerate the signal by phase-locking a laser diode to the incoming radiation or to redistribute toward other directions. Moreover, the signal has to be periodically amplified with 11 bidirectional Er-doped fibers to compensate for fiber attenuation. The link was tested over the period between October 27^{th}, 2021, and October 24^{th}, 2022, with overall uptime of the full chain of 57% (including also winter holidays in the calculation) and a peak of 72% in January 2022. Downtimes have been mainly caused by external interventions along the fiber path or temporary interruptions of certain element of the chain (e.g., comb unlocked or clock not operative).

Measurement chain

The measurement chain is schematized in Figure 3.5. From the Italian side the experimental system is the same of the *H-maser chain* explained in Section 3.1, with the LO of the fountain and the ytterbium clock, respectively, generated by a quartz referred to a local H-maser and by an infrared laser locked to an ultrastable laser, counted on a frequency comb. From the French side, the microwave radiation generated by a cryogenic oscillator, referenced to a local H-maser, steers the optical frequency comb reading the ultrastable 1542.14 nm telecom laser. By disseminating



Fig. 3.4 Scheme of the fiber link infrastructure connecting the main National Metrology institutes (extracted from [55], underlying the SYRTE-INRiM branch with thick line. The intermediate nodes are represented by the white dots. The red color represents the Italian portion (IQB) while the blue the French one (REFIMEVE). It is also possible to see the other branches of the link connecting Paris to the NPL (UK) and the PTB (Germany), as well as other European links not connected to the main infrastructure.

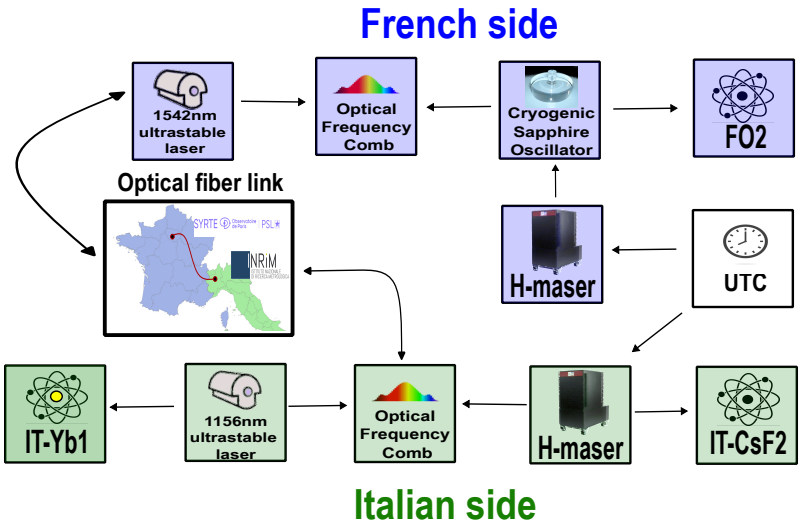


Fig. 3.5 Measurement scheme of the INRiM-SYRTE 2021 clock comparison. An optical frequency comb at LNE-SYRTE steered on the FO2 local oscillator measures the frequency of the a 1542 nm telecom laser locked to an ultrastable cavity. This one is distributed via fiber link to INRiM, where it is measured by the same local OFC responsible to measure the Yb clock local oscillator. This comb is steered on an H-maser referenced to UTC and employed to generate the IT-CsF2 local oscillator. All these nodes constitutes transfer oscillator that relate the frequency of the different clocks.

this signal toward INRiM and counting simultaneously on each side, the link acts as a transfer oscillator, allowing a contemporary comparison of the clock frequencies. In particular, the count on the INRiM side is an optical-to-optical conversion where the comb can be used in a single branch configuration achieving an uncertainty below 1×10^{-18}.

After the remotion of eventual outliers and data acquired in correspondence of cycle slips that affect the phase-lock of the link, the validated data are collected and averaged in 864 s bins to be compared with the other clocks involved [125].

Results

The optical clock IT-Yb1 was operated for this measurement campaign for 7 days, from December 15th to 21st, 2021, showing an instability of $2 \times 10^{-15} 1/\sqrt{\tau/s}$ and a fractional systematic uncertainty of 2.1×10^{-17}. In this work, we measured the ytterbium clock frequency by comparing it against two different microwave fountains to obtain two remote ratio (IT-Yb1/FO2-Cs and IT-Yb1/FO2-Rb) and a local (IT-

	y ($x10^{-16}$)	u ($x10^{-16}$)	u_A ($x10^{-16}$)	$u_{B,Yb}$ ($x10^{-16}$)	$u_{B,mw}$ ($x10^{-16}$)	Meas. time (h)
Remote comparison						
IT-Yb1/FO2-Cs	-0.4	3.0	2.1	0.2	2.1	95
IT-Yb1/FO2-Rb	-4.2	3.2	1.9	0.2	2.5	95
Local comparison						
IT-Yb1/IT-CsF2	-4.9	5.9	5.3	0.2	2.4	103

Table 3.1 Frequency ratio measured during the INRiM/SYRTE comparison campaign involving the IT-Yb1 [55]. **y** represents the fractional frequency deviation, **u** is the total uncertainty, $\mathbf{u}_A$ is the statistical uncertainty, dominated by the microwave standards stability, $\mathbf{u}_B$ is the systematic uncertainty distinguishing the Yb clock contribution from the fountain one. Last column shows the measurement time.

Yb1/IT-CsF2) one. The two measurements with cesium are absolute frequency measurements, whereas the one against rubidium is the first direct comparison between these two atomic species. As shown in Fig. 3.6, the instability of the microwave fountains predominantly limits the comparisons relative to the optical clock: the overlapped Allan variance has been measured as $4\times10^{-14}/\sqrt{\tau/s}$ for FO2 and $3.2\times10^{-13}/\sqrt{\tau/s}$ for IT-CsF2. The fractional frequency ratios are listed in Table 3.1, including the different sources of uncertainty associated to the measurement. The calculations have been carried out assuming as reference r_0 for the Yb and Rb clock transition frequencies the values established by CCTF in 2021 [26].

From the two measurements involving a primary frequency standard we can estimate the absolute frequency measurement of the Yb as:

$$f(\text{IT-Yb1/FO2-Cs}) = 518\,295\,836\,590\,863.61(17)\text{Hz}$$

$$f(\text{IT-Yb1/IT-CsF2}) = 518\,295\,836\,590\,863.38(31)\text{Hz}$$

while the remote measurement involving the two secondary frequency standards gives as result the Yb/Rb ratio:

$$f(\text{IT-Yb1})/f(\text{FO2-Rb}) = 75\,833.197\,545\,114\,168(24)$$

All these measurements are in good agreement with the recommended values for the secondary representations of the SI second and also with other previously

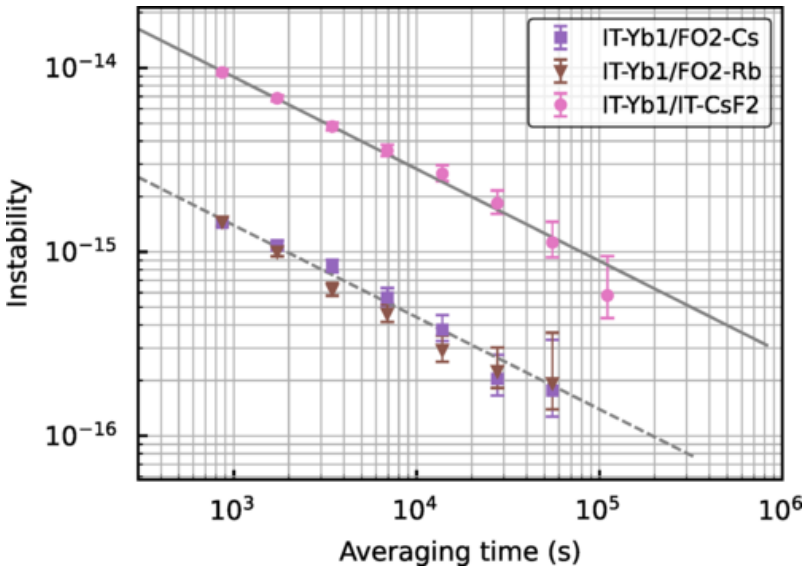


Fig. 3.6 Instability of the clock comparisons involving IT-Yb1 calculated as overlapping Allan deviation. The comparison with IT-CsF2 is limited by a white noise at th elevel of $3.2 \times 10^{-13}/\sqrt{\tau/s}$ while the one against FO2 shows a short term instability at $4.3 \times 10^{-14}/\sqrt{\tau/s}$ thank to the better local oscillator and a lower background gas noise.

measured Yb values and other Yb/Rb ratios [45][138].
It is noticeable that, despite the distance between the two clocks, the remote measurement exhibits a lower uncertainty compared to the local one. Due to the short duration of the campaign, the statistical uncertainty u_A dominates over the sistematic one. This makes the comparisons with the French fountain, characterized by a better stability, about 2.5 times more precise than the local one (see Table 3.1) despite the similar accuracy.
These results are a further proof that supports the potential of optical fiber links in remote comparisons of atomic clocks without affecting their accuracy and precision.

3.2.2 ROCIT 2022 Campaign

In the context of the EMPIR-funded ROCIT project [139], in March 2022 IT-Yb1 participated for the first time in a remote comparison campaign of optical clocks. The acronym ROCIT means Robust Optical Clock for International Timescales and its main project goal included to encourage European optical clocks to regularly contribute to the International Atomic Timescale (TAI) (1.3). To enable them for this operation it is not only important to make optical clocks robust and automatic instru-

ments, but also their incredible level of accuracy has to be validated by comparing different optical frequency standards against each other.
One of the key points of this project was the implementation of the largest international comparison campaign ever done, which involved 11 optical clocks from 7 different Countries connected via fiber link or GPS satellites. The following NMIs and universities, also shown in the map in Figure 3.7, participated to the comparison with their optical clocks: INRiM from Italy, PTB and LUH from Germany, LNE-SYRTE from France, NPL from UK, UMK from Poland, VTT from Finland, and, in conclusion, NMIJ from Japan. Table 3.2 summarizes all optical clocks whose data were considered in the ROCIT project reporting their uncertainty contributions and the comparison technique applied for this campaign.
Considering the efforts to keep in operation for a long time optical clocks and the complexity of the link system, to maximize the recorded data the measurement has been carried out for 1 entire month continuously operating clocks and links from MJD 59634 to MJD 59669. This period has been chosen because it overlaps the clock operation with the duration of the TAI Circular T 411 [32], which included the contribution of 3 optical clocks involved in this campaign (IT-Yb1, SYRTE-Sr2 and NMIJ-Yb1). The main results of this campaign are 38 validated clock frequency ratios determined concurrently: they constitute a significant addition in the determination of recommended frequencies of optical frequency standards and a notable progression towards the redefinition of the SI second.

Fiber and GNSS link

The measurement has been carried out by comparing the optical clocks placed in different countries connected via optical fiber and GNSS satellite link. The different kinds of connection are schematized in figure 3.7. The European phase-stabilized optical fiber link network [140] connects SYRTE with PTB and NPL and in 2021 it has been extended to enable INRiM to join the international optical-to-optical comparisons for the first time. It extends from the central node of Paris for thousands of kilometers periodically restoring the signal with bidirectional amplifiers. The uncertainty associated with this measurement technique has been estimated to be $<1 \times 10^{-18}$ after 1000 s of averaging, with a statistical uncertainty dominated by white frequency noise. Unfortunately, the portion between London and Paris was not operational in March 2022.

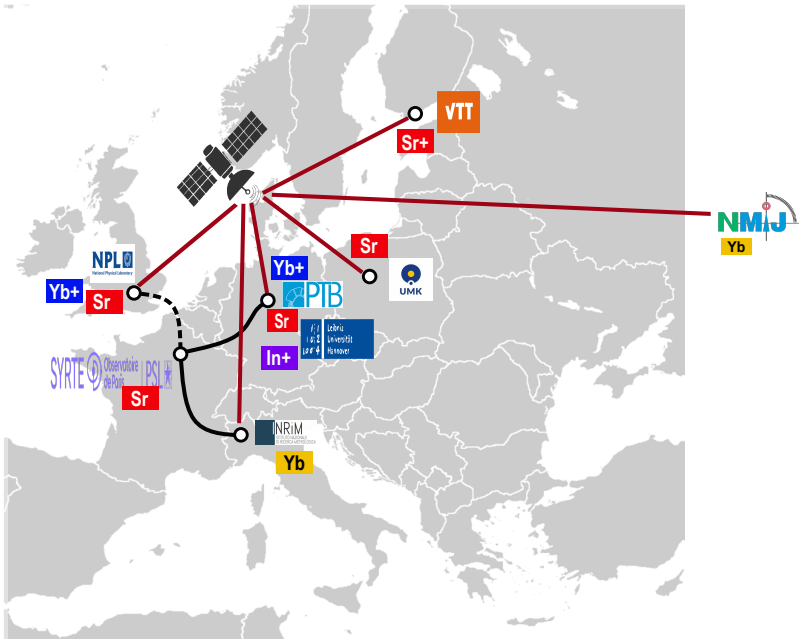


Fig. 3.7 Map of the institutes participating to the ROCIT 2022 clock comparisons campaign: INRiM(Italy), SYRTE (France), PTB and LUH (Germany), NPL (UK), UMK (Poland),VTT (Finland), NMIJ (Japan). The black curved lines represent the optical fibre link while the red straight lines the GNSS satellite connections. Atomic species employed are indicated close to each institute.

2022 Campaign

Institute	Clock	Link	u_B /10^{-18}	u_{RSS} /10^{-18}	u_{RF} /10^{-18}	u_{trans} /10^{-18}
INRIM	^{171}Yb	Fibre & GNSS	20	3.0	30	1.0
LNE-SYRTE	^{87}Sr	Fibre & GNSS	17	3.0	58	1.0
LUH	^{115}In^{+}	Fibre	2.5	2.4	-	1.0
NMIJ	^{171}Yb	GNSS	110	6.0	100	-
NPL	^{87}Sr	GNSS	22	2.7	49	-
NPL	^{171}Yb^{+}(E3)	GNSS	3.2	3.2	49	-
PTB	^{87}Sr	Fibre & GNSS	3.0	2.4	10	1.0
PTB	^{171}Yb^{+}(E2)	Local	33	-	-	-
PTB	^{171}Yb^{+}(E3)	Fibre & GNSS	2.7	2.4	10	1.0
VTT	^{88}Sr^{+}	GNSS	10	2.4	10	-

Table 3.2 List of optical clocks involved in the ROCIT 2022 measurement campaign. For each clock is reported the type of link used for the comparison, the fractional systematic uncertainty during the campaign (u_B), the uncertainty on the gravitational redshift characterization (u_{RSS}) and the uncertainty of the distribution mean, distinguishing between the one coming from the RF used for the GNSS comparison (u_{RF}) and the one provided by the transfer laser for fiber comparison (u_{trans}). The UMK Sr clock from Poland has not been included in this table because of problems in the clock operation.

To extend the campaign to other laboratories not connected by the fiber link, also a satellite link has been established with IPPP technique [38]. This technique, commonly employed for microwave comparisons, is also valid for optical clocks, but its performance is significantly worse than that of optical fibers in terms of both accuracy and stability. IPPP technique is in fact dominated by white phase noise and requires continuous phase measurement against hydrogen Masers to scale the link noise as $1/\tau$, but optical clocks typically present large data gaps due to the limited uptime. The measurement is thus dominated by the HM noise during the clock downtime. The typical frequency transfer instability is at the level of 1×10^{-15} after 1 day of measurement with overall uncertainty constrained to the low 10^{-16}[37, 36].

Results

Due to the considerable complexity of the measurement chain and the high number of elements involved, the results of this campaign have not yet been published and they are still under discussion. A paper is in preparation to describe in detail the campaign and the main results: in total, 38 validated optical frequency ratios between

different optical clocks have been obtained, 12 of which compared via fiber link with uncertainty at low 10^{-17} and 5 local comparisons with uncertainty at the 10^{-18} level. These include both same species comparisons (Sr, Yb and Yb^{+}(E3)) and ratios between different optical frequency standards. The first are particularly helpful in detecting eventual outliers or problem on a single clock, while the other not known a priori and so particularly interesting to be compared with their recommended values. This made it possible to reveal the presence of undetected uncertainty sources or criticalities in the uncertainty budget evaluation. In addition, the coordination effort necessary to organize the largest international optical clocks comparison campaign ever clears the road for future similar experiments.

Regarding IT-Yb1, we focused our efforts on constantly operating the clock throughout the entire period, achieving a total uptime over 45%. It was the first time this optical frequency standard was compared to other remote optical clocks via fiber link, an operation necessary in the process to validate the clock performances and to detect eventual errors in its accuracy evaluation. The IT-Yb1 uncertainty budget has not been assumed as constant but it had been evaluated in real time during each data acquisition, in particular concerning the characterization of the effects of density, DC Stark shift and lattice light shift. We obtained 4 validated optical frequency ratios through the fiber link, with Sr,Yb^{+} and In^{+} and other 4 through the GNSS technique. Among these, particular relevance is given to the first direct measurement of the ratios Yb/In^{+} and Yb/Yb^{+}. Unfortunately, a problem occurred in the GPS distribution apparatus at INRiM, forcing us to reject the satellite link measurements involving IT-Yb1. For this reason a direct comparison between the only two neutral ytterbium clocks present from INRiM and NMIJ has not been validated. Nevertheless, it may still be possible to estimate this value by bypassing the Italian GNSS infrastructure, utilizing the fiber link to other antennas as a transfer oscillator.

3.2.3 2023 International measurement campaign via fiber link

In 2023, another international measurement campaign took place in Europe from February 24th to April 30th (MJD 59999-60064). During 65 consecutive days of operations, 8 optical clocks have been operated simultaneously and compared exclusively by fiber link. Compared to the 2022 campaign, this one presented a longer duration and involved a new atomic species, the neutral ^{199}Hg measured by

2023 Campaign

Atom	Institute	INFO	u_B
Yb	INRiM	Lattice,Static	1.9×10^{-17}
Yb^+(E3)	PTB	Lattice,Static	2.7×10^{-18}
Sr	PTB	Lattice,Static	1.5×10^{-17} [142]
Sr	PTB	Lattice,Transportable	1.4×10^{-17} [142]
Yb^+(E3)	NPL	Ion,Static	3.2×10^{-18}
Sr	NPL	Lattice, Static	2.2×10^{-17}
Hg	SYRTE	Lattice,Static	4.8×10^{-17}
Sr	RIKEN	Lattice,Transportable	5.5×10^{-18} [3]

Table 3.3 Summary of the optical clocks involved in the 2023 international comparison campaign via fiber link. The fourth column reports the typical uncertainty, not the one used for this measurement.

the SYRTE Hg clock. Furthermore, two transportable Sr clocks, one from PTB and the other from RIKEN (Japan) participated to the measurement [141]. These were placed for the first month in London and then shipped to Braunschweig (Germany), headquarter of NPL and PTB, respectively. The list of clocks participating is represented in table 3.3.

During this measurement the link was operational for all the countries allowing a four-way campaign among INRiM, SYRTE, NPL and PTB. The clock redundancy was ensured by the presence of two Yb ion clocks and 3 neutral Sr clocks. Like the campaign of the previous year, the results are still under discussion and will be described in a paper in preparation. Not considering the transportable clocks, 15 optical frequency ratio at low 10^{-17} uncertainty level have been directly measured. Among the main results, the same species ratio between Yb^+ ion clocks of PTB and NPL has been remotely validated in agreement at $<5 \times 10^{-18}$ level and for the first time the LNE-SYRTE^{199}Hg clock has been compared at the level of 10^{-17}. These results are still under analysis and a paper is in preparation. Analogously to the ratios derived from the preceding campaign, these optical frequency comparisons campaign are crucial in the validation of the clocks uncertainty budget and to determine with higher accuracy the value of the optical frequency standards as recommended by the Roadmap for the redefinition of the second [28]. In particular, if the choice falls on Option 2 [30], the entire definition will be based on OFS comparisons, strongly motivating future experiments.

3.3 UTC contribution

As described in Section 1.3, the International Atomic Time (TAI) is the timescale generated by BIPM calibrating the Échelle Atomique Libre (EAL), monthly average of more than 400 atomic clocks worldwide, referenced to the SI second. The international Universal Coordinated Time (UTC) is then derived from TAI through the incorporation of an integer number of leap seconds. Both primary and secondary frequency standards (PSFS) can contribute to the timescale calibration. Although the process is straightforward for the Cs fountains, on which the definition of the second is based, the 10 optical transitions recommended by CCTF 2021 as a secondary representation of the second can be also used for the UTC steering passing through their recommended value [26]. This requires the introduction of an additional uncertainty u_{Srep}, corresponding to the uncertainty on the recommended value, to relate the secondary to the primary standard. The first secondary frequency standard contributing to UTC calibration was the Rb microwave fountain FO2-Rb from SYRTE (already described in Section 3.2.1) beginning in 2012 and in continuing in real time from 2013. Optical clocks started contributing sporadically from 2014 (SYRTE-Sr2) [143] and then from 2019 even in real time (SYRTE-SrB and NICT-Sr1). In recent years, 8 optical frequency standards contributed to UTC steering, showing high reliability in timekeeping operations, competitive with the fountains despite their lower uptime and the additional uncertainty. Figure 3.8 reports all the PSFS that provided their data to the BIPM to calibrate the timescales, highlighting primary and secondary frequency standards and distinguishing real-time or delayed calibrations with black or colored diamonds.

Data submission to BIPM

The Universal Coordinated Timescale is generated monthly by BIPM using data collected and submitted at the beginning of each month by several laboratories around the world.
Before a PSFS starts providing data for timescale calibration, it must go through an approval process from the CCTF Working Group on Primary and Secondary Frequency Standards (WGPSFS). It requires providing at least three months of calibration of an H-maser used as frequency reference for timekeeping, not necessarily continuous, and a cover letter including information about the frequency standard and

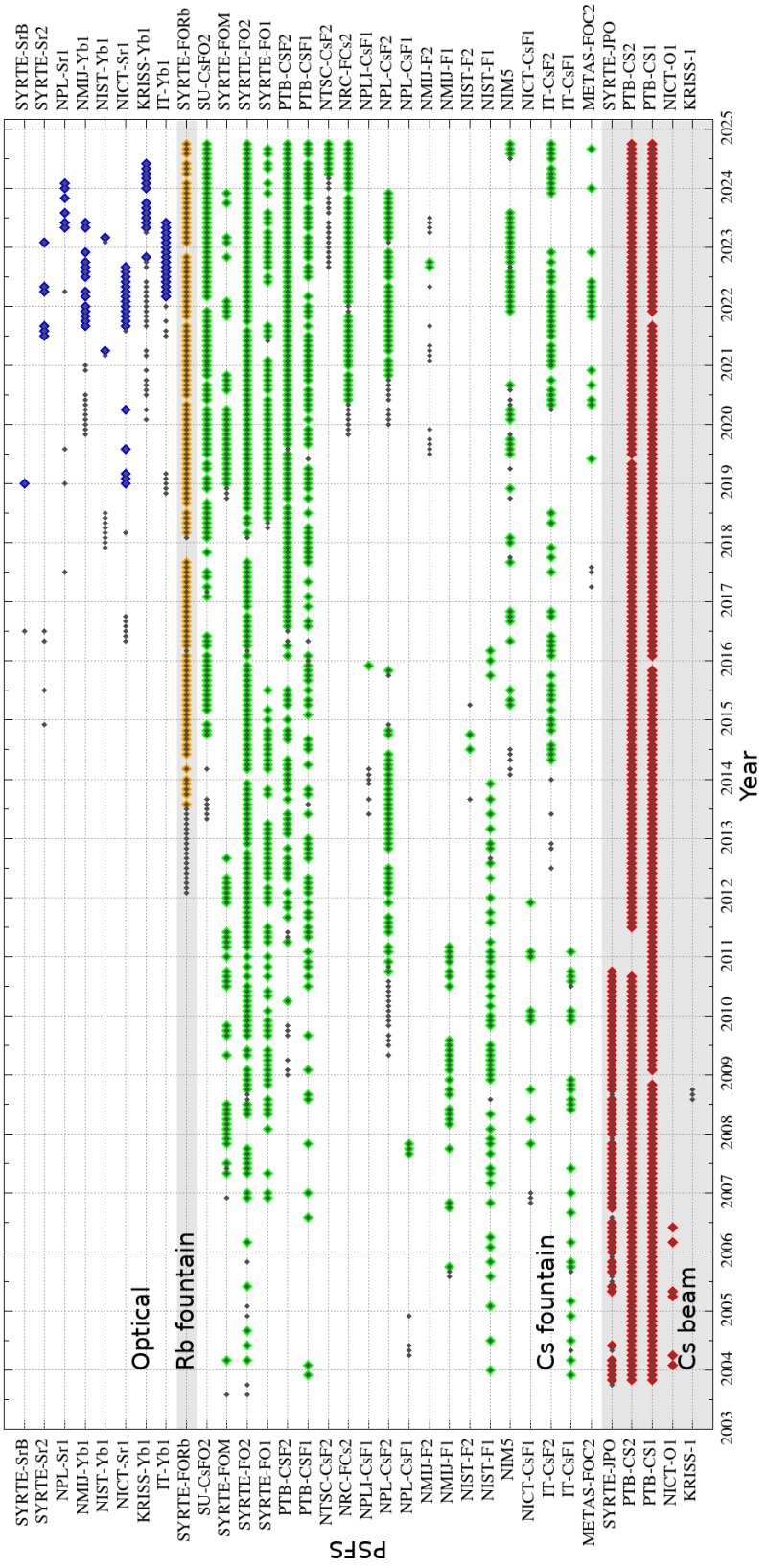


Fig. 3.8 Graphical representation of all the Primary and Secondary frequency standards submitting data to the BIPM from the Circular T 190. Highlighted points distinguish data submitted in real time within the month of UTC computation. IT-Yb1 contributed between 2021 and 2023 with 16 consecutive real time calibrations. Source https://webtai.bipm.org/ftp/pub/tai/other-products/taipsfs/psfs.png

its performances, such as frequency comparisons against other clocks. Moreover, the experimental system, the metrological chain and the uncertainty budget have to be presented in at least one peer-reviewed publication. If the atomic clock successfully passes this process, the provided data are employed for a delayed calibration, and it can contribute with future submissions.
Steering an H-maser means, in practice, measuring its frequency against a PSFS and correcting it to keep in agreement with the reference. H-masers are used as frequency reference for the timekeeping due to their long term reliability, low phase noise and good short term stability [144], but these instruments are not referred to the definition of the second and their frequency can drift in time. A continuous calibration is thus necessary to minimize the deviation from UTC of a timescale generated with these oscillators.

The clock data, i.e. the measurement of the maser frequency against a PSFS, are provided in form of report, whose structure is not fixed but has to contain some essential information. All the reports are available on the BIPM website. Data are packaged in 5 days samples starting from 00.00 UTC of the days ending with 4 or 9 if expressed in Modified Julian Date (MJD): the average frequency of the maser is calculated for each interval. The report must include the duration of the calibration interval of the reference maser indicated by its BIPM code [145, 146], the corresponding measurement uptime and (in case of optical clocks) the recommended value of the frequency used as secondary representation of the second with the associated uncertainty [26, 147]. In addition, the measured frequency has to be corrected keeping in account all the frequency shifts affecting the atomic clock used as reference, including the gravitational redshift. An example of this calibration is shown in figure 3.9. Other data required by the BIPM include the different sources of uncertainty, both statistical and systematic, concerning the PSFS and the dissemination chain.

Every month the BIPM updates UTC with the provided data and if they have been submitted within the 4th day of the month, they can be used for a real-time calibration, preferable because more effective. The considered interval can range between 25,30 or 35 days to overlap to the corresponding month. Moreover, BIPM also publishes *Circular T*, a monthly bulletin reporting the time offset of each local realization of UTC (the so-called UTC(k)) and including the information on all the

atomic clocks participating in the calibration. Additional information is available in reference [148].

IT-Yb1 Contribution

Data collected by IT-Yb1 have been regularly employed to measure the frequency of the INRiM H-Masers IT-HM3 and IT-HM4. The measurement chain is identical that described in the previous section, where the clock laser is frequency-stabilized to an ultrastable cavity and its frequency is measured by an optical frequency comb referenced to the H-maser under characterization. When the clock is operating, the laser frequency is actively controlled with an acousto-optic modulator to tune it on the atomic transition. By monitoring these laser frequency steering and the corresponding comb measurements, it is possible to measure the H-maser frequency (which drifts over time) with respect to the Yb atomic reference (stationary over time). As an example, Figure 3.9 displays the H-maser calibration, showing its fractional frequency deviation over time against IT-Yb1 during July 2022 (Circular T 415). Each blue dot represents the average of 864 s of clock measurement and because of the limited amount of data availability, the average maser frequency within each interval is derived through linear regression. Typically, the maser drift is on the order of 5-6 $\times 10^{-16}$/d.

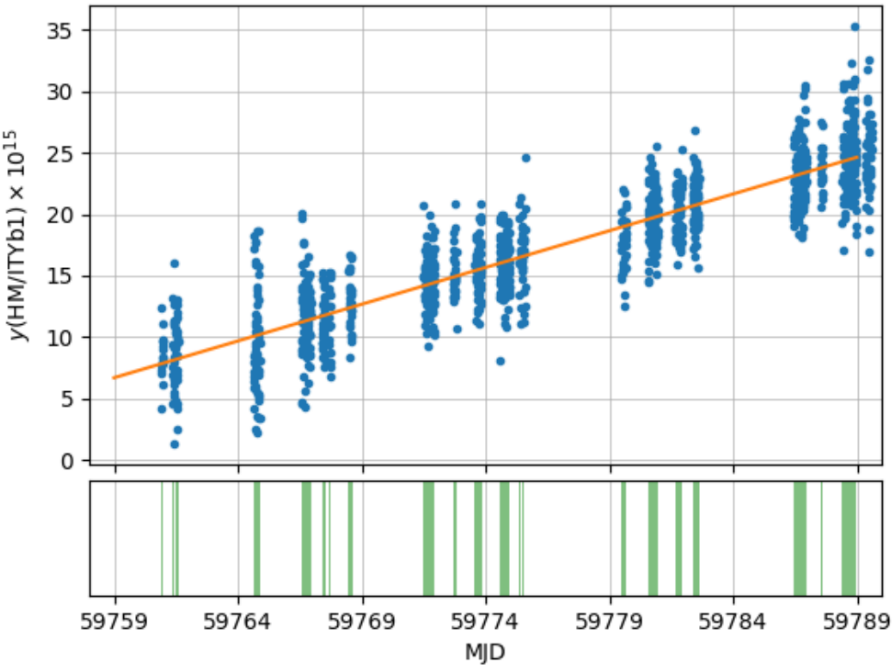


Fig. 3.9 Fractional frequency deviation y(HM1401104/ITYb1) measured between MJD 59759 and 59789. Blue dots represents the data averaged in 864 s groups. Orange line represents the maser drift, estimated at $6.0(1) \times 10^{-16}$/d from the linear regression. Green shaded regions in the bottom plot represent the uptime of IT-Yb1. Source: Circular T no.416 https://webtai.bipm.org/ftp/pub/tai/Circular-T/cirt/cirt.416

IT-Yb1 received approval from the CCTF (WPSFS) in 2019 making its first appearance in Circular T no.383. Figure 3.10 lists all the TAI contributions performed by IT-Yb1 during the last years, indicating the corresponding period in MJD. As with the initial submission in 2019, data collected in 2021 was submitted late in Circular T no. 410 (February 2022). However, from February 2022 up to May 2023, the monthly maser calibrations were regularly submitted on time, appearing continuously in 16 consecutive Circular T issues (from no. 410 to no. 425)

Various sources of uncertainty affect the measurement and are summarized in table 3.10: from the clock side u_A and u_B represent the statistical and systematic uncertainty,respectively, evaluated for the clock during the period of clock operation. The uncertainty in the link distribution is expressed by $u_{L/Lab}$ and $u_{L/TAI}$. The

```
# Estimate of d by individual PSFS measurements and corresponding uncertainties.
# All values are expressed in 10^-15 and are valid for the stated period of estimation.
# Values are reported as published in Circular T.
# 'YYMM' stands for the year 20YY and month MM of the corresponding Circular T period
# For Secondary Frequency Standard, 'Year(uS)' stands for the year of the recommendation of the updates to the list of the standard frequencies
#-------------------------------------------------------------------------------------------------------------------
# Standard   Period of     d     uA     uB  ul/Lab ul/Tai     u      uSrep  Ref(uB) uB(Ref)   Steer  Year(uS) YYMM  Uptime
# IT-Yb1     Estimation
#-------------------------------------------------------------------------------------------------------------------
 IT-Yb1     58389 58419   0.17   0.01   0.03  0.32   0.26    0.41    0.5       [2]    0.03     Y       2017   1911
 IT-Yb1     58419 58434   0.14   0.01   0.03  0.57   0.49    0.75    0.5       [2]    0.03     Y       2017   1911
 IT-Yb1     58459 58469  -0.10   0.01   0.03  0.59   0.70    0.92    0.5       [2]    0.03     Y       2017   1911
 IT-Yb1     58489 58514   0.65   0.01   0.03  0.39   0.31    0.50    0.5       [2]    0.03     Y       2017   1911
 IT-Yb1     58514 58539   0.75   0.01   0.03  0.26   0.31    0.40    0.5       [2]    0.03     Y       2017   1911
 IT-Yb1     59384 59389   0.82   0.01   0.03  0.37   0.98    1.05      0.5    T383    0.03     Y       2017   2202    13.7
 IT-Yb1     59394 59419   1.07   0.01   0.03  0.44   0.23    0.50      0.5    T383    0.03     Y       2017   2202     5.9
 IT-Yb1     59459 59464   2.00   0.02   0.04  0.65   0.98    1.18      0.5    T383    0.03     Y       2017   2202     2.4
 IT-Yb1     59564 59569  -0.19   0.00   0.02  0.08   0.98    0.99      0.5    T383    0.03     Y       2017   2202    75.7
 IT-Yb1     59619 59634  -0.38   0.00   0.04  0.20   0.37    0.42      0.5    T383    0.03     Y       2017   2202    22.2
 IT-Yb1     59634 59669  -0.51   0.00   0.02  0.08   0.17    0.19      0.5    T383    0.03     Y       2017   2203    45.8
 IT-Yb1     59669 59679  -0.24   0.00   0.02  0.13   0.53    0.54     0.19    T383    0.03     Y       2021   2204    45.6
 IT-Yb1     59709 59724   0.94   0.01   0.02  0.19   0.37    0.41     0.19    T383    0.03     Y       2021   2205    16.9
 IT-Yb1     59729 59734  -0.30   0.01   0.03  0.45   0.98    1.08     0.19    T383    0.03     Y       2021   2206    10.0
 IT-Yb1     59744 59759  -0.15   0.00   0.02  0.22   0.37    0.43     0.19    T383    0.03     Y       2021   2206    23.6
 IT-Yb1     59759 59789   0.04   0.00   0.02  0.14   0.20    0.24     0.19    T383    0.03     Y       2021   2207    16.7
 IT-Yb1     59789 59799  -0.11   0.01   0.02  0.27   0.53    0.59     0.19    T383    0.03     Y       2021   2208     7.8
 IT-Yb1     59829 59844   0.79   0.01   0.03  0.36   0.37    0.51     0.19    T383    0.03     Y       2021   2209     5.0
 IT-Yb1     59849 59879   0.16   0.00   0.03  0.21   0.20    0.29     0.19    T383    0.03     Y       2021   2210    12.1
 IT-Yb1     59879 59909   0.09   0.00   0.03  0.22   0.27    0.35     0.19    T383    0.03     Y       2021   2211     9.3
 IT-Yb1     59914 59939  -0.57   0.00   0.03  0.27   0.23    0.36     0.19    T383    0.03     Y       2021   2212    14.2
 IT-Yb1     59954 59974  -0.25   0.00   0.02  0.19   0.28    0.34     0.19    T383    0.03     Y       2021   2301    18.8
 IT-Yb1     59974 59999  -0.30   0.00   0.02  0.11   0.23    0.26     0.19    T383    0.03     Y       2021   2302    29.4
 IT-Yb1     59999 60034  -0.28   0.00   0.02  0.12   0.23    0.26     0.19    T383    0.03     Y       2021   2303    27.6
 IT-Yb1     60049 60064   0.13   0.00   0.02  0.24   0.37    0.44     0.19    T383    0.03     Y       2021   2304    15.6
 IT-Yb1     60064 60079  -0.02   0.00   0.02  0.17   0.50    0.53     0.19    T383    0.03     Y       2021   2305    30.5
```

Fig. 3.10 List of all the contributions to the BIPM Circular T from IT-Yb1. The one from the sixth line have been performed during my Ph.D. Every number is expressed in term of 10^{-15} Source: https://webtai.bipm.org/ftp/pub/tai/other-products/taipsfs/it_yb1-ftai

first arises from the link between IT-Yb1 and the H-maser, including the optical-to-microwave conversion, the statistics on the comb operation, the uncertainty from the maser-drift extrapolation and the effects of the downtimes. Its magnitude is typically in the low 10^{-16} and the dominant contribution comes from the dead times due to limited uptime. $u_{L/TAI}$ instead keeps in consideration the effects of the satellite comparison and is calculated by the BIPM. The global measurement uptime for each period is reported in the last column: it varies from few percent up to 75% with an average value weighted by every submission duration over 21%. It is important to note that u_{Srep} changed from 0.5 to 0.19×10^{-15} due to the update of the recommended value of the ytterbium clock frequency after CCTF 2021 [26].

We have proved the great reliability of IT-Yb1 for long-time operations. However, achieving this notable uptime currently necessitates considerable human effort. Despite lower data availability and less automation compared to a Cs fountain (which typically has >90% uptime), the lower systematic uncertainty and higher stability of the optical clocks make them competitive with primary frequency standards, even in TAI calibration. Unfortunately, other research activities or clock operations can compromise the availability of the data usable for maser calibration, currently limiting to 8 the number of optical clocks providing data to BIPM in the recent years [143].

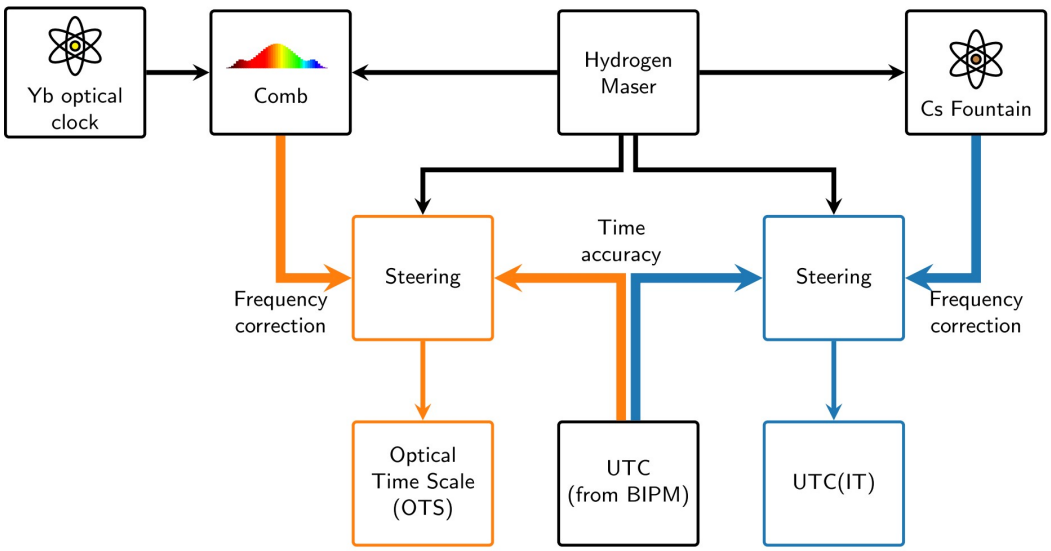


Fig. 3.11 Experimental setup scheme employed to generate the Italian timescale UTC(IT) (blue) and the Optical Timescale (OTS)(orange) [122]. Both use an H-maser used as master oscillator steering it respect to a reference: the local Cs fountain IT-CsF2 for UTC(IT) and IT-Yb1 for OTS. The time accuracy is ensured by the comparison with the global UTC .

3.4 Optical timescale

INRiM is responsible for generating UTC(IT), the Italian realization of the global UTC. It is typically generated by steering an H-maser with the Cs fountain IT-CsF2 and then monthly compared with UTC to correct any time offset. Thanks to the substantial amount of data collected during IT-Yb1 operations between February 2022 and April 2023, we collaborated with the INRiM time section to generate a local Optical Timescale steering an H-maser using the INRiM ytterbium clock as frequency reference. This timescale has not yet been employed to generate the official timescale UTC(IT), but this activity showed the possibility of implementing even optical clocks in typical local timekeeping. Despite the lower uptime and intermittent operation compared to the highly automated IT-CsF2, a few hours of measurement each day were enough to keep the UTC-OTS difference below 1 ns. An additional reason motivating this activity is the perspective of a future definition of the second based on optical clocks. In fact, among the necessary requirements [28] there is not only the contribution to the global UTC (discussed in the previous section) but also the regular participation in the generation of the local UTC(k) in the National Metrology Institutes.

In particular, we were able to generate a so-called "paper-OTS" by post-processing more than 1 year of data to test and calibrate the algorithm. Subsequently, a "physical OTS" was elaborated, processing data in real time for 5 months from December 2022 to April 2023. These timescales demonstrated a sub-nanosecond discrepancy from the global UTC for several months despite the limited mount of data availability. This work has been published on *Optica* in 2024 [122].

Experimental setup

The primary limitation in generating a purely optically based timescale is that optical clocks cannot ensure continuous operation over long periods. This problem can be bypassed by employing an H-maser as a flywheel oscillator and correcting its frequency by steering it to a stable atomic reference. The experimental setup used to generate the OTS is represented in figure 3.11 (orange arrows) compared with the one operating for the generation of UTC(IT) (blue arrows). The two measurement chains are conceptually equivalent. An H-Maser is measured against a PSFS to steer its frequency. If this is done against IT-CsF2, it is directly referenced to the definition of the second. Otherwise, if the comparison is done with respect to IT-Yb1 through the frequency comb, there is an additional conversion step. Time accuracy is provided to the timescales generated by the frequency-corrected H-maser by comparing them to UTC to remove any time offset..

HM4 is the code of the hydrogen maser employed during this activity (iMaser 3000 from T4Science [144]), which was at that time used to generate UTC(IT). ATo avoid compromising the generation of the Italian timescale, the signal emitted by the maser was separated into two independently steered branches: one to regularly maintain UTC(IT), and the other to generate the OTS. The typical linear drift of HM4 is at the level of 6×10^{-16}/day and along one year of operation only 3 anomalies occurred (sudden and unexpected changes in the maser frequency).

Paper OTS

IT-Yb1 operated regularly for over a year, from February 2022 to January 2023, measuring the frequency of HM4 for approximately 6 hours each day on average throughout this period. Data have been processed to provide the average frequency ratio IT-Yb1 / HM4 for each day of measurement. Knowing the systematic effects

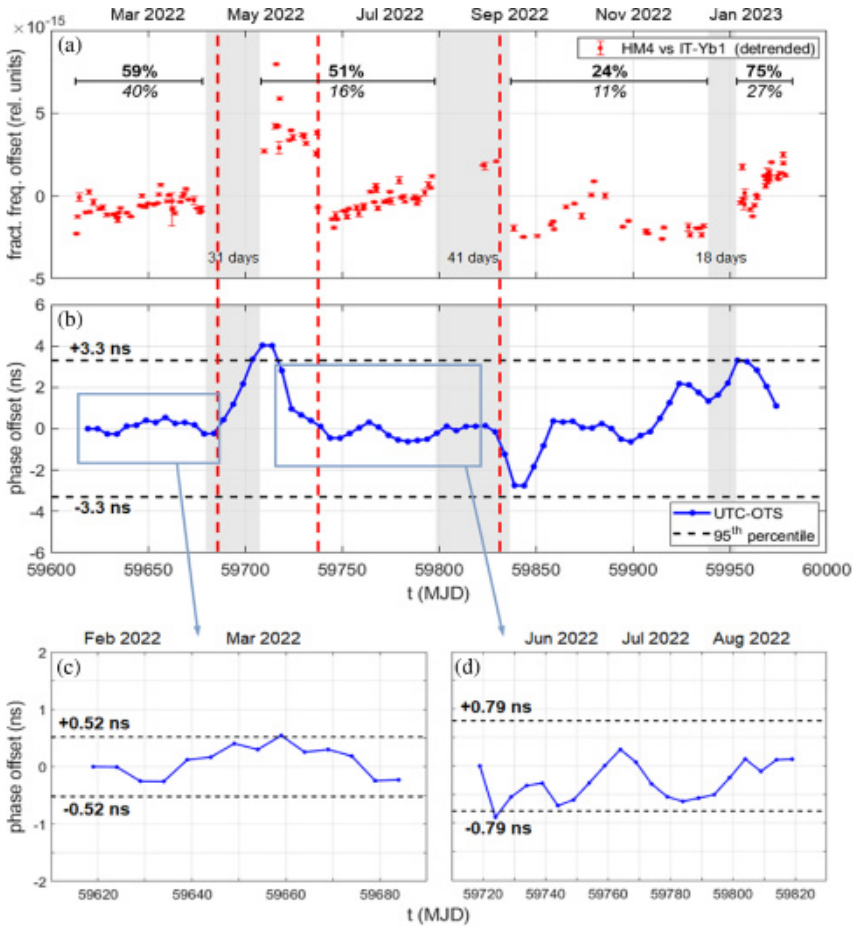


Fig. 3.12 **(a)** Daily average of the fractional frequency ratio between IT-Yb1 and the H-maser4 between February 2022 and January 2023. Dashed red lines evidence the presence of maser anomalies. Grey shaded regions represent periods without (or with few) available data, indicating their duration. **(b)** Phase offset of the paper OTS generated post-processing data in panel (a) from 9 February 2022 to 30 January 2023. **(c)(d)** Zoom-in on the paper OTS in panel (b) showing a sub-nanosecond phase offset from UTC for several months when clock data are regularly available.

and stability of all components in the chain, the uncertainty was assigned to each data point based on the daily measurement time.
The steering algorithm weights each data point according to its uncertainty to calculate the frequency correction applied to the H-maser, keeping the timescale in agreement with the references. This frequency correction serves two purposes: locking the maser frequency to the atomic frequency standard to remove drift and canceling out any time offset accumulated from UTC due to the use of a different frequency reference. These two actions provide frequency and time accuracy to the timescale, respectively.
This algorithm, originally developed for previous works [149, 124], has been adapted to accommodate the limited data availability of IT-Yb1. A detailed description of the algorithm is given in section 4 of *Formichella et al., Optica 11, 523-530 (2024)* [122] and in the supplementary materials [150].
Figure 3.12 illustrates the results from generating a year-long "paper OTS," which was calculated via post-processing using previously collected data. In the panel (a), each point represents the daily average of the HM4 relative to the IT-Yb1 reference, after removing a linear frequency drift of 6×10^{-16}/day. The red dashed lines indicate the occurrence of maser anomalies, while the gray-shaded regions denote periods with measurement gaps exceeding 14 days. The uptime is reported in two ways for each measurement period: the **bold** value represents the percentage of days with at least one valid measurement, whereas the *italic* value indicates the fraction of the total time the clock was operating within the considered period. Although, the latter is typical in timekeeping, the former holds greater significance for this experiment given that the steering correction is performed once daily. Considering the entire year, IT-Yb1 obtained a total up-time about 16%.
The second graph reports the time offset between UTC and the paper OTS calculated with the data in the top panel. The 95th percentile of the time displacement is within 3.3 ns and it is evidenced by the horizontal dashed lines. The main contribution to the displacement comes from the two maser anomalies occurred during the measurement gap of IT-Yb1 (corresponding to the first and third vertical lines). In this case HM4 frequency and drift change in unpredictable way, and if the clock data are not available, it cannot be corrected. Considering the first event, it occurred just at the beginning of the 31-day gap, accumulating so a consistent phase offset.
In contrast, the timescale is nearly insensitive to the second event (which occurred at MJD 59740) because the presence of clock measurements allowed for a timely

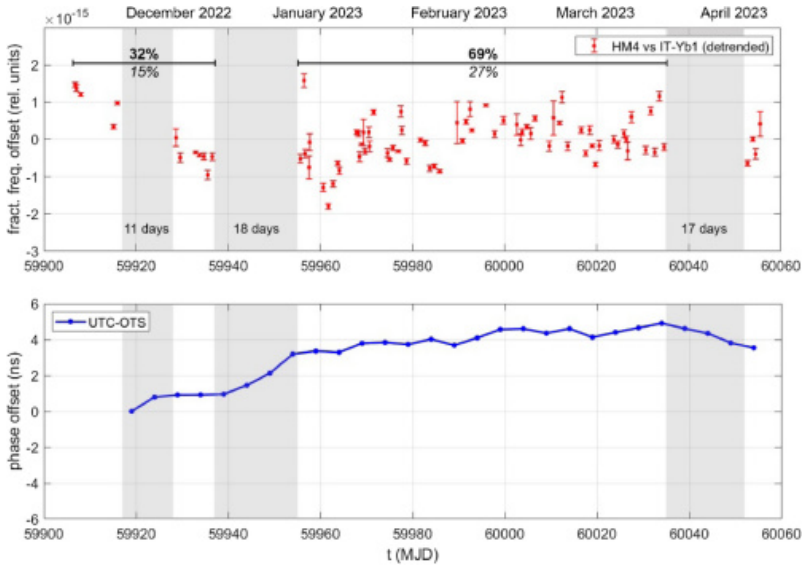


Fig. 3.13 Physical OTS. Upper panel: Daily average of the fractional frequency ratio between IT-Yb1 and the H-Maser4. Grey shaded regions distinguish periods over 10 days without data. Horizontal lines shows the two main measurements windows, indicating in bold the fraction of days with at least one available measurement and in italic the measurement uptime respect to the total time. Data submitted in real time from December 2022 to April 2023. Bottom panel: Phase offset between UTC and the physical OTS generated in the same time of the data collection. If the phase offset increases in absence of clock data, when IT-Yb1 is operating the timescale is not subject to significative drifts.

correction of the anomaly. Another significant displacement from UTC is observed after 59900 MJD due to the lower amount of data availability.
As expected, the best performances were achieved during the periods of higher optical clock uptime. As shown in panels (c) and (d), in these two regions with uptime over 50% the 95th percentile of the time offset was limited at 520 ps over 2 months and 790 ps over 100 days, respectively. Moreover, the last portion of figure 3.12(d) includes a 20-day period within an optical clock measurement gap. However, the maser's consistent behavior didn't introduce any additional phase offset, keeping the OTS offset at the sub-nanosecond level throughout this window.

Physical OTS

From December 2022 to April 2023, data collected by IT-Yb1 during the day were regularly processed and submitted the following morning.
This process enabled a real-time HM4 calibration, generating a "*physical timescale*"

that was continuously updated with new measurements day by day. In contrast to the *paper timescale* previously described, the steering algorithm employed for the real-time calibration does not present terms responsible for the time accuracy, since UTC is available only at the end of the month.For this reason, the physical OTS can only accumulate a time offset from UTC without active cancellation deriving from the comparison. At the same time, this highlights the actual performance of optical clocks used as timekeeping references.

Figure 3.13 illustrates the behavior of the Physical OTS during this period. The red points in the top graph represent the daily average measurement of the HM4 frequency after removing the linear frequency drift, estimated at 5×10^{-16}/day for the analyzed period.This experiment was affected by three major data gaps (highlighted in gray): the first, lasting 11 days, was due to an update of the experimental system, while the other two occurred during the Christmas and Easter holidays. Bold numbers indicate the percentage of days with available data, whereas italic numbers show the total uptime as a fraction of the time the clock was operational relative to the entire period. The lower panel reports the time offset of the OTS with respect to UTC. Over the 5 months considered, the physical OTS accumulated a maximum time offset below 5 ns,. The most significant contribution to this offset was derived by the 18-day data gap during the winter holidays, when HM4 exhibited an unpredicted frequency fluctuation that the steering algorithm could not correct. Limiting the analysis to the 3 month measurement window with 69% of IT-Yb1 uptime, the phase offset is below 2 ns.

3.4.1 Conclusions

This work demonstrates the feasibility of generating both paper and physical Optical Timescales (OTS) that achieve sub-nanosecond time accuracy over several months of operation. It also highlights the capability to maintain similar performance for an entire year using an optical frequency standard under realistic conditions. This OTS exhibits high reliability and robustness, despite occasional anomalies from the flywheel oscillator and limited uptime interspersed with periods lacking clock data. With respect to purely optical timescales based on ultrastable cavities as oscillators [151], which are valid as proof of principle but yet not relevant for metrological applications, the timescales based on optically referenced flywheel oscillators have already been generated in the last years at NIST [152], PTB [153] and NICT [154,

155], but never with this level of reliability for a long time. Other similar works have been published recently, for example, at NMIJ, where they performed maser steering based on the NMIJ-Yb1 clock [45] for 230 days [156]. Unlike that work, our study generated only a post-processed timescale, achieving similar results in terms of time accuracy (1.6 ns root-mean square of the phase offset to UTC) despite an extremely high uptime of the NMIJ clock, over 80%. This provides further evidence that, even if high uptime is desirable, a few hours of measurements regularly distributed in time are sufficient for good timescale performance, making the algorithm capable of compensating for any frequency irregularity.
At a local level, this experiment demonstrates the possibility of including IT-Yb1 in the list of references commonly used to calibrate the official Italian timescale, along with IT-CsF2 and UTC.

Chapter 4

Secondment at UvA - transfer cavity stabilization for an active clock

Between the second and third year of my Ph.D. I spent seven months in the Quantum gases group of the Institute of Physics of the Universiteit Van Amsterdam, supervised by professor Florian Schreck. Several cold atoms experiments are ongoing, [157], including continuous atom laser [158], quantum computation with Rydberg states in optical tweezers [159], Rubidium-Strontium molecules [160] and continuous superrdiance on thermal bemas [161]. They are also developing two strontium optical clocks: one passive, aiming to perform zero-deadtime continuous measurement and one active clock based on the phenomenon of superradiance [162, 163]. My secondment aimed to expand my experience with innovative and alternative techniques for building and operating an optical clock, specifically by assisting in the development of these two clocks. In particular, I built the experimental setup to generate a moving optical lattice at 813 nm used to control the atom-cavity interaction to achieve superradiance. I also designed and constructed a transfer cavity to frequency lock the lattice laser to a stable reference. This system will also be applied to the passive clock to generate the optical lattice for trapping cold atoms.

4.1 Active optical resonators

The progress in building ultra-stable cavities has led to clock lasers with linewidth lower than 100 mHz and frequency stability until $\sigma_y = 5.5 \times 10^{-17}$ at 1 s, but they

are anyway limited by the thermal noise of the optical cavities [164, 165].A potential solution to overcome this limitation is to generate an ultra-narrow laser by stimulating atoms to emit at the same high-Q transitions used in optical clocks. By inducing correlations among atoms, they can form a collective dipole, emitting radiation that follows the collective phase of the atoms. The coherence of the generated laser then relies on the atom coherence rather than the photons, thereby limiting the linewidth and stability based on the atomic properties. One of the most promising techniques for generating collective atomic emission is continuous superradiance, stimulated by atom-cavity interaction. In this phenomenon, N atoms trapped in a cavity align their electric dipoles, generating a collective and directional emission along a cavity mode whose power scales as N^2. scaling factor could also circumvent the problem that optical ultra-narrow transitions inherently have extremely small spontaneous decay emission power, making them difficult to measure and limiting the possibility of creating a so-called *optical maser*.

An essential requirement is to interrogate the atoms in the "*bad cavity regime*", where the cavity linewidth κ is significantly broader than the atomic transition linewidth Γ ($\kappa \gg \Gamma$). This regime effectively suppresses the dependency on external perturbations by introducing a cavity jitter suppression factor:

$$\alpha = \frac{2\Gamma}{2\Gamma + \kappa} \simeq \frac{2\Gamma}{\kappa} \tag{4.1}$$

Its value can be strongly smaller than the unit (even of the order of 10^{-3} or 10^{-5} for ultra-narrow transitions), making the frequency almost insensitive to the cavity perturbations on short timescales. Collective phenomena are possible in cavity if the number of photons interacting with a single cavity mode $NC_0\Gamma$ dominates the decoherence effects Γ_{dec} as:

$$NC_0\Gamma \gg \Gamma_{dec} \tag{4.2}$$

Among the main parameters concurring in Γ_{dec}, the most relevant are the spontaneous emission of the cavity mode Γ, the Doppler effect and the transit time of the atom through the cavity mode. The parameter C_0 is the single-atom cooperativity, defined as:

$$C_0 = \frac{4g_0^2}{\kappa\Gamma} = \mathscr{F}\frac{6\lambda^2}{\pi^3 w_0^2} \tag{4.3}$$

where g_0 is the single-atom coupling strength, $\mathscr{F}$ is the cavity Finesse, λ is the transition wavelength and w_0 is the waist of the cavity mode. This quantity depends on both the typical parameters of the atom and on the physical properties of the cavity. It may be interpreted as the ratio of the optical cross section of the emitted light to the cavity waist scaled by the finesse.

As the superradiant effect is achieved, the linewidth $\Delta\nu$ of the emitted light depends on both atomic and cavity parameters following:

$$\Delta\nu = \frac{C_0\Gamma}{\pi} \tag{4.4}$$

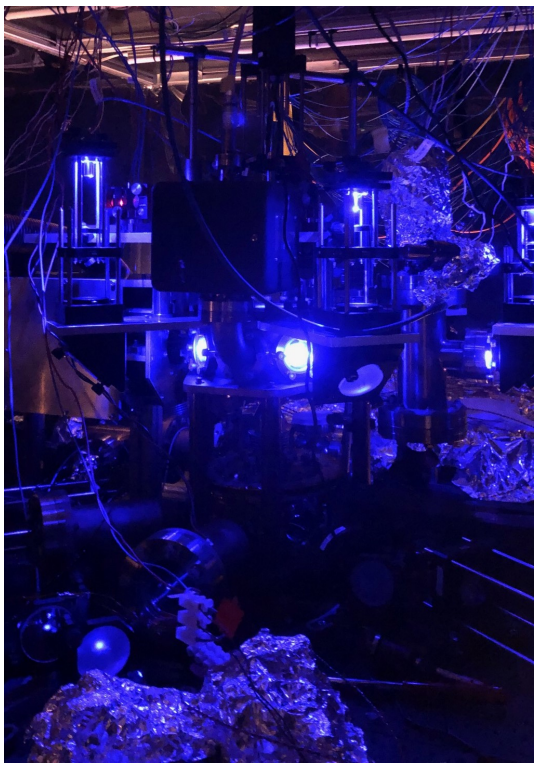
Pulsed superradiance has been experimentally obtained in several works[166], however, to make this type of active clock competitive in metrology, continuous emission is necessary. In this scenario, to sustain the collective effect over time, the number of atoms coupled with the cavity mode must be continuously maintained above a threshold by introducing new excited atoms that can replace those that have already interacted with the cavity. A straightforward expression to determine the minimum flux of atoms R_{th} to keep the system operating comes from [167]:

$$R_{th} = \frac{\pi^3 v^2}{3\lambda^2\Gamma\mathscr{F}} \tag{4.5}$$

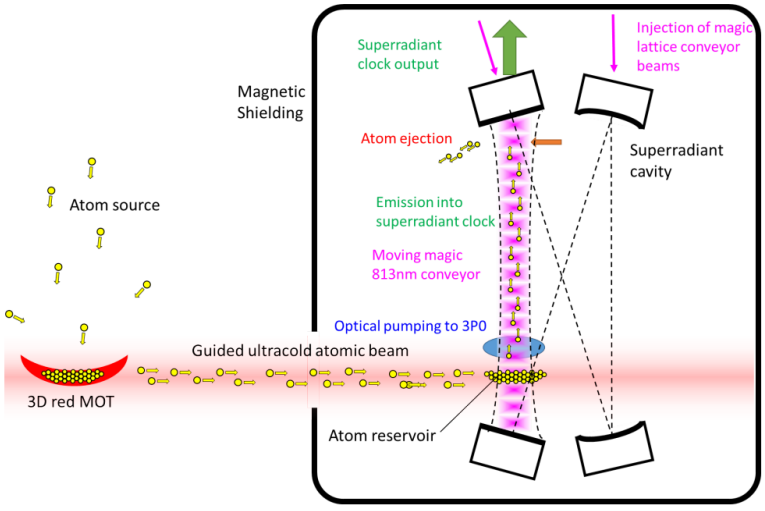
where v is the velocity of the atoms crossing the cavity. From this expression, increasing the finesse of the optical cavity makes it easier to achieve the superradiant threshold, thereby stimulating collective effects, but at the same time it increases the atom cavity cooperativity parameter (eq.4.3) and, consequently, the linewidth of the emitted light (eq.4.4).

4.2 Outlook - "mHz machine"

The so-called "*mHz machine*" (shown in picture 4.1a) is the experimental apparatus currently under development in the laboratories of the University of Amsterdam (UvA). Its primary objective is to generate continuous superradiance at the 698 nm



(a)



(b)

Fig. 4.1 (a) Picture of the experimental apparatus of the *mHz machine* with the blue 461 nm laser for the first stage cooling ON (b) Schematic diagram of the final stage of the UvA *mHz machine*. Atoms trapped in a steady-state 3D red MOT are transferred to the superradiant chamber and stored in a reservoir. A conveyor beam moves atoms along the cavity mode and after pumping in the clock excited state a superradiant emission is possible. A conveyor beam extract them from the reservoir moving them along the propagation of the cavity mode where they are pumped in the excited state enabling the superradiant emission. Credits iQClock deliverable 5.5 [168].

clock transition in Strontium atoms. Its name is derived from the natural linewidth of the doubly forbidden ${}^3P_0 \rightarrow {}^1S_0$ transition, which is at the level of few milliHertz. The main feature of this experiment is the bow-tie-shaped superradiance cavity, where cold atoms are trapped and transported along the cavity mode using a conveyor beam (see figure 4.1b) [168]. Unlike other approaches, where the atom-cavity interaction is stimulated with atoms crossing perpendicularly the cavity mode [169, 170, 161], this solution offers several advantages: it allows for a larger cavity waist, enabling the storage of a high number of atoms at low density, and provides a long interaction time controlled by the conveyor's speed. However, this approach also introduces some drawbacks, such as the requirement for a uniform and high-intensity magnetic field on a centimeter scale, a more complex cavity design, and a continuous source of excited cold atoms for storage in the cavity. The experimental setup for generating a continuous source of cold atoms is based on the continuous atom laser developed by the same group [171]. In this setup, a thermal atomic beam from the oven is collimated with a transverse cooling beam and then slowed using a Zeeman slower with permanent magnets. The atoms are then trapped in a continuous "*blue*" 2D-MOT at 461 nm (wavelenght of the ${}^1S_0 \rightarrow {}^3P_1$ electric dipole transition) in the horizontal plane. The atoms are so free to move along gravity falling down in a second science chamber after a further reduction of the horizontal velocity thanks to a 2D-"*red*" molasses operating at the 7.5 kHz wide intercombination transition at 689 nm: this reduces the divergence of the beam in the about 40 cm length of free-fall.
In the lower chamber, atoms are trapped in a continuous 3D 'red' magneto-optical trap , forming a permanent reservoir of cold atoms. The separation from the upper chamber is crucial for protecting the trapped atoms from the scattering with resonant blue photons, which would otherwise remove atoms from the MOT. Given that the superradiant cavity must be shielded from external magnetic fields, it has been constructed in a third chamber. Consequently, the atoms are delivered from the red MOT via a dipole guide. An high power laser a 1064 nm is used to extract cold atoms from the red-MOT and move them horizontally for 30 cm. They are then slowed by either a counter-propagating beam or a Sisyphus decelerator [172] and stored in a reservoir generated by a dipole trap inside the cavity. Here the atoms are excited on the metastable ${}^3P_0$ state by using a three photon STIRAP-like transfer [173]: this scheme has the advantage of not introducing photons at the clock wavelenght (698 nm) externally, ensuring that measured signal comes only from the collective effects. As previously described, an optical conveyor is

situated inside the cavity, transporting the excited atoms along the cavity mode. This conveyor comprises of a moving lattice at 813 nm, magic wavelenght of the strontium clock transition, generated by two slightly detuned, counter-propagating laser beams forming a Bloch accelerator [174]. ontrolling the conveyor's speed allows for managing the interaction time between atoms and the cavity, thereby facilitating the achievement of the superradiant threshold. Typical speed range are from 0.2 to 20 cm/s corresponding to a storage time from 10 s to 100 ms.
Furthermore, extended periods within the lattice offer the opportunity to create multiple pumping regions by repeatedly utilizing the same atoms. Ultimately, atoms must be ejected by a push beam to prevent their deposition on the high-reflectivity mirrors, which would reduce the cavity's finesse. The system is designed to work with both the ^{87}Sr and ^{88}Sr isotopes: the first, fermionic, is easier to manage because its natural hyperfine structure requiring a smaller magnetic field (about 2 G) to separate it. However, the bosonic isotope is preferable because of the higher natural abundance (making easier to achieve the superradiant threshold) and the linewidth of the clock transition in principle even smaller than 1 mHz. Concurrently, the clock transition requires the application of a constant magnetic field, whose magnitude has been estimated to be up to 200 G, depending on the speed of the moving lattice.

4.2.1 Current status

The system is currently not fully operational and remains partially under construction. When I left Amsterdam in December 2023, the physical package was nearing completion.Recently, the steady-state red MOT has been successfully achieved and optimized, and team members are now working on the atom transfer from toward the superradiance cavity. More information are available in the Sheng Zhou thesis [175].

4.3 Magic lattice generation

As previously described, the 'mHz machine' requires a conveyor to guide atoms within the optical cavity. This conveyor will be generated by overlapping two counter-propagating laser beams with a controlled detuning. At least 200 mW of 813 nm light have been estimated, with a linewidth lower than 1 MHz.
In this section, I will describe the experimental apparatus I designed and built to

generate and frequency-stabilize an 813 nm laser for this purpose. This system is fundamentally composed of an injection-locked laser diode whose master laser is stabilized on a transfer cavity, thereby transferring the long-term stability of an atomic reference. Furthermore, the same master laser I developed will also be used to stabilize another slave laser diode, which will generate the optical lattice for the 'passive' clock currently under development at the UvA laboratories

4.3.1 Injection locking of a 808nm laser diode

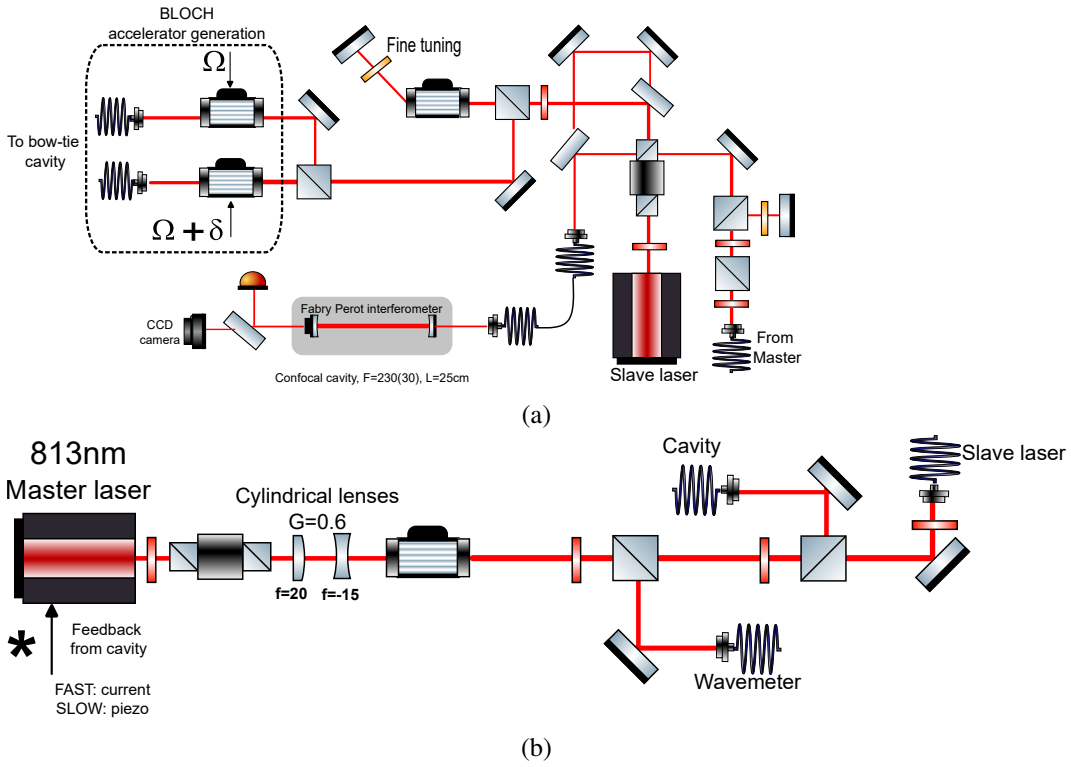


Fig. 4.2 Optical setup to generate the lattice laser at 813nm. (a) The slave laser is injected by using an isolator to frequency stabilize it. The emitted radiation is split on two branches whose frequency is finely tuned through two AOMs. (b) Master laser setup: the laser beam is spatially manipulated by a telescope and a small portion is provided to a wavemeter and a the transfer cavity. Passing through a fiber noise cancellation scheme the main portion of the power is transferred to the slave laser.

The laser source employed for this work is a single-mode laser diode manufactured by Toptica, with central emission at 808 nm. It generates up to 800 mW of laser power and can be tuned by temperature or injection current to move the wavelength

close to the magic value, 813 nm. At the desired wavelength the maximum power does not exceed 750 mW. The optical setup is shown in figure 4.2a: The slave laser is placed in a butterfly mounting to supply current and control temperature, and it is enclosed in a custom-built aluminum box to shield it from external perturbations and ensure thermal stability. A Faraday isolator is utilized to protect the diode from back-reflected light and to facilitate injection locking. After passing through the isolator, the laser beam is directed towards a double-pass AOM (Acousto-Optic Modulator) for fine frequency tuning. The light is then split and directed into two parallel branches, each containing an AOM for power control and frequency detuning of the respective beams. These two beams will subsequently be sent to the bow-tie cavity to generate the moving lattice, where controlling their detuning allows for precise management of the lattice speed. A small portion of the light is extracted using a beam-sampler and overlapped with a fraction of the seed light designated for injection locking. Both are coupled into the same optical fiber and transmitted to a custom-built Fabry-Perot Interferometer (FPI), which is used to monitor whether the slave laser is locked to the reference. The FPI is a confocal Fabry-Perot cavity 25 cm long with two spherical mirrors with radius of 25 cm and 99.0% of reflectivity. The measured Finesse is $F = 231(6)$, corresponding to a linewidth of $2.60(7)$ MHz. One mirror is fixed to the aluminum spacer, while the other is mounted on a piezo ring to actively change the cavity length, thereby scanning different resonant frequencies.

The master laser employed for injection locking is a Toptica DLpro Extended Cavity Laser Diode (ECDL), frequency-stabilized on a transfer cavity (described in Section 4.4). The optical scheme is described in Fig:4.2b: The highly elliptic and astigmatic beam is manipulated in the horizontal direction using a telescope composed of a pair of cylindrical lenses. After that the beam passes through a dual stage optical isolator attenuating eventual back-reflected beams of 60dB and two small portions are distributed toward a wavemeter to measure the frequency and to the transfer cavity used to lock the master laser. This laser emits up to 50 mW of power at 813 nm, but just 20 mW are enough to obtain an injection ratio of -15 dB at maximum power.

4.3.2 Optical Injection locking (OIL)

Optical Injection Locking (OIL) is a technique employed to synchronize the phase and frequency of two lasers through photon-photon interaction. A reference laser,

with frequency ω_{ML} (defined as "seed" or "master"), is injected into a 'slave' laser operating at its free-running frequency ω_{fr} forcing it to synchronize with a fixed phase offset and the same frequency.

A commonly used model for describing OIL originates from the semi-classical laser rate equations. These equations describe the time evolution of the number of atoms, the phase, and the number of emitters in the active material, incorporating additional terms that account for the number of injected photons and the phase of the master oscillator [176, 177]. If steady-state solutions exist, stable OIL occurs, where the slave laser frequency tracks that of the master laser. A necessary condition for this stability is that the frequency difference between the master and the free-running slave laser, $\Delta\omega = \omega_{ML} - \omega_{fr}$ must fall within the locking bandwidth $\Delta\omega_L$. Defining the stability conditions, the stable locking range is asymmetric with respect to the frequency detuning and is defined by [178]:

$$-\kappa\sqrt{1+\alpha^2}\sqrt{\frac{P_{inj}}{P_0}} = \Delta\omega_{min} < \Delta\omega_L < \Delta\omega_{max} = \kappa\sqrt{\frac{P_{inj}}{P_0}} \tag{4.6}$$

here κ is the coupling coefficient describing the rate at which the injected photons enter into the laser cavity. This can be approximated as half the lossless cavity bandwidth $\omega_{fr}/2Q_c$, with Q_c the quality factor. P_{inj}/P_0 is the injection ratio between the injected and the free-running power. The asymmetry arises from the presence of the amplitude enhancement factor α, which describes an amplitude phase coupling responsible for the red-shifting of the laser cavity mode [176]. In semiconductor laser α typically ranges between 0.1 and 10 [178]. As κ can be approximated as half the cold,lossless cavity bandwidth $\omega_{fr}/2Q_c$, laser with lower quality factor Q_c are easier to lock thank to a wide locking bandwidth. At the same time, a low Q_c increases the laser linewidth influencing the phase noise performances of the slave laser [177]. Under stable OIL the phase difference between master and slave laser stabilize at:

$$\Delta\phi = sin^{-1}\left\{\frac{\Delta\omega_{inj}}{\Delta\omega_L}\right\} - tan^{-1}(\alpha) \tag{4.7}$$

depending on the relative frequency detuning with respect to the bandwidth and ranging between $cot^{-1}(\alpha)$ and $-\pi/2$ at the positive edge of the locking range.

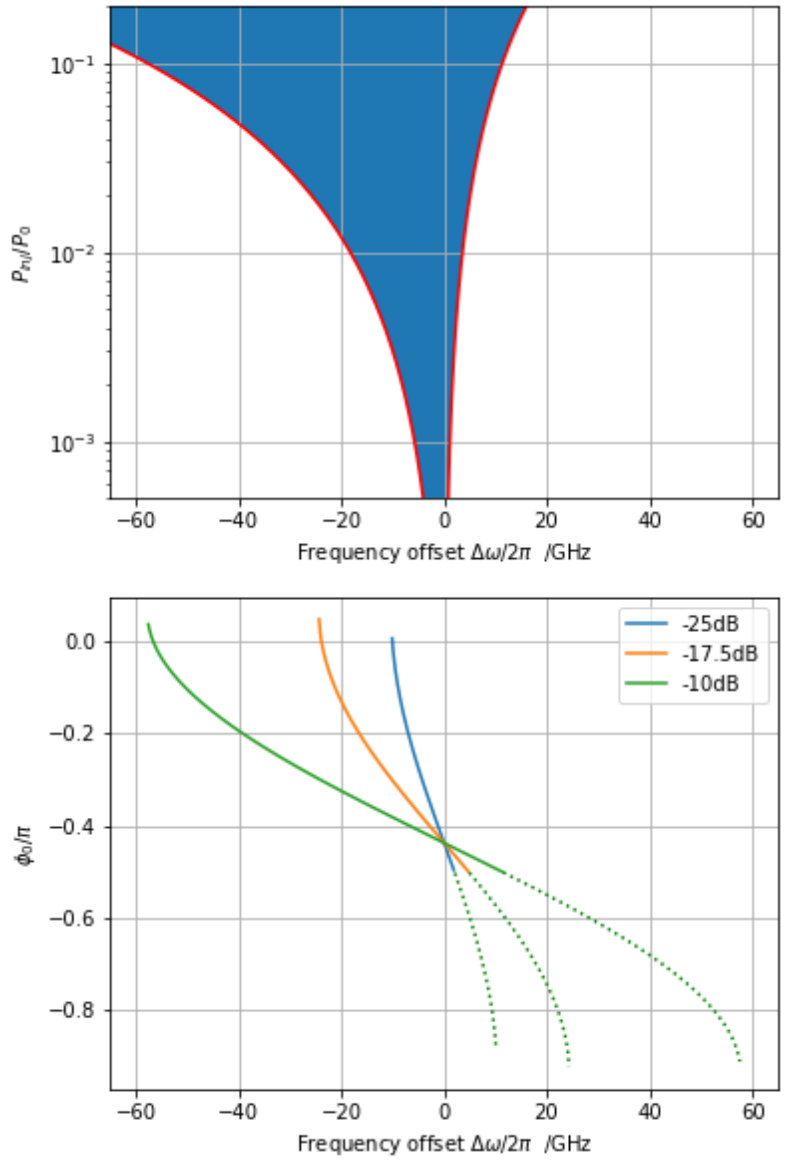


Fig. 4.3 Calculation of the stable locking range for injection locking using κ=35 GHz and α=5.The upper graph shows the locking range as function of the injection ratio. The two red curves are the extreme detuning values while out the lock is not stable. In the lower graph has been calculated the phase difference as function of the detuning for different injection ratios. The dashed portion represent the unstable lock for phase lower than $-\pi/2$

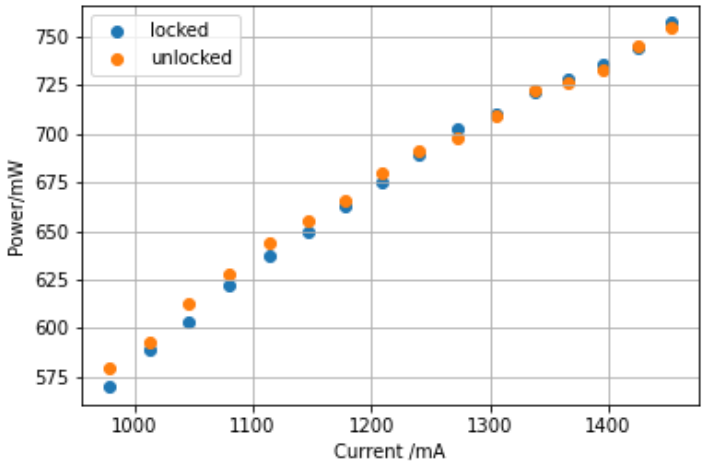


Fig. 4.4 Optical power emitted by the slave laser measured in free running (orange dots) and locked conditions (blue dots) keeping fixed the seed power and changing the current of the slave laser. It is possible to notice a regular interval on the value of current that generate injection locking.

Figure 4.3 shows the OIL behavior calculated for the slave laser used in the experiment, evaluated for different injection ratios and frequency detuning. The stable lock region is represented by the shaded region between the two red lines (so the extreme values of the locking range). The parameters κ, representing also the spacing of the longitudinal cavity mode of the laser, has been chosen as 36 GHz and while α=5. Using equation 4.6, the Locking range has been estimated as 29 GHz at -20dB of injection and about 90 GHz at -10dB of injection. The lower panel shows the phase offset between master and slave in the stable region calculated with 4.7 for different injection ratio. One can notice that as the frequency difference increases, ϕ_0 tends to approach $-\pi/2$ until the laser enters in a not-stable region, represented by the dashed lines in the picture.

The estimation of the longitudinal cavity mode spacing of the diode was performed by fixing the seed laser's power and varying the slave laser's frequency via changes in the diode current.This process also affects the locking bandwidth; as the emitted power decreases, $\Delta\omega_L$ increases. This procedure was carried out under conditions of unstable locking to obtain a series of discrete frequency ranges where the slave laser could autonomously lock to the seed. The points in Figure 4.4 were recorded by varying the slave laser current and measuring power only when it autonomously locked to the seed.

As shown in figure 4.4, sweeping the slave laser current and keeping fixed the master frequency one can observe a OIL at regular current intervals of $31(2)$ mA: from the diode characterization the frequency dependence of the current is $-1.5(3)$ GHz/mA, so the frequency separation for every point is $46.5(9.5)$ GHz.

4.4 Frequency stabilization

Even though the lattice laser's frequency is stabilized by injection locking to the seed laser, the master laser also requires frequency stabilization to a superior reference. While an ECDL is designed for maximum stability, it remains susceptible to external perturbations such as thermal changes, mechanical vibrations, or mode hops.
A frequency control at the level of a few hundred kilohertz for several hours is essential for generating an optical lattice suitable for metrological purposes. A commonly employed solution involves locking the laser frequency to a resonance of a high-finesse cavity, which serves as a reference and transfers its spectral purity to the oscillator. Cavity linewidth scales with the Finesse as $\Delta\nu = FSR/\mathscr{F}$. Although a low linewidth indicates a good short-term frequency reference, environmental perturbations and cavity drifts cause the resonance position to shift over time, thereby reducing long-term stability. This issue can be mitigated by locking the cavity to a superior long-term reference, such as an atomic resonance via a spectroscopy cell, which transfers its enhanced stability to the laser.

In this section, I will describe the design and realization of a transfer lock cavity developed to stabilize the master laser frequency, aiming for a short-term linewidth of less than 100 kHz. This activity constituted my primary activity during my period as a visiting student. The 813 nm laser is locked with the Pound-Drever-Hall technique to a Zerodur $\mathscr{F}$=16000 plano-concave cavity. The cavity's length is, in turn, locked to an externally stabilized 689 nm red laser, which is itself locked to an atomic reference, thereby providing long-term stability to mitigate the natural cavity drift. In future, it will also be possible to use as reference laser a 698 nm radiation, corresponding to the wavelength of the Sr clock transition. This will introduce a phase correlation between the lattice and the clock laser, locked to an ultrastable cavity [179], necessary to perform quantum non-demolition measurements in the passive clock under development [13].

First I will describe the design considerations kept in account to obtain a good resonator shielded by the environmental noise, than I will describe the cavity setup implemented and the optical system built to lock the lattice laser to the reference laser.

4.4.1 Design consideration

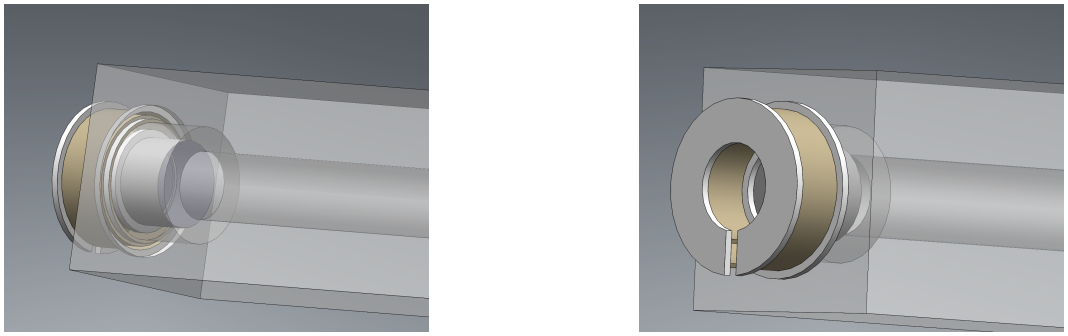
The precision of the locking point for an optical cavity used as a frequency reference primarily depends on its linewidth, which is, in principle, determined solely by the reflectivity of the mirrors and the length of the optical path.
The cavity employed for this laser stabilization has been built with an ultra-low expansion glass Zerodur®spacer 15 cm long and with square section 2.5 cm wide.It features a cylindrical hole parallel to its axis, at the ends of which two mirrors manufactured by Layertec are positioned. One mirror is flat while the other has a curvature radius R=50 cm. Both present an high reflectivity coating between 660 and 720 nm (Transfer lock) and 800-830 nm (red or lattice lock). From these specification they form a 1 GHz free spectral range cavity with expected linewidth of $111(38)$ kHz for the transfer lock and $64(25)$ kHz for the red lock.

To have a valid reference for long times is necessary to keep in account the possible effect that can influence the cavity resonances, designing a system able to shield the cavity from environmental disturbances and to suppress the shift of the locking point. One can start considering that two consecutive longitudinal cavity modes are separated in frequency by a free spectral range defined as:

$$\Delta\nu_{FSR} = \frac{c}{2nd} \tag{4.8}$$

where c is the speed of light, n is the refraction index and d is the cavity length. It is so dependent solely on the optical path that light travels in a round trip inside the cavity and it is so sensitive to variation both of geometrical length and refraction index. This sensitivity of the cavity resonance can be expressed deriving equation 4.8 and dividing by $\Delta\nu_{FSR}$:

$$\frac{\Delta\nu}{\Delta\nu_{FSR}} = -\frac{\Delta d}{d} - \frac{\Delta n}{n} \tag{4.9}$$



(a) (b)

Fig. 4.5 Insight of the piezo stack used to connect the flat mirror to the spacer. A Macor ring (white) connects the external piezo (brown) with the spacer. The internal piezo is connected from one side to the bigger actuator, from the other it is glied to the mirror.

The first source of noise influencing the variation of the optical path is the change of the refraction index, and it mainly depends on the pressure and the temperature of the gas where the light is propagating. A simple way to get rid of this effect is placing the cavity in vacuum. It is possible to estimate the fractional variation of the refraction index because of the pressure fluctuations as [180]:

$$\frac{\Delta n}{n} \approx 2.65 \cdot 10^{-7} \text{mbar}^{-1} \Delta P \tag{4.10}$$

While pressure cannot be measured directly within the vacuum system, it can be estimated from the ion pump's current, which operates to maintain the vacuum level. Considering the operating condition $p \approx 10^{-8}$ mbar, fluctuations of 4% of the pressure influence the fractional frequency stability at the level of 10^{-16} [181]. This level of vacuum can be easily reached with commercial ion pumps and standard vacuum components.

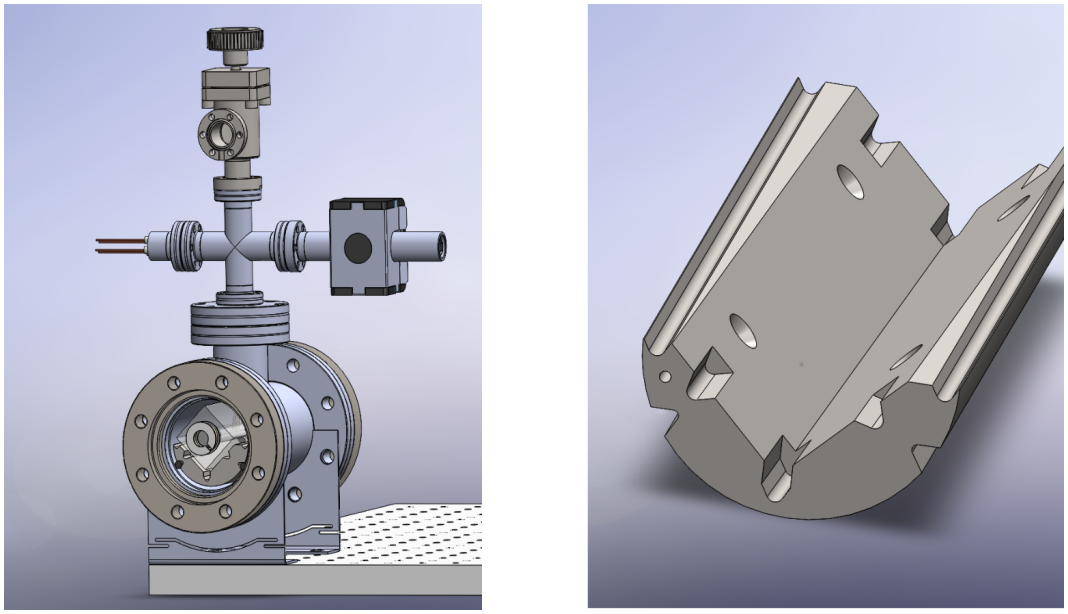
The second effect that influences the optical path is the change in geometrical length of the cavity. The main sources of noise affecting it are the thermal expansion of the cavity and the vibrations, inducing a deformation of the mirror spacer and a misalignment from the optical axis. Thermal drifts of the environment can cause slow but strong drifts in the cavity frequency that have to be prevented or actively compensated.
The first approach is to thermally isolate the cavity from the environment, decoupling it from eventual temperature variations. Convective motions are suppressed placing the cavity in vacuum. At the same time, heat exchange by conduction is reduced by

suspending the mirror spacer on 4 Viton balls (thermal conductivity 0.2-0.3 $\mathrm{W/m/K}$) decoupling it from the stainless steel holder. Fast temperature fluctuations are mitigated by the high thermal capacity of the stainless steel holder. Furthermore, as well as the vacuum can, it also constitutes a shallow metallic shield reflective thermal radiation from the environment. For this reason an active temperature control has not be implemented.
The second straightforward approach is building the mirror spacer in a material as much as possible insensitive to thermal variation. The spacer has been manufactured in ultra-low expansion glass Zerodur, with thermal expansion coefficient vanishing at room temperature making it at first approximation immune to temperature noise. Unfortunately it is not sufficient to build a transfer cavity, because one mirror is fixed on a piezoelectric element to enable active control of the cavity length: thermal expansion is limited by mounting the mirror on a piezo stack built in a temperature insensitive configuration. It is composed of two concentric piezo rings as shown in figure 4.5. One piezo is glued between the spacer flat surface and a Macor ring, the other is between the Macor ring and the mirror. Due to this geometry the effect of the elongation on the mirror position is in first approximation null due to the opposite contribution of the two piezo rings, leaving the cavity length almost unperturbed. +

The third design constrain aims to improve the stability by suppressing the transmission of the vibration toward the cavity. As shown in figure 4.6a, a shallow attenuation of the vibration from the breadboard is provided by the two spring-like supports. The main design approach is instead based on decoupling the mechanical elements separating them with rubber to dump the vibration transmission: 4 Viton rods separate the holder from the vacuum can and 4 Viton balls decouple the spacer from the metallic holder. Moreover, the 2.5 kg stainless steel holder itself constitutes an inertial dump to attenuate the fast vibration. The spacer is supported by the 4 Viton balls placed in the Airy points and the symmetric design provide a suppression of the sensitivity to horizontal vibrations. Considering this geometry, the relative elongation of a Zerodur cavity for Poisson effect induced by the tilt of the mirror around the optical axis can be described as [182]:

$$\left(\frac{\Delta l}{l}\right)_{Poisson} = \frac{\nu \rho W}{\sqrt{2}E} = 1.37 \cdot 10^{-10}/(m/s^2) \tag{4.11}$$

depending on the width of the spacer W and from the mechanical properties of the used material ν,ρ and E respectively the Poisson ratio, the density and the Young's



(a) (b)

Fig. 4.6 (a) CAD design of the transfer cavity in the vacuum can. The vacuum system is clamped to the breadboard through two supports and the optical access is enabled by two not-coated viewports. The vacuum can is connected to an ion pump (right), an angle valve (top) and 4 electric feedthrough (left). (b) Zoom in of the stainless steel holder for the spacer.The square groove hosting the spacer is 2° tilted to avoid etalon effects. Circular holes (placed at the Airy points of the spacer) and the smaller grooves host the Viton balls and rods.

modulus. Finally, a home-made wood box (more precisely manufactured in Medium-Density Fibreboard or MDF) protects the system from acoustic noises and all-the system is placed in an anti-acoustic room.

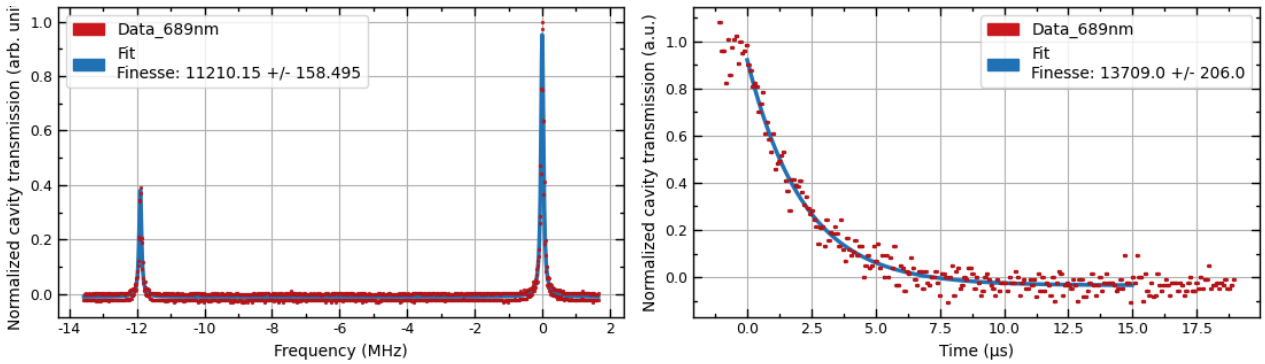
4.4.2 Cavity setup

The cavity has been assembled from scratch with a flat mirror, glued on a piezo-stack, and a curved mirror directly glued on a 15 cm Zerodur spacer. The piezo-stack (Figure 4.5) has been assembled with Noliac piezo rings and Macor rings glued with EPO TEK 353ND. They can handle a voltage between -150 and 200 V provided through Kapton isolated wires soldered on the side surfaces of the rings with the vacuum compatible Allectra 315-LF-solder UHV. It has been connected to the Zerodur spacer with Masterbond EP21TCHT-1 epoxy glue. Both glues are vacuum compatible and the choice has been managed considering the temperature tolerance

of the different components: the EPO-TEK one, in fact, requires a shorter waiting time to be effective but needs a degassing process and an oven baking as well.
A critical point is gluing the curved mirror to the spacer in order to generate a cavity with the flat one when a laser beam is sent: a test optical bench has been prepared to look for cavity modes moving the curved one through a 4 direction sideshifter and gluing it in the final position where low-order cavity modes are visible in transmission.
As the two mirrors are well aligned in cavity configuration, optimized on a TEM00 mode, the Finesse has been measured using both the sideband and the ring-down technique: the first is easier to perform, so it has been used to validate the alignment before the gluing, the latter instead is more accurate but also more demanding, and so it has been used after the assembling phase.
The sideband technique is based on modulating the laser injected in the cavity with an EOM to introduce a couple of sidebands detuned of a known value: scanning the cavity length, one can observe the transmission signal with a fast photodiode tracking the carrier and the sidebands. Knowing the frequency distance between sideband and carrier and fitting them with an Airy profile it is possible to extrapolate the linewidth of the transmitted light and thus the Finesse (figure 4.7a). This technique is limited by several external factors, such as the speed of the detector, the noise of the laser and the speed of the sweep.
Instead, a complementary approach in the time domain is the basis of the ring-down method. The light coupled in cavity continues traveling inside the cavity stored into the resonator but, depending on the mirror reflectivity, at each round trip part of the photons will be lost. Photons present a typical lifetime into the resonator depending on the Finesse and it can be measured abruptly interrupting the light directed to the cavity: the cavity transmission, measured by an avalanche photo-detector (APD), will decay exponentially with a typical decay time τ_{cav} that can be extracted from a fit (figure 4.7b). The relationship between the decay time and the Finesse can be described as:

$$\tau_{cav} = \frac{1}{\pi \Delta \nu_{cav}} = \frac{\mathscr{F}}{\pi \Delta \nu_{FSR}} \tag{4.12}$$

Table 4.1 reports the value of Finesse estimated with the two methods and the corresponding cavity linewidth.



(a) (b)

Fig. 4.7 (a) Cavity transmission as a function on the frequency detuning from the carrier, obtained by scanning the resonator length with the moving mirror. The sideband at the left evidence the laser modulation at 11.9 MHz and has been also used to calibrate the scan. (b) Cavity transmission in time chopping the laser beam with an AOM and fitting the decay to do a ring down measurement. The uncertainty on the single acquisition has been evaluated from the fit.

Table 4.1 Cavity Finesse measured with different techniques. The estimation has been calculated from the mirror reflectivity. Values reported as average and standard deviation from repeated measurements. Linewidth estimated from the ring-down Finesse.

$\mathscr{F}$	689 nm	813 nm
Estimated	9000(3100)	15700(6300)
Sidebands	11500(1500)	—
Ring Down	13300(500)	16100(700)
Linewidth/kHz	75(3)	62(4)

After the characterization of the optical cavity, it has been placed on the self-designed stainless steel holder, manufactured by the mechanical workshop of the University (Fig. 4.6b): the groove has been set to keep the cavity 2° tilted with respect to the viewports to avoid etalon effects. The vacuum system has been assembled with a commercial ConFlat 63 can connected with a cross flange to an ion pump, an angle valve and a feedthrough flange connected to the cables to pilot the piezo rings (see Figure 4.6a). To avoid outgasing from the Viton elements they have been baked for several days at 150 °C. After assembling the whole cavity system, it has been baked for 1 week in oven at 120 °C reaching a pressure below 1×10^{-8} mbar

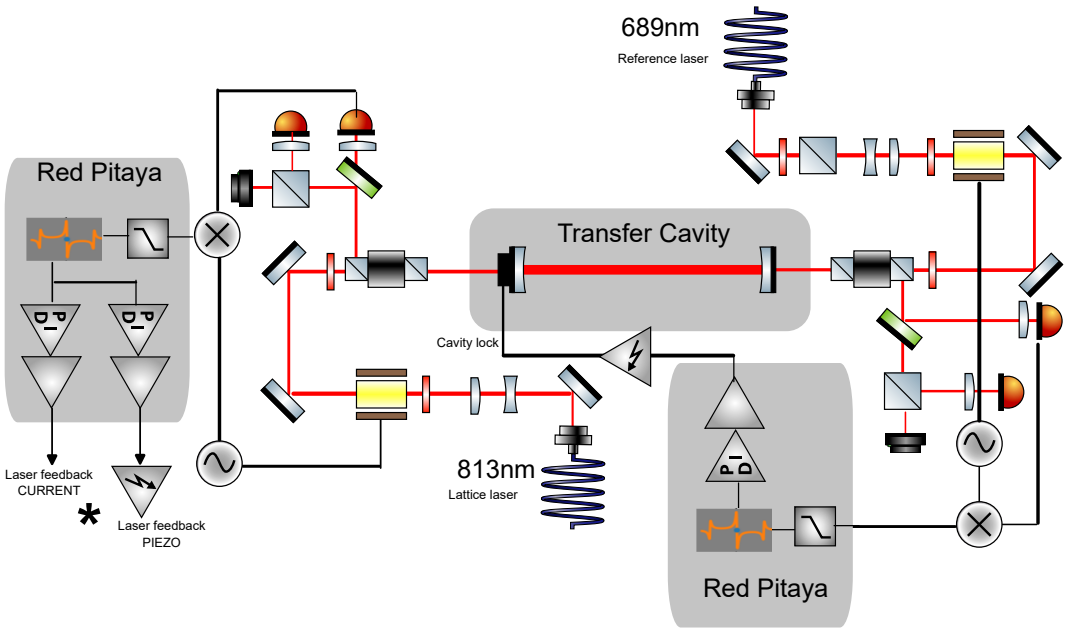


Fig. 4.8 Optical setup to lock the 813 nm lattice laser (dark red lines) and the 689 nm reference laser (light red) to the same cavity.

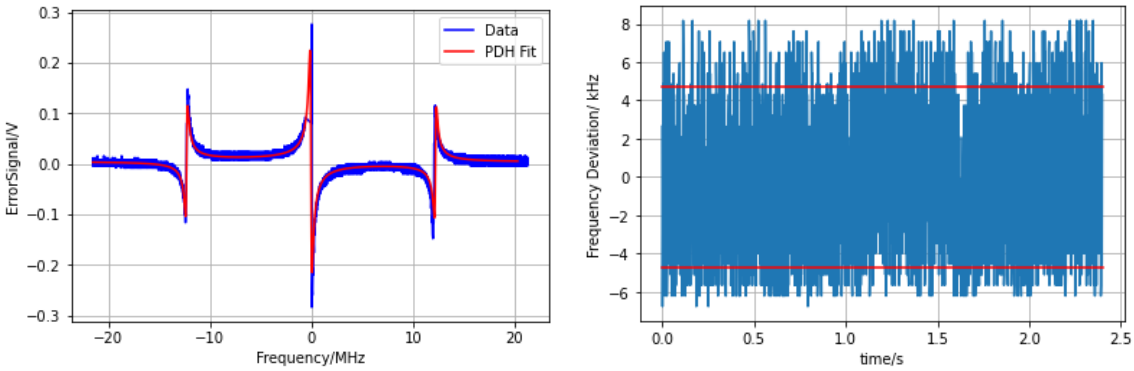
measured by the ion pump. During the baking, the feedthrough connected to the piezo rings have been shorted to avoid build-up voltages that could damage them.

4.4.3 Optical and electronic setup

The simple and robust optical setup to lock the lattice laser on the high-finesse cavity is represented in Figure 4.8. The central element is the transfer cavity contained in the vacuum system described in the previous section and placed at the center of the optical table. The optical path has been arranged to perform a Pound-Drever-Hall (PDH) lock for both the lasers. The 813 nm light comes from the master laser (placed in a breadboard just on top of the cavity) while the reference light at 689 nm is stabilized on an external $\mathscr{F} = 15000$ cavity referenced on a strontium spectroscopy cell. Both are sent to the cavity breadboard through polarization-maintenance optical fibers. Then home-built free-space EOMs modulate the light to generate the sidebands and then a couple of lenses form a telescope to match the cavity modes for each wavelength. The EOMs are based on a lithium-niobate crystal (Nortus Optronics GmbH) and a LC circuit resonant at 11.9 MHz, and a half-wave plate is placed in front of the modulator to control the input polarization to avoid

RAM effects due to polarization imbalance with respect to the birefringence axis. The reference and the lattice lasers are coupled in cavity from the opposite sides. To implement a Pound-Drever-Hall lock is necessary to couple light in cavity and at the same time extract the non-resonant portion that is reflected by the cavity to generate the error signal [183]. The adopted solution includes two Faraday isolators placed in front of the cavity optimized to transmit the beam toward the cavity. The counter-propagating beam is so extracted sideways and, because it presents two components at different wavelength, separated with dichroic mirrors (green elements in figure 4.8). The first one is the reflection of the same laser, used to generate the PDH error signal and collected by a home-designed 1 GHz bandwidth photodiode. The second one is instead the cavity transmission of the other laser, used just as alignment monitor and detected with a commercial DET 10 A2 photodetector from Thorlabs with bandwidth of 350 MHz.

Typical laser power injected in cavity in regular operation are of the order of 30 µW at 813 nm and 20 µW at the reference wavelength. Even using the dichroic mirrors, a tiny portion of the transmitted light pollutes the photodiodes employed to generate the error signal. The power unbalance between the two laser beams was set in order to fix this problem. As the cavity presents higher finesse at 813 nm, the transmitted power is lower with respect to the 689 nm one. The lattice laser power can be so slightly increased in order to have a higher signal-to-noise ratio on the photodetector responsible for the lattice lock without excessively affecting the transfer lock. The automatic control to lock both the laser and the cavity length has been implemented on a RedPitaya board STEMlab 125-14 integrated in an amplifier box designed and produced by the electronic workshop of the university. It uses the PyRPL software to elaborate two PDH error signals, one from the lattice lock, the other for the transfer lock,and with a PID module it generates three different feedback signal through a Digital to Analog Converter (DAC). If the laser lock is ON, it provides a fast feedback on the master laser injection current and a slow one on the piezo control. If the transfer lock is ON, it generates high voltage feedback to pilot one of the piezo ring of the transfer cavity, locking the length to be resonant with the 689 nm laser. In addition, this RedPitaya board can also generate a constant offset at high voltage (between 0 and 150 V) used to pilot the second piezo of the cavity: one piezo actuator can be used to bring the cavity close to the resonance while the other to compensate for the noise.



(a) (b)

Fig. 4.9 (a)PDH error signal of the cavity lock. From the fit the linear slope close to resonance is C=$-0.28(8)$ MHz/V (b) In-loop error signal detected in time for the 813 nm laser locked to the transfer cavity. Vertical axis converted from voltage to frequency through a conversion factor obtained from the PDH fit. Red lines evidence the FWHM of the distribution.

4.5 PDH stabilization

As described in the previous sections, the high finesse cavity, the stable cavity holder the high bandwidth electronics (until 50 MHz) and the optical locking setup make possible a simple and robust locking setup to transfer the spectral purity of the reference laser to the lattice one. The coupling of both the lattice and the reference laser is optimized on the TEM_{00} mode with more than 60% of coupling efficiency and a ratio compared to the $TEM_{01/10}$ modes more than 5 times. Also this factor contributes to obtain a good PDH error signal as the one represented in Figure 4.9(a).

4.5.1 Lattice lock

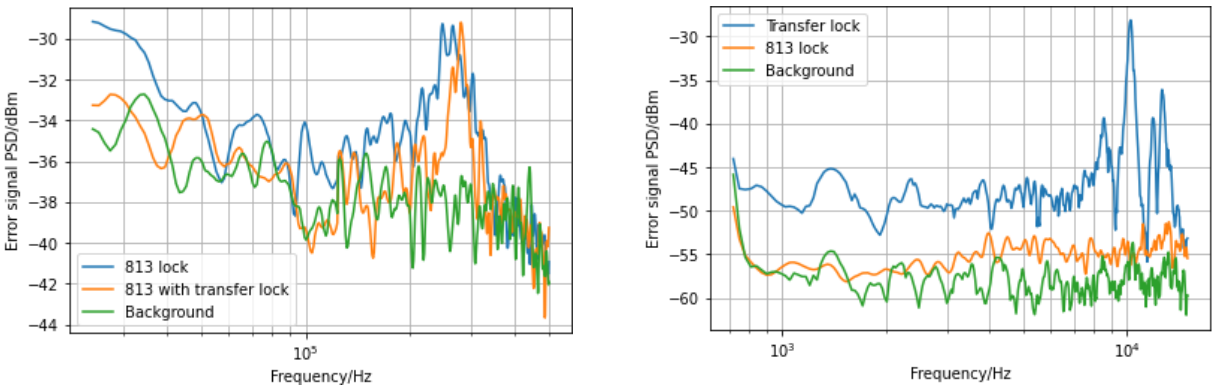
As previously described, this lock aims to stabilize the frequency of the 813 nm laser and reduce the linewidth below 100 kHz. The linewidth estimation is not trivial for optical frequencies at the kHz level. A self-heterodyne detection [177] would require a 3 km long optical fiber considering a 100 kHz narrow laser, not present in the lab. For this reason a rough estimation has been done from a statistical analysis of the in-loop error signal measured in time. The error signal represents the deviation from the locking point in term of voltage. From the fit of the PDH model close to the resonance in 4.9(a), one can convert the voltage deviation in a frequency

deviation when the lock is ON. The data follows a Gaussian distribution and one can estimate the frequency linewidth of the laser locked to the cavity as the full width half maximum (FWHM) of the distribution. From the time distribution of the error signal for the lattice laser locked to the cavity (reported as an example in the graph 4.9(b)),it is possible to estimate an in-loop linewidth of $11(2)$ kHz evaluated for more than 2 seconds with a sampling rate of 1 ms.
A limitation of this technique reducing the accuracy of the estimation arises from the speed of the scan used to evaluate the PDH shape: a too fast scan does not allow the light to couple in cavity reducing the error signal and inducing so a shallower slope. In this case the linewidth would be underestimated. On the other side, a too slow scan makes the trace more susceptible to noises or jitter distorting the fit.

Other information about the lock transfer function comes from the analysis in frequency of the power spectral density of the in-loop error signal. Figure 4.10(a) compares the PSD of the error signal of the laser locked to the cavity with the transfer lock OFF (blue) and ON (yellow). Green line shows the background noise of the detection system (photodiode, cables and RedPitaya board). In this case the gain has been amplified to excite the so-called "servo bump" of the lock, so where the transfer function approaches the border of the bandwidth. The position of the servo-bump can be considered as the locking bandwidth and the typical target is increasing it pushing the PSD close to the background detection level and moving the servo bump at higher frequencies. Optimizing the digital PID gains, one can push the peak of the noise up to 250 kHz, obtaining so a wide locking bandwidth to suppress the noise. Aiming to make the lock stronger, a further digital low pass filter has been implemented to remove the high-frequency noise that the system can detect but cannot compensate. It is possible to notice that the presence of the transfer lock reduces the global noise of the error signal and narrows the servo bump.

4.5.2 Transfer Lock

Aiming to increase the long-term stability of the transfer cavity, the transfer lock operates on the moving mirror controlling the cavity length making it resonant to the 689 nm reference laser. Thanks to this feature the transfer cavity can actively compensate the slow frequency drift of the resonant frequency and can introduce a phase correlation between the two lasers. Aiming to only remove drift, the transfer lock has to be slow enough to avoid active narrowing of the lattice laser linewidth:



(a) (b)

Fig. 4.10 (a) PSD of the lattice lock evidencing a servo bump at about 250 kHz. Activating the transfer lock (orange) the servo-bump is narrowed and the global noise reduced (b) PSD of the slower transfer lock, limited by the piezo bandwidth at 10 kHz. Orange line shows that the high frequency noise of the transfer lock is not transferred to the lattice laser.

in this case, it would introduce additional noise with the effect of increasing the final linewidth with respect to the estimated $11(2)$ kHz. As demonstrated in other experimental setups [184], a good cavity coupling of the reference light and a sharp slope of the reflected signal enables the implementation of a side of peak lock. In this case a PDH lock is preferable because it makes possible to push the bandwidth toward higher frequencies in order to introduce a phase correlation between the reference and the lattice: it will be particularly useful when the reference laser will be changed from the 689 nm one, used for the intercombination line of the strontium, to a 698 nm one used for the strontium clock transition and locked to an ultrastable cavity. Figure 4.10(b)shows the PSD of the transfer lock error signal when the cavity length is actively controlled.
The blue curve shows a servo bump at about 20 kHz, also limited by the bandwidth of the piezoelectric actuators whose mechanical resonances have been observed at some kHz. The orange curve represents the noise of the 813 nm laser when the transfer lock is ON and evidences that the high-frequency noise of the reference laser is not transferred to the lattice laser. Even in this case, a digital low-pass filter has been implemented to reduce the noise to compensate at few kilohertz.

When both the transfer and the lattice lock are active, the lattice lock benefits from the cavity control reducing the noise in the lock PSD, narrowing the servo bump and reducing the overall noise.

4.6 Conclusion

In this chapter I described the optical system that I designed, built and characterized, to generate a lattice laser for an optical clock whose frequency has been stabilized and drift-compensated with a transfer lock cavity.
The transfer cavity has been placed in a silent room containing also the clock laser ultrastable cavity [179] and it is currently employed to frequency stabilize the master laser at 813 nm. Only minor modifications have been applied on the experimental system. It can stay locked without human intervention for several hours efficiently removing the cavity drift. The estimated laser linewidth seems to widely respect requirements of few tens of kHz. The slave laser that I built, locked by injection locking to the seed and provides the optical power for the *mHz machine*, while another high power slave laser is planned to be locked to the same master to generate the optical lattice for the *Zero deadtime* passive clock.

Chapter 5

Conclusions

5.1 Conclusions

This thesis details the activities undertaken and the results obtained during my three-year Ph.D. program, specifically focusing on the operation of the INRiM optical lattice clock, IT-Yb1. The clock's systematic uncertainty budget was characterized, achieving a relative accuracy of 1.9×10^{-17}, primarily limited by the physical package. The level of automation for unattended operations was significantly enhanced through improvements to the physical package, including automatic laser locking and the integration of a new lattice laser. Furthermore, a longitudinal sideband cooling technique was implemented within the clock cycle to reduce the atomic ensemble's temperature, leading to a greater level of control over the atoms.
These upgrades collectively increased the reliability and robustness of IT-Yb1 for extended operations, enabling the clock to run almost continuously for over a year and a half, achieving 40% of uptime during some months.

Two absolute frequency measurements of the ytterbium clock transition were performed: one local measurement against the INRiM Cs fountain, spanning over 900 hours, and another remote measurement against the French Cs-Rb fountain, conducted for approximately three months via an optical fiber link.Both results aligned with the CCTF recommended values and represent the lowest uncertainty ever reported for Yb measurements involving fountains, constrained by the systematics of the primary standards. A portion of the local campaign was carried out using an innovative microwave generation scheme derived from an ultrastable optical

oscillator. Additionally, the first direct measurement of the Yb/Rb frequency ratio was obtained.

IT-Yb1 participated in two international campaigns of optical frequency comparisons in March 2022 and March 2023. They involved several European clocks from SYRTE, NPL, PTB, VTT and UMK, beyond other international partners, connected via fiber link and GPS satellite continuously measuring for more than one month. These constitute the largest campaign ever seen for optical clocks. Several ratios of optical frequency standards have been measured, some for the first time, and the results are close to the publication.

Clock data collected operating IT-Yb1 during these years have been employed in local and international time scale generation, showing the capability of the optical frequency standard in replacing the microwave clocks in time-keeping.
We regularly submitted the clock data to the Bureau International des Poids et Mesures (BIPM) for the calibration of the Universal Coordinated Time (UTC), the most diffused international time scale. Notably, our participation, spanning 16 consecutive months, constitutes the longest continuous contribution so far from an optical clock to UTC. Concurrently, through our collaboration with the INRiM time group, IT-Yb1 data has been instrumental in steering a hydrogen maser, thereby generating an optical time scale for over a year. Despite the limited amount of uptime, this timescale demonstrated a sub-nanosecond displacement from UTC in several months.

Between the second and third year, I spent 7 months at the University of Amsterdam, where a superradiant strontium optical clock is under development. There, my primary contributions involved building and designing the lattice laser system and a transfer cavity to lock the lattice frequency with respect to an external reference, efficiently removing the cavity drift.

Most of the activities described in this thesis contribute directly to a new definition of the SI second. Our work, encompassing absolute frequency measurements, clock validations through optical frequency ratios, and optical clock contributions to UTC and local time scales, aligns with the criteria established by the CCTF in anticipation of this redefinition

5.2 Next steps

Several activities are in progress involving IT-Yb1. First the new data collections will continue to contribute to UTC calibration and eventually it will constantly assist IT-CsF2 in the UTC(IT) steering. Regarding future enhancements to the clock's experimental system, we're working to implement a new 30 cm-long ultrastable cavity. This upgrade will boost the clock's instability by an order of magnitude (currently limited by oscillator noise) and consequently reduce the statistical uncertainty in our measurements. Both clock accuracy characterization and future clock comparisons will benefit significantly from this improvement.
Furthermore, we are initiating the design of the physical package for the new IT-Yb2 optical lattice clock. This new system is not planned to replace the current IT-Yb1 but to operate in conjunction with it. IIt will incorporate several features aimed at overcoming the structural limitations of IT-Yb1, including: a separated 2D-MOT to trap atoms directly from the oven (thereby reducing the flux of hot atoms toward the lattice and preventing oven contributions to the BBR shift), a lattice laser enhancement cavity (enabling the exploration of higher trap depths for improved characterization of the lattice shift), and a BBR/Stark shield. TThanks to these advancements, we are confident in achieving a fundamental clock uncertainty at the level of 10^{-18}.

In the context of the redefinition of the second, we plan to participate in new international clock comparison campaigns to measure the ratios between different atomic frequency standards and to compare these results with those from the two campaigns described in this work. The next campaign is scheduled to take place between March and April 2025, funded by the Euramet TOCK project. This event will involve INRiM hosting the PTB transportable strontium lattice clock, with other European partners connected via fiber link. During this campaign, we will introduce several novelties into the clock cycle: the implementation of the Sysiphus cooling technique (developed from the sideband cooling studies and setup detailed in this thesis) to reduce both radial and longitudinal atomic temperature; a reduction of the trapping potential from 100 to 50 E_R (which will impact density and lattice shift); and a change in the interrogation order, which has already improved measurement stability at the level of $1 \times 10^{-15}\, 1/\sqrt{\tau/\mathrm{s}}$.

5.3 List of Publications

- **Coherent Optical-Fiber Link Across Italy and France**, *C. Clivati, M. Pizzocaro, E. Bertacco,* ***S. Condio****, G. Costanzo, S.Donadello, I. Goti, M. Gozzelino, F.Levi, A. Mura, M. Risaro, D. Calonico, M. Tønnes, B. Pointard, M. Mazouth Laurol, R. Le Targat, M. Abgrall, M. Lours, H. Le Goff, L. Lorini, P.-E. Pottie, E. Cantin, O. Lopez, C. Chardonnet, and A. Amy-Klein*, Phys. Rev. Appl. 18 (Nov, 2022) 054009. DOI https://doi.org/10.1103/PhysRevApplied.18.054009

- **Absolute frequency measurement of a Yb optical clock at the limit of the Cs fountain**, *I. Goti,* ***S. Condio****, C. Clivati, M. Risaro, M. Gozzelino, G. A. Costanzo, F. Levi, D. Calonico, and M. Pizzocaro*, Metrologia 60 no. 3, (May, 2023) 035002. DOI: https://doi.org/10.1088/1681-7575/accbc5

- **Year-long optical time scale with sub-nanosecond capabilities**, *V. Formichella, G. Signorile, T. T. Thai, L. Galleani, M. Pizzocaro, I. Goti,* ***S. Condio****, C. Clivati, M. Risaro, F. Levi, D. Calonico and I. Sesia*, OPTICA, Vol. 11, Issue 4, pp. 523-530 (2024),509706. OPTICA, Vol. 11, Issue 4, pp. 523-530 (2024),509706. https://doi.org/10.1364/OPTICA.509706

References

[1] Kyle Beloy, Martha I. Bodine, Tobias Bothwell, Samuel M. Brewer, Sarah L. Bromley, Jwo-Sy Chen, Jean-Daniel Deschênes, Scott A. Diddams, Robert J. Fasano, Tara M. Fortier, Youssef S. Hassan, David B. Hume, Dhruv Kedar, Colin J. Kennedy, Isaac Khader, Amanda Koepke, David R. Leibrandt, Holly Leopardi, Andrew D. Ludlow, William F. McGrew, William R. Milner, Nathan R. Newbury, Daniele Nicolodi, Eric Oelker, Thomas E. Parker, John M. Robinson, Stefania Romisch, Stefan A. Schäffer, Jeffrey A. Sherman, Laura C. Sinclair, Lindsay Sonderhouse, William C. Swann, Jian Yao, Jun Ye, Xiaogang Zhang, and Boulder Atomic Clock Optical Network (BACON) Collaboration*. Frequency ratio measurements at 18-digit accuracy using an optical clock network. *Nature*, 591(7851):564–569, 2021.

[2] Alexander Aeppli, Kyungtae Kim, William Warfield, Marianna S. Safronova, and Jun Ye. Clock with 8×10^{-19} systematic uncertainty. *Phys. Rev. Lett.*, 133:023401, Jul 2024.

[3] Noriaki Ohmae, Masao Takamoto, Yosuke Takahashi, Motohide Kokubun, Kuniya Araki, Andrew Hinton, Ichiro Ushijima, Takashi Muramatsu, Tetsuo Furumiya, Yuya Sakai, et al. Transportable strontium optical lattice clocks operated outside laboratory at the level of 10- 18 uncertainty. *Advanced Quantum Technologies*, 4(8):2100015, 2021.

[4] Rudolf Grimm, Matthias Weidemüller, and Yurii B Ovchinnikov. Optical dipole traps for neutral atoms. In *Advances in atomic, molecular, and optical physics*, volume 42, pages 95–170. Elsevier, 2000.

[5] D.W. Allan. Statistics of atomic frequency standards. *Proceedings of the IEEE*, 54(2):221–230, 1966.

[6] Fritz Riehle. *Frequency standards: basics and applications*. John Wiley & Sons, 2006.

[7] William J Riley and David A Howe. Handbook of frequency stability analysis. *NIST special publications*, 2008.

[8] Andrew D. Ludlow, Martin M. Boyd, Jun Ye, E. Peik, and P. O. Schmidt. Optical atomic clocks. *Rev. Mod. Phys.*, 87:637–701, Jun 2015.

[9] W. M. Itano, J. C. Bergquist, J. J. Bollinger, J. M. Gilligan, D. J. Heinzen, F. L. Moore, M. G. Raizen, and D. J. Wineland. Quantum projection noise: Population fluctuations in two-level systems. *Phys. Rev. A*, 47:3554–3570, May 1993.

[10] G John Dick. Local oscillator induced instabilities in trapped ion frequency standards. In *Proceedings of the 19th Annual Precise Time and Time Interval Systems and Applications Meeting*, pages 133–147, 1989.

[11] Andrea Caprotti, Matteo Barbiero, Marco G Tarallo, Marco G Genoni, and Gianluca Bertaina. Analysis of spin-squeezing generation in cavity-coupled atomic ensembles with continuous measurements. *Quantum Science and Technology*, 9(3):035032, 2024.

[12] William J Eckner, Nelson Darkwah Oppong, Alec Cao, Aaron W Young, William R Milner, John M Robinson, Jun Ye, and Adam M Kaufman. Realizing spin squeezing with rydberg interactions in an optical clock. *Nature*, 621(7980):734–739, 2023.

[13] William Bowden, Alvise Vianello, Ian R Hill, Marco Schioppo, and Richard Hobson. Improving the q factor of an optical atomic clock using quantum nondemolition measurement. *Physical Review X*, 10(4):041052, 2020.

[14] Grégoire Vallet, E Bookjans, U Eismann, S Bilicki, R Le Targat, and Jérôme Lodewyck. A noise-immune cavity-assisted non-destructive detection for an optical lattice clock in the quantum regime. *New Journal of Physics*, 19(8):083002, 2017.

[15] Richard Hobson, William Bowden, Alvise Vianello, Ian R Hill, and Patrick Gill. Cavity-enhanced non-destructive detection of atoms for an optical lattice clock. *Optics express*, 27(26):37099–37110, 2019.

[16] GW Biedermann, K Takase, X Wu, L Deslauriers, S Roy, and MA Kasevich. Zero-dead-time operation of interleaved atomic clocks. *Physical review letters*, 111(17):170802, 2013.

[17] Masao Takamoto, Tetsushi Takano, and Hidetoshi Katori. Frequency comparison of optical lattice clocks beyond the dick limit. *Nature Photonics*, 5(5):288–292, 2011.

[18] Marco Schioppo, Roger C Brown, William F McGrew, Nathan Hinkley, Robert J Fasano, Kyle Beloy, TH Yoon, Gianmaria Milani, D Nicolodi, JA Sherman, et al. Ultrastable optical clock with two cold-atom ensembles. *Nature Photonics*, 11(1):48–52, 2017.

[19] E. J. Angstmann, V. A. Dzuba, and V. V. Flambaum. Relativistic effects in two valence-electron atoms and ions and the search for variation of the fine-structure constant. *Phys. Rev. A*, 70:014102, Jul 2004.

[20] R. Lange, N. Huntemann, J. M. Rahm, C. Sanner, H. Shao, B. Lipphardt, Chr. Tamm, S. Weyers, and E. Peik. Improved limits for violations of local position invariance from atomic clock comparisons. *Phys. Rev. Lett.*, 126:011102, Jan 2021.

[21] P Wcisło, P Morzyński, M Bober, A Cygan, D Lisak, R Ciuryło, and M Zawada. Experimental constraint on dark matter detection with optical atomic clocks. *Nature Astronomy*, 1(1):0009, 2016.

[22] P Wcisło, P Ablewski, K Beloy, S Bilicki, M Bober, R Brown, R Fasano, R Ciuryło, H Hachisu, T Ido, et al. New bounds on dark matter coupling from a global network of optical atomic clocks. *Science advances*, 4(12):eaau4869, 2018.

[23] Jacopo Grotti, Silvio Koller, Stefan Vogt, Sebastian Häfner, Uwe Sterr, Christian Lisdat, Heiner Denker, Christian Voigt, Ludger Timmen, Antoine Rolland, et al. Geodesy and metrology with a transportable optical clock. *Nature Physics*, 14(5):437–441, 2018.

[24] Masao Takamoto, Ichiro Ushijima, Noriaki Ohmae, Toshihiro Yahagi, Kensuke Kokado, Hisaaki Shinkai, and Hidetoshi Katori. Test of general relativity by a pair of transportable optical lattice clocks. *Nature photonics*, 14(7):411–415, 2020.

[25] BIPM. Si brochure, practical realization of the definition of some important units. https://www.bipm.org/en/publications/mises-en-pratique, 2019.

[26] BIPM. Recommended values of standard frequencies.

[27] Fritz Riehle, Patrick Gill, Felicitas Arias, and Lennart Robertsson. The cipm list of recommended frequency standard values: guidelines and procedures. *Metrologia*, 55(2):188, feb 2018.

[28] Noel Dimarcq, Marina Gertsvolf, Gaetano Mileti, Sebastien Bize, CW Oates, Ekkehard Peik, Davide Calonico, Tetsuya Ido, Patrizia Tavella, Frédéric Meynadier, et al. Roadmap towards the redefinition of the second. *Metrologia*, 61(1):012001, 2024.

[29] Jérôme Lodewyck. On a definition of the si second with a set of optical clock transitions. *Metrologia*, 56(5):055009, sep 2019.

[30] Jérôme Lodewyck. A definition of the si second based on several optical transitions. *Journal of Physics: Conference Series*, 2889(1):012026, nov 2024.

[31] Renato Mannucci and Franco Cordara. *Misurare il tempo e la frequenza*. il Rostro, 1997.

[32] BIPM. https://webtai.bipm.org/ftp/pub/tai/Circular-T/cirt/cirt.411. Circular T411.

[33] INTERNATIONAL EARTH ROTATION and leap seconds announcement REFERENCE SYSTEMS SERVICE (IERS), Bulletin C. https://datacenter.iers.org/data/latestVersion/16_BULLETIN_C16.txt.

[34] BIPM. https://www.bipm.org/en/cgpm-2022/resolution-4. XXVII CGPM, resolution 4.

[35] Alexandra Tofful. *Advances in performance and automation of a single ytterbium ion optical clock*. PhD thesis, Imperial College London, 2023.

[36] François Lahaye, Giancarlo Cerretto, and Patrizia Tavella. Gnss geodetic techniques for time and frequency transfer applications. *Advances in Space Research*, 47(2):253–264, 2011. Scientific applications of Galileo and other Global Navigation Satellite Systems - I.

[37] Gérard Petit. Sub-10-16 accuracy gnss frequency transfer with ippp. *GPS Solutions*, 25(1):22, 2021.

[38] Gérard Petit, Amale Kanj, Sylvain Loyer, Jérôme Delporte, Flavien Mercier, and Félix Perosanz. $1\times$ 10- 16 frequency transfer by gps ppp with integer ambiguity resolution. *Metrologia*, 52(2):301, 2015.

[39] H. Schuh and D. Behrend. Vlbi: A fascinating technique for geodesy and astrometry. *Journal of Geodynamics*, 61:68–80, 2012.

[40] Cecilia Clivati, Roberto Ambrosini, Thomas Artz, Alessandra Bertarini, Claudio Bortolotti, Matteo Frittelli, Filippo Levi, Alberto Mura, Giuseppe Maccaferri, Mauro Nanni, Monia Negusini, Federico Perini, Mauro Roma, Matteo Stagni, Massimo Zucco, and Davide Calonico. A vlbi experiment using a remote atomic clock via a coherent fibre link. *Scientific Reports*, 7(1):40992, 2017.

[41] Marco Pizzocaro, Mamoru Sekido, Kazuhiro Takefuji, Hideki Ujihara, Hidekazu Hachisu, Nils Nemitz, Masanori Tsutsumi, Tetsuro Kondo, Eiji Kawai, Ryuichi Ichikawa, Kunitaka Namba, Yoshihiro Okamoto, Rumi Takahashi, Junichi Komuro, Cecilia Clivati, Filippo Bregolin, Piero Barbieri, Alberto Mura, Elena Cantoni, Giancarlo Cerretto, Filippo Levi, Giuseppe Maccaferri, Mauro Roma, Claudio Bortolotti, Monia Negusini, Roberto Ricci, Giampaolo Zacchiroli, Juri Roda, Julia Leute, Gérard Petit, Federico Perini, Davide Calonico, and Tetsuya Ido. Intercontinental comparison of optical atomic clocks through very long baseline interferometry. *Nature Physics*, 17(2):223–227, 2021.

[42] N. D. Lemke, A. D. Ludlow, Z. W. Barber, T. M. Fortier, S. A. Diddams, Y. Jiang, S. R. Jefferts, T. P. Heavner, T. E. Parker, and C. W. Oates. Spin-$1/2$ optical lattice clock. *Phys. Rev. Lett.*, 103:063001, Aug 2009.

[43] WF McGrew, X Zhang, RJ Fasano, SA Schäffer, K Beloy, D Nicolodi, RC Brown, N Hinkley, G Milani, M Schioppo, et al. Atomic clock performance enabling geodesy below the centimetre level. *Nature*, 564(7734):87–90, 2018.

[44] Takuya Kohno, Masami Yasuda, Kazumoto Hosaka, Hajime Inaba, Yoshiaki Nakajima, and Feng-Lei Hong. One-dimensional optical lattice clock with a fermionic 171yb isotope. *Applied Physics Express*, 2(7):072501, jun 2009.

[45] Takumi Kobayashi, Daisuke Akamatsu, Kazumoto Hosaka, Yusuke Hisai, Masato Wada, Hajime Inaba, Tomonari Suzuyama, Feng-Lei Hong, and Masami Yasuda. Demonstration of the nearly continuous operation of an 171yb optical lattice clock for half a year. *Metrologia*, 57(6):065021, nov 2020.

[46] Masami Yasuda, Hajime Inaba, Takuya Kohno, Takehiko Tanabe, Yoshiaki Nakajima, Kazumoto Hosaka, Daisuke Akamatsu, Atsushi Onae, Tomonari Suzuyama, Masaki Amemiya, and Feng-Lei Hong. Improved absolute frequency measurement of the 171yb optical lattice clock towards a candidate for the redefinition of the second. *Applied Physics Express*, 5(10):102401, sep 2012.

[47] Takumi Kobayashi, Akiko Nishiyama, Kazumoto Hosaka, Daisuke Akamatsu, Akio Kawasaki, Masato Wada, Hajime Inaba, Takehiko Tanabe, and Masami Yasuda. Improved absolute frequency measurement of 171yb at nmij with uncertainty below 2×10^{-16}. $Metrologia, 62(2) : 025006, mar2025$.

[48] Chang Yong Park, Dai-Hyuk Yu, Won-Kyu Lee, Sang Eon Park, Eok Bong Kim, Sun Kyung Lee, Jun Woo Cho, Tai Hyun Yoon, Jongchul Mun, Sung Jong Park, Taeg Yong Kwon, and Sang-Bum Lee. Absolute frequency measurement of 1s0(f = 1/2)–3p0(f = 1/2) transition of 171yb atoms in a one-dimensional optical lattice at kriss. *Metrologia*, 50(2):119, feb 2013.

[49] Huidong Kim, Myoung-Sun Heo, Won-Kyu Lee, Chang Yong Park, Hyun-Gue Hong, Sang-Wook Hwang, and Dai-Hyuk Yu. Improved absolute frequency measurement of the 171yb optical lattice clock at kriss relative to the si second. *Japanese Journal of Applied Physics*, 56(5):050302, mar 2017.

[50] Huidong Kim, Myoung-Sun Heo, Chang Yong Park, Dai-Hyuk Yu, and Won-Kyu Lee. Absolute frequency measurement of the 171yb optical lattice clock at kriss using tai for over a year. *Metrologia*, 58(5):055007, aug 2021.

[51] Limeng Luo, Hao Qiao, Di Ai, Min Zhou, Shuang Zhang, Sheng Zhang, Changyue Sun, Qichao Qi, Chengquan Peng, Taoyun Jin, Wei Fang, Zhiqiang Yang, Tianchu Li, Kun Liang, and Xinye Xu. Absolute frequency measurement of an yb optical clock at the 1016 level using international atomic time. *Metrologia*, 57(6):065017, oct 2020.

[52] Marco Pizzocaro, Pierre Thoumany, Benjamin Rauf, Filippo Bregolin, Gianmaria Milani, Cecilia Clivati, Giovanni A Costanzo, Filippo Levi, and Davide Calonico. Absolute frequency measurement of the–transition of 171yb. *Metrologia*, 54(1):102, 2017.

[53] Marco Pizzocaro, Filippo Bregolin, Piero Barbieri, Benjamin Rauf, Filippo Levi, and Davide Calonico. Absolute frequency measurement of the 1s0–3p0 transition of 171yb with a link to international atomic time. *Metrologia*, 57(3):035007, 2020.

[54] Irene Goti, Stefano Condio, Cecilia Clivati, Matias Risaro, Michele Gozzelino, Giovanni A Costanzo, Filippo Levi, Davide Calonico, and Marco Pizzocaro. Absolute frequency measurement of a yb optical clock at the limit of the cs fountain. *Metrologia*, 60(3):035002, 2023.

[55] C Clivati, M Pizzocaro, EK Bertacco, S Condio, GA Costanzo, S Donadello, I Goti, M Gozzelino, F Levi, A Mura, et al. Coherent optical-fiber link across italy and france. *Physical Review Applied*, 18(5):054009, 2022.

[56] C-Y Xu, J Singh, JC Zappala, KG Bailey, MR Dietrich, JP Greene, W Jiang, ND Lemke, Z-T Lu, P Mueller, et al. Measurement of the hyperfine quenching rate of the clock transition in yb 171. *Physical Review Letters*, 113(3):033003, 2014.

[57] Martin M Boyd, Tanya Zelevinsky, Andrew D Ludlow, Sebastian Blatt, Thomas Zanon-Willette, Seth M Foreman, and Jun Ye. Nuclear spin effects in optical lattice clocks. *Physical Review A—Atomic, Molecular, and Optical Physics*, 76(2):022510, 2007.

[58] Sergey G Porsev, Andrei Derevianko, and EN Fortson. Possibility of an optical clock using the 6 1 s 0→ 6 3 p 0 o transition in 1 7 1, 1 7 3 yb atoms held in an optical lattice. *Physical Review A*, 69(2):021403, 2004.

[59] Hidetoshi Katori, Masao Takamoto, V. G. Pal'chikov, and V. D. Ovsiannikov. Ultrastable optical clock with neutral atoms in an engineered light shift trap. *Phys. Rev. Lett.*, 91:173005, Oct 2003.

[60] Stefano Condio. Optical lattice clock with an amplified laser diode. Master's thesis, Università di Torino, 2021.

[61] Nathan Dean Lemke. *Optical Lattice Clock with Spin-1/2 Ytterbium Atoms*. PhD thesis, University of Colorado Boulder, 2012.

[62] VA Dzuba, VV Flambaum, and S Schiller. Testing physics beyond the standard model through additional clock transitions in neutral ytterbium. *Physical Review A*, 98(2):022501, 2018.

[63] Marianna S Safronova, Sergey G Porsev, Christian Sanner, and Jun Ye. Two clock transitions in neutral yb for the highest sensitivity to variations of the fine-structure constant. *Physical review letters*, 120(17):173001, 2018.

[64] Taiki Ishiyama, Koki Ono, Tetsushi Takano, Ayaki Sunaga, and Yoshiro Takahashi. Observation of an inner-shell orbital clock transition in neutral ytterbium atoms. *Physical Review Letters*, 130(15):153402, 2023.

[65] K. Honda, Y. Takahashi, T. Kuwamoto, M. Fujimoto, K. Toyoda, K. Ishikawa, and T. Yabuzaki. Magneto-optical trapping of yb atoms and a limit on the branching ratio of the $^1P_1$ state. *Phys. Rev. A*, 59:R934–R937, Feb 1999.

[66] Filippo Bregolin. *Yb-171 optical frequency standards towards the redefinition of the second*. PhD thesis, Politecnico di Torino, 2019.

[67] Irene Goti. *High accuracy Yb optical lattice clock: frequency comparisons and contributions to International Atomic Time*. PhD thesis, Politecnico di Torino, 2023.

[68] Benjamin Rauf. *Absolute frequency measurement of an 171Yb lattice clock and optical clock comparisons*. PhD thesis, Politecnico di Torino, 2023.

[69] Gianmaria Milani. *Realization of advanced 171Yb optical lattice frequency standard*. PhD thesis, Politecnico di Torino, 2023.

[70] Marco Pizzocaro. *Realization and characterization of optical frequency standards*. PhD thesis, Politecnico di Torino, 2013.

[71] M. Schioppo, N. Poli, M. Prevedelli, St. Falke, Ch. Lisdat, U. Sterr, and G. M. Tino. A compact and efficient strontium oven for laser-cooling experiments. *Review of Scientific Instruments*, 83(10):103101, 10 2012.

[72] W. P. Risk, T. R. Gosnell, and A. V. Nurmikko. *Compact Blue-Green Lasers*. Cambridge University Press, 2003.

[73] Marco Pizzocaro, Davide Calonico, Pablo Cancio Pastor, Jacopo Catani, Giovanni A. Costanzo, Filippo Levi, and Luca Lorini. Efficient frequency doubling at 399 nm. *Appl. Opt.*, 53(16):3388–3392, Jun 2014.

[74] T.W. Hansch and B. Couillaud. Laser frequency stabilization by polarization spectroscopy of a reflecting reference cavity. *Optics Communications*, 35(3):441–444, 1980.

[75] Gianmaria Milani, Benjamin Rauf, Piero Barbieri, Filippo Bregolin, Marco Pizzocaro, Pierre Thoumany, Filippo Levi, Davide Calonico, et al. Multiple wavelength stabilization on a single optical cavity using the offset sideband locking technique. *Optics letters*, 42(10):1970–1973, 2017.

[76] bandpass filter Optigrate Volume Bragg grating. https://optigrate.com/braggrate-bandpass-filter/.

[77] Jonas E Hellstrom, Björn Jacobsson, Valdas Pasiskevicius, and Fredrik Laurell. Finite beams in reflective volume bragg gratings: theory and experiments. *IEEE Journal of quantum electronics*, 44(1):81–89, 2007.

[78] Léon Brillouin. Diffusion de la lumière et des rayons x par un corps transparent homogène. In *Annales de physique*, volume 9, pages 88–122, 1922.

[79] Benjamin Rauf, Vélez López, Pierre Thoumany, Marco Pizzocaro, and Davide Calonico. Phase noise cancellation in polarisation-maintaining fibre links. *Review of Scientific Instruments*, 89(3), 2018.

[80] Toptica photonics. https://www.toptica.com/products/tunable-diode-lasers/laser-locking-electronics/falc-110-mfalc-110-fast-pid. Falc110, Fast laser locking module.

[81] Harold J Metcalf and Peter Van der Straten. *Laser cooling and trapping*. Springer Science & Business Media, 1999.

[82] Harold J Metcalf and Peter Van der Straten. Laser cooling and trapping of neutral atoms. *The Optics Encyclopedia: Basic Foundations and Practical Applications*, 2007.

[83] D. J. Wineland and Wayne M. Itano. Laser cooling of atoms. *Phys. Rev. A*, 20:1521–1540, Oct 1979.

[84] Kurt Gibble and Boudewijn J Verhaar. Eliminating cold-collision frequency shifts. *Physical Review A*, 52(4):3370, 1995.

[85] Eric L Hazlett, Yi Zhang, Ronald W Stites, Kurt Gibble, and Kenneth M O'Hara. S-wave collisional frequency shift of a fermion clock. *Physical review letters*, 110(16):160801, 2013.

[86] Ryotatsu Yanagimoto, Nils Nemitz, Filippo Bregolin, and Hidetoshi Katori. Decomposed description of ramsey spectra under atomic interactions. *Physical Review A*, 98(1):012704, 2018.

[87] Nils Nemitz, Asbjørn Arvad Jørgensen, Ryotatsu Yanagimoto, Filippo Bregolin, and Hidetoshi Katori. Modeling light shifts in optical lattice clocks. *Physical Review A*, 99(3):033424, 2019.

[88] Nathan D Lemke, J Von Stecher, JA Sherman, AM Rey, CW Oates, and AD Ludlow. p-wave cold collisions in an optical lattice clock. *Physical Review Letters*, 107(10):103902, 2011.

[89] Sangkyung Lee, Chang Yong Park, Won-Kyu Lee, and Dai-Hyuk Yu. Cancellation of collisional frequency shifts in optical lattice clocks with rabi spectroscopy. *New Journal of Physics*, 18(3):033030, 2016.

[90] X. Zhang, K. Beloy, Y. S. Hassan, W. F. McGrew, C.-C. Chen, J. L. Siegel, T. Grogan, and A. D. Ludlow. Subrecoil clock-transition laser cooling enabling shallow optical lattice clocks. *Phys. Rev. Lett.*, 129:113202, Sep 2022.

[91] Chun-Chia Chen, Jacob L Siegel, Benjamin D Hunt, Tanner Grogan, Youssef S Hassan, Kyle Beloy, Kurt Gibble, Roger C Brown, and Andrew D Ludlow. Clock-line-mediated sisyphus cooling. *Physical Review Letters*, 133(5):053401, 2024.

[92] Kyle Beloy, Xiaogang Zhang, William F McGrew, Nathan Hinkley, Tai Hyun Yoon, Daniele Nicolodi, Robert J Fasano, Stefan A Schaeffer, Roger C Brown, and Andrew D Ludlow. Faraday-shielded dc stark-shift-free optical lattice clock. *Physical review letters*, 120(18):183201, 2018.

[93] Jérôme Lodewyck, Michal Zawada, Luca Lorini, Mikhail Gurov, and Pierre Lemonde. Observation and cancellation of a perturbing dc stark shift in strontium optical lattice clocks. *IEEE transactions on ultrasonics, ferroelectrics, and frequency control*, 59(3):411–415, 2012.

[94] J. A. Sherman, N. D. Lemke, N. Hinkley, M. Pizzocaro, R. W. Fox, A. D. Ludlow, and C. W. Oates. High-accuracy measurement of atomic polarizability in an optical lattice clock. *Phys. Rev. Lett.*, 108:153002, Apr 2012.

[95] Claude Cohen-Tannoudji and David Guéry-Odelin. *Advances in atomic physics: an overview*. World Scientific, 2011.

[96] Kyle Beloy, WF McGrew, Xiaogang Zhang, Daniele Nicolodi, Robert J Fasano, YS Hassan, RC Brown, and AD Ludlow. Modeling motional energy spectra and lattice light shifts in optical lattice clocks. *Physical Review A*, 101(5):053416, 2020.

[97] A. V. Taichenachev, V. I. Yudin, V. D. Ovsiannikov, V. G. Pal'chikov, and C. W. Oates. Frequency shifts in an optical lattice clock due to magnetic-dipole and electric-quadrupole transitions. *Phys. Rev. Lett.*, 101:193601, Nov 2008.

[98] Ichiro Ushijima, Masao Takamoto, and Hidetoshi Katori. Operational magic intensity for sr optical lattice clocks. *Phys. Rev. Lett.*, 121:263202, Dec 2018.

[99] Hidetoshi Katori, V. D. Ovsiannikov, S. I. Marmo, and V. G. Palchikov. Strategies for reducing the light shift in atomic clocks. *Phys. Rev. A*, 91:052503, May 2015.

[100] V. D. Ovsiannikov, S. I. Marmo, V. G. Palchikov, and H. Katori. Higher-order effects on the precision of clocks of neutral atoms in optical lattices. *Phys. Rev. A*, 93:043420, Apr 2016.

[101] Roger C Brown, Nate B Phillips, Kyle Beloy, William F McGrew, Marco Schioppo, Robert J Fasano, Gianmaria Milani, Xiaogang Zhang, Nathan Hinkley, Holly Leopardi, et al. Hyperpolarizability and operational magic wavelength in an optical lattice clock. *Physical review letters*, 119(25):253001, 2017.

[102] S. Blatt, J. W. Thomsen, G. K. Campbell, A. D. Ludlow, M. D. Swallows, M. J. Martin, M. M. Boyd, and J. Ye. Rabi spectroscopy and excitation inhomogeneity in a one-dimensional optical lattice clock. *Phys. Rev. A*, 80:052703, Nov 2009.

[103] E. J. Angstmann, V. A. Dzuba, and V. V. Flambaum. Frequency shift of hyperfine transitions due to blackbody radiation. *Phys. Rev. A*, 74:023405, Aug 2006.

[104] K. Beloy, N. Hinkley, N. B. Phillips, J. A. Sherman, M. Schioppo, J. Lehman, A. Feldman, L. M. Hanssen, C. W. Oates, and A. D. Ludlow. Atomic clock with 1×10^{-18} room-temperature blackbody stark uncertainty. *Phys. Rev. Lett.*, 113:260801, Dec 2014.

[105] Iec Bipm, Ilac Ifcc, and Iupac Iso. Iupap, and oiml. *Evaluation of measurement data—Supplement*, 1, 2008.

[106] Matteo Barbiero, Marco G. Tarallo, Davide Calonico, Filippo Levi, Giacomo Lamporesi, and Gabriele Ferrari. Sideband-enhanced cold atomic source for optical clocks. *Phys. Rev. Appl.*, 13:014013, Jan 2020.

[107] Matteo Barbiero, Davide Calonico, Filippo Levi, and Marco G. Tarallo. Optically loaded strontium lattice clock with a single multi-wavelength reference cavity. *IEEE Transactions on Instrumentation and Measurement*, 71:1–9, 2022.

[108] Masao Takamoto, Feng-Lei Hong, Ryoichi Higashi, Yasuhisa Fujii, Michito Imae, and Hidetoshi Katori. Improved frequency measurement of a one-dimensional optical lattice clock with a spin-polarized fermionic 87sr isotope. *Journal of the Physical Society of Japan*, 75(10):104302, 2006.

[109] M. V. Romalis and E. N. Fortson. Zeeman frequency shifts in an optical dipole trap used to search for an electric-dipole moment. *Phys. Rev. A*, 59:4547–4558, Jun 1999.

[110] R. F. C. Vessot, M. W. Levine, E. M. Mattison, E. L. Blomberg, T. E. Hoffman, G. U. Nystrom, B. F. Farrel, R. Decher, P. B. Eby, C. R. Baugher, J. W. Watts, D. L. Teuber, and F. D. Wills. Test of relativistic gravitation with a space-borne hydrogen maser. *Phys. Rev. Lett.*, 45:2081–2084, Dec 1980.

[111] Resolution 2" BIPM, "On the definition of time scales. https://www.bipm.org/en/committees/cg/cgpm/26-2018/resolution-2.

[112] Kurt Gibble. Scattering of cold-atom coherences by hot atoms: Frequency shifts from background-gas collisions. *Phys. Rev. Lett.*, 110:180802, May 2013.

[113] Stephan Falke, Nathan Lemke, Christian Grebing, Burghard Lipphardt, Stefan Weyers, Vladislav Gerginov, Nils Huntemann, Christian Hagemann, Ali Al-Masoudi, Sebastian Häfner, Stefan Vogt, Uwe Sterr, and Christian Lisdat. A strontium lattice clock with 3×10^{-17} inaccuracy and its frequency. *New Journal of Physics*, 16(7):073023, jul 2014.

[114] S. G. Porsev, M. S. Safronova, A. Derevianko, and Charles W. Clark. Long-range interaction coefficients for ytterbium dimers. *Phys. Rev. A*, 89:012711, Jan 2014.

[115] Stephan Falke, Mattias Misera, Uwe Sterr, and Christian Lisdat. Delivering pulsed and phase stable light to atoms of an optical clock. *Applied Physics B*, 107:301–311, 2012.

[116] Pierre Lemonde and Peter Wolf. Optical lattice clock with atoms confined in a shallow trap. *Phys. Rev. A*, 72:033409, Sep 2005.

[117] L Olschewski. Determination of the nuclear magnetic moments on free 43 ca-, 87 sr-, 135 ba-, 137 ba-, 171 yb-and 173 yb-atoms by means of optical pumping. *Zeitschrift für Physik*, 249:205–227, 1972.

[118] W. Neuhauser, M. Hohenstatt, P. Toschek, and H. Dehmelt. Optical-sideband cooling of visible atom cloud confined in parabolic well. *Phys. Rev. Lett.*, 41:233–236, Jul 1978.

[119] Evan C. Reed, Lu Qi, and Kenneth R. Brown. Comparison of continuous and pulsed sideband cooling on an electric quadrupole transition. *Phys. Rev. A*, 110:013123, Jul 2024.

[120] A P Kulosa, O N Prudnikov, D Vadlejch, H A Fürst, A A Kirpichnikova, A V Taichenachev, V I Yudin, and T E Mehlstäubler. Systematic study of tunable laser cooling for trapped-ion experiments. *New Journal of Physics*, 25(5):053008, may 2023.

[121] Vladan Vuletić, Andrew J. Kerman, Cheng Chin, and Steven Chu. Observation of low-field feshbach resonances in collisions of cesium atoms. *Phys. Rev. Lett.*, 82:1406–1409, Feb 1999.

[122] Valerio Formichella, Giovanna Signorile, Tung Thanh Thai, Lorenzo Galleani, Marco Pizzocaro, Irene Goti, Stefano Condio, Cecilia Clivati, Matias Risaro, Filippo Levi, et al. Year-long optical time scale with sub-nanosecond capabilities. *Optica*, 11(4):523–530, 2024.

[123] Filippo Levi, Davide Calonico, Claudio E Calosso, Aldo Godone, Salvatore Micalizio, and Giovanni A Costanzo. Accuracy evaluation of itcsf2: a nitrogen cooled caesium fountain. *Metrologia*, 51(3):270, 2014.

[124] Lorenzo Galleani, Giovanna Signorile, Valerio Formichella, and Ilaria Sesia. Generating a real-time time scale making full use of the available frequency standards. *Metrologia*, 57(6):065015, 2020.

[125] Jérôme Lodewyck, Rodolphe Le Targat, Paul-Eric Pottie, Erik Benkler, Sebastian Koke, and Jochen Kronjäger. Universal formalism for data sharing and processing in clock comparison networks. *Physical Review Research*, 2(4):043269, 2020.

[126] Jacques Millo, Michel Abgrall, Michel Lours, EML English, Haifeng Jiang, Jocelyne Guéna, André Clairon, Michael E Tobar, Sébastien Bize, Yann Le Coq, et al. Ultralow noise microwave generation with fiber-based optical frequency comb and application to atomic fountain clock. *Applied Physics Letters*, 94(14), 2009.

[127] Burghard Lipphardt, Vladislav Gerginov, and Stefan Weyers. Optical stabilization of a microwave oscillator for fountain clock interrogation. *IEEE Transactions on Ultrasonics, Ferroelectrics, and Frequency Control*, 64(4):761–766, 2017.

[128] VV Flambaum and VA Dzuba. Search for variation of the fundamental constants in atomic, molecular, and nuclear spectra. *Canadian Journal of Physics*, 87(1):25–33, 2009.

[129] Jocelyne Guena, Michel Abgrall, Daniele Rovera, Philippe Laurent, Baptiste Chupin, Michel Lours, Giorgio Santarelli, Peter Rosenbusch, Michael E. Tobar, Ruoxin Li, Kurt Gibble, Andre Clairon, and Sebastien Bize. Progress in atomic fountains at lne-syrte. *IEEE Transactions on Ultrasonics, Ferroelectrics, and Frequency Control*, 59(3):391–409, 2012.

[130] J Guéna, M Abgrall, A Clairon, and S Bize. Contributing to tai with a secondary representation of the si second. *Metrologia*, 51(1):108, jan 2014.

[131] P. A. Williams, W. C. Swann, and N. R. Newbury. High-stability transfer of an optical frequency over long fiber-optic links. *J. Opt. Soc. Am. B*, 25(8):1284–1293, Aug 2008.

[132] Cecilia Clivati, Roberto Aiello, Giuseppe Bianco, Claudio Bortolotti, Paolo De Natale, Valentina Di Sarno, Pasquale Maddaloni, Giuseppe Maccaferri, Alberto Mura, Monia Negusini, Filippo Levi, Federico Perini, Roberto Ricci, Mauro Roma, Luigi Santamaria Amato, Mario Siciliani de Cumis, Matteo Stagni, Alberto Tuozzi, and Davide Calonico. Common-clock very long baseline interferometry using a coherent optical fiber link. *Optica*, 7(8):1031–1037, Aug 2020.

[133] Cecilia Clivati, Roberto Ambrosini, Thomas Artz, Alessandra Bertarini, Claudio Bortolotti, Matteo Frittelli, Filippo Levi, Alberto Mura, Giuseppe Maccaferri, Mauro Nanni, Monia Negusini, Federico Perini, Mauro Roma, Matteo Stagni, Massimo Zucco, and Davide Calonico. A vlbi experiment using a remote atomic clock via a coherent fibre link. *Scientific Reports*, 7(1):40992, 2017.

[134] Cecilia Clivati, Alice Meda, Simone Donadello, Salvatore Virzì, Marco Genovese, Filippo Levi, Alberto Mura, Mirko Pittaluga, Zhiliang Yuan, Andrew J. Shields, Marco Lucamarini, Ivo Pietro Degiovanni, and Davide Calonico. Coherent phase transfer for real-world twin-field quantum key distribution. *Nature Communications*, 13(1):157, 2022.

[135] Cecilia Clivati, Giacomo Cappellini, Lorenzo F. Livi, Francesco Poggiali, Mario Siciliani de Cumis, Marco Mancini, Guido Pagano, Matteo Frittelli, Alberto Mura, Giovanni A. Costanzo, Filippo Levi, Davide Calonico, Leonardo Fallani, Jacopo Catani, and Massimo Inguscio. Measuring absolute frequencies beyond the gps limit via long-haul optical frequency dissemination. *Opt. Express*, 24(11):11865–11875, May 2016.

[136] REFIMEVE. https://www.refimeve.fr/index.php/en/.

[137] F. Guillou-Camargo, V. Ménoret, E. Cantin, O. Lopez, N. Quintin, E. Camisard, V. Salmon, J.-M. Le Merdy, G. Santarelli, A. Amy-Klein, P.-E. Pottie, B. Desruelle, and C. Chardonnet. First industrial-grade coherent fiber link for optical frequency standard dissemination. *Appl. Opt.*, 57(25):7203–7210, Sep 2018.

[138] W. F. McGrew, X. Zhang, H. Leopardi, R. J. Fasano, D. Nicolodi, K. Beloy, J. Yao, J. A. Sherman, S. A. Schäffer, J. Savory, R. C. Brown, S. Römisch, C. W. Oates, T. E. Parker, T. M. Fortier, and A. D. Ludlow. Towards the optical second: verifying optical clocks at the si limit. *Optica*, 6(4):448–454, Apr 2019.

[139] NPL. https://empir.npl.co.uk/rocit/. EMPIR project 18SIB05.

[140] Pacôme Delva, Jérôme Lodewyck, S Bilicki, E Bookjans, Guy Vallet, R Le Targat, P-E Pottie, C Guerlin, F Meynadier, C Le Poncin-Lafitte, et al. Test of special relativity

using a fiber network of optical clocks. *Physical review letters*, 118(22):221102, 2017.

[141] International Clock, Oscillator Networking, Anne Amy-Klein, Erik Benkler, Pascal Blondé, Kai Bongs, Etienne Cantin, Christian Chardonnet, Heiner Denker, Sören Dörscher, et al. International comparison of optical frequencies with transportable optical lattice clocks. *arXiv preprint arXiv:2410.22973*, 2024.

[142] J Grotti, I Nosske, SB Koller, S Herbers, H Denker, L Timmen, G Vishnyakova, G Grosche, T Waterholter, A Kuhl, et al. Long-distance chronometric leveling with a transportable optical clock. *arXiv preprint arXiv:2309.14953*, 2023.

[143] BIPM. https://webtai.bipm.org/ftp/pub/tai/other-products/taipsfs/psfs.png. Graphical representation of all evaluations of Primary and Secondary Frequency Standardsreported since Circular T 190.

[144] "iMaser 3000 specifications. https://safran-navigation-timing.com/product/imaser-3000/?model_interest__c=iMaser+3000&product_interest___single_select=Atomic+Clocks+and+Oscillators.

[145] BIPM. http://webtai.bipm.org/database/clock.html.

[146] BIPM. http://webtai.bipm.org/database/documents/clockform.pdf.

[147] BIPM. https://www.bipm.org/en/publications/mises-en-pratique/standard-frequencies.html.

[148] BIPM. https://webtai.bipm.org/database/documents/guidelines-psfs-reports.pdf. Guidelines for the Primary and Secondary Frequency Standards data submission.

[149] V Formichella, L Galleani, G Signorile, and I Sesia. Robustness tests for an optical time scale. *Metrologia*, 59(1):015002, 2021.

[150] Valerio Formichella, Giovanna Signorile, Tung Thai, Lorenzo Galleani, Marco Pizzocaro, Irene Goti, Stefano Condio, Cecilia Clivati, Matias Risaro, and Filippo Levi. Supplementary document for Year-long optical time scale with sub-nanosecond capabilities - 6897806.pdf. *Optica*, 4 2024.

[151] William R Milner, John M Robinson, Colin J Kennedy, Tobias Bothwell, Dhruv Kedar, Dan G Matei, Thomas Legero, Uwe Sterr, Fritz Riehle, Holly Leopardi, et al. Demonstration of a timescale based on a stable optical carrier. *Physical Review Letters*, 123(17):173201, 2019.

[152] Jian Yao, Jeff A Sherman, Tara Fortier, Holly Leopardi, Thomas Parker, William McGrew, Xiaogang Zhang, Daniele Nicolodi, Robert Fasano, Stefan Schäffer, et al. Optical-clock-based time scale. *Physical review applied*, 12(4):044069, 2019.

[153] Christian Grebing, Ali Al-Masoudi, Sören Dörscher, Sebastian Häfner, Vladislav Gerginov, Stefan Weyers, Burghard Lipphardt, Fritz Riehle, Uwe Sterr, and Christian Lisdat. Realization of a timescale with an accurate optical lattice clock. *Optica*, 3(6):563–569, 2016.

[154] Hidekazu Hachisu, Fumimaru Nakagawa, Yuko Hanado, and Tetsuya Ido. Months-long real-time generation of a time scale based on an optical clock. *Scientific Reports*, 8(1):4243, 2018.

[155] H Hachisu, H Ito, N Nemitz, N Ohtsubo, Y Miyauchi, M Morikawa, K Matsubara, and T Ido. Utc (nict) referenced to a timescale based on the optical clock nict-sr1. In *2023 Joint Conference of the European Frequency and Time Forum and IEEE International Frequency Control Symposium (EFTF/IFCS)*, pages 1–3. IEEE, 2023.

[156] Takumi Kobayashi, Daisuke Akamatsu, Kazumoto Hosaka, Yusuke Hisai, Akiko Nishiyama, Akio Kawasaki, Masato Wada, Hajime Inaba, Takehiko Tanabe, Tomonari Suzuyama, et al. Generation of a precise time scale assisted by a near-continuously operating optical lattice clock. *Physical Review Applied*, 21(6):064015, 2024.

[157] Florian Schreck. Strontium BEC group. https://www.strontiumbec.com/.

[158] Chun-Chia Chen, Rodrigo González Escudero, Jiří Minář, Benjamin Pasquiou, Shayne Bennetts, and Florian Schreck. Continuous bose–einstein condensation. *Nature*, 606(7915):683–687, 2022.

[159] Alexander Urech, Ivo HA Knottnerus, Robert JC Spreeuw, and Florian Schreck. Narrow-line imaging of single strontium atoms in shallow optical tweezers. *Physical Review Research*, 4(2):023245, 2022.

[160] Mateusz Borkowski, Lukas Reichsöllner, Premjith Thekkeppatt, Vincent Barbé, Tijs van Roon, Klaasjan van Druten, and Florian Schreck. Active stabilization of kilogauss magnetic fields to the ppm level for magnetoassociation on ultranarrow Feshbach resonances. *Review of Scientific Instruments*, 94(7):073202, 07 2023.

[161] Francesca Famà, Sheng Zhou, Benedikt Heizenreder, Mikkel Tang, Shayne Bennetts, Simon B. Jäger, Stefan A. Schäffer, and Florian Schreck. Continuous cavity qed with an atomic beam. *Phys. Rev. A*, 110:063721, Dec 2024.

[162] Dominic Meiser, Jun Ye, DR Carlson, and MJ Holland. Prospects for a millihertz-linewidth laser. *Physical review letters*, 102(16):163601, 2009.

[163] Swadheen Dubey, Georgy A. Kazakov, Benedikt Heizenreder, Sheng Zhou, Shayne Bennetts, Stefan Alaric Schäffer, Ananya Sitaram, and Florian Schreck. Modeling of a continuous superradiant laser on the sub-mhz $^1s_0 \rightarrow {}^3p_0$ transition in neutral strontium-88. *Phys. Rev. Res.*, 7:013292, Mar 2025.

[164] D. G. Matei, T. Legero, S. Häfner, C. Grebing, R. Weyrich, W. Zhang, L. Sonderhouse, J. M. Robinson, J. Ye, F. Riehle, and U. Sterr. 1.5 μm lasers with sub-10 mhz linewidth. *Phys. Rev. Lett.*, 118:263202, Jun 2017.

[165] E Oelker, RB Hutson, CJ Kennedy, L Sonderhouse, T Bothwell, A Goban, D Kedar, C Sanner, JM Robinson, GE Marti, et al. Demonstration of 4.8$\times$ 10- 17 stability at 1 s for two independent optical clocks. *Nature Photonics*, 13(10):714–719, 2019.

[166] Matthew A. Norcia, Matthew N. Winchester, Julia R. K. Cline, and James K. Thompson. Superradiance on the millihertz linewidth strontium clock transition. *Science Advances*, 2(10):e1601231, 2016.

[167] Georgy A. Kazakov and Thorsten Schumm. Active optical frequency standards using cold atoms: Perspectives and challenges. In *2014 European Frequency and Time Forum (EFTF)*, pages 411–414, 2014.

[168] Horizon 2020. iqClock deliverable 5.5. https://cordis.europa.eu/project/id/820404/results, 2022.

[169] A Gogyan, G Kazakov, M Bober, and M Zawada. Characterisation and feasibility study for superradiant lasing in 40 ca atoms. *Optics express*, 28(5):6881–6892, 2020.

[170] Jia Zhang, Tiantian Shi, Jianxiang Miao, and Jingbiao Chen. The development of active optical clock. *AAPPS Bulletin*, 33(1):10, 2023.

[171] Rodrigo González Escudero, Chun-Chia Chen, Shayne Bennetts, Benjamin Pasquiou, and Florian Schreck. Steady-state magneto-optical trap of fermionic strontium on a narrow-line transition. *Physical Review Research*, 3(3):033159, 2021.

[172] Chun-Chia Chen, Shayne Bennetts, Rodrigo González Escudero, Florian Schreck, and Benjamin Pasquiou. Sisyphus optical lattice decelerator. *Phys. Rev. A*, 100:023401, Aug 2019.

[173] Junyu He, Benjamin Pasquiou, Rodrigo Gonzalez Escudero, Sheng Zhou, Mateusz Borkowski, and Florian Schreck. Coherent three-photon excitation of the strontium clock transition, 2024.

[174] E Peik, M Ben Dahan, I Bouchoule, Y Castin, and C Salomon. Bloch oscillations and an accelerator for cold atoms. *Applied Physics B: Lasers & Optics*, 65(6), 1997.

[175] Sheng Zhou. *Towards a continuous active optical clock based on superradiant lasing using strontium*. PhD thesis, Universiteit van Amsterdam, 2024.

[176] Erwin K Lau, Liang Jie Wong, and Ming C Wu. Enhanced modulation characteristics of optical injection-locked lasers: A tutorial. *IEEE Journal of Selected Topics in Quantum Electronics*, 15(3):618–633, 2009.

[177] Zhixin Liu and Radan Slavík. Optical injection locking: From principle to applications. *Journal of Lightwave Technology*, 38(1):43–59, 2020.

[178] Finn Mogensen, Henning Olesen, and Gunnar Jacobsen. Locking conditions and stability properties for a semiconductor laser with external light injection. *IEEE Journal of Quantum Electronics*, 21(7):784–793, 1985.

[179] Scott Wolzak. to be completed. Master's thesis, Institute of Physics,Universiteit van Amsterdam, 2023.

[180] Patrick F Egan, Jack A Stone, Jay H Hendricks, Jacob E Ricker, Gregory E Scace, and Gregory F Strouse. Performance of a dual fabry–perot cavity refractometer. *Optics Letters*, 40(17):3945–3948, 2015.

[181] Moustafa Abdel-Hafiz, Piotr Ablewski, Ali Al-Masoudi, Héctor Álvarez Martínez, Petr Balling, Geoffrey Barwood, Erik Benkler, Marcin Bober, Mateusz Borkowski, William Bowden, Roman Ciuryło, Hubert Cybulski, Alexandre Didier, Miroslav Doležal, Sören Dörscher, Stephan Falke, Rachel M. Godun, Ramiz Hamid, Ian R. Hill, Richard Hobson, Nils Huntemann, Yann Le Coq, Rodolphe Le Targat, Thomas Legero, Thomas Lindvall, Christian Lisdat, Jérôme Lodewyck, Helen S. Margolis, Tanja E. Mehlstäubler, Ekkehard Peik, Lennart Pelzer, Marco Pizzocaro, Benjamin Rauf, Antoine Rolland, Nils Scharnhorst, Marco Schioppo, Piet O. Schmidt, Roman Schwarz, Çağrı Şenel, Nicolas Spethmann, Uwe Sterr, Christian Tamm, Jan W. Thomsen, Alvise Vianello, and Michał Zawada. Guidelines for developing optical clocks with 10^{-18} fractional frequency uncertainty, 2019.

[182] Jonas Keller, Stepan Ignatovich, Stephen A Webster, and Tanja E Mehlstäubler. Simple vibration-insensitive cavity for laser stabilization at the 10- 16 level. *Applied Physics B*, 116:203–210, 2014.

[183] Eric D Black. An introduction to pound–drever–hall laser frequency stabilization. *American journal of physics*, 69(1):79–87, 2001.

[184] Thies Plassmann. A strontium rydberg laser for quantum simulation with tweezer arrays. Master's thesis, Universiteit van Amsterdam, 2021.